SSC-342

GLOBAL ICE FORCES AND SHIP RESPONSE TO ICE
ANALYSIS OF ICE RAMMING FORCES
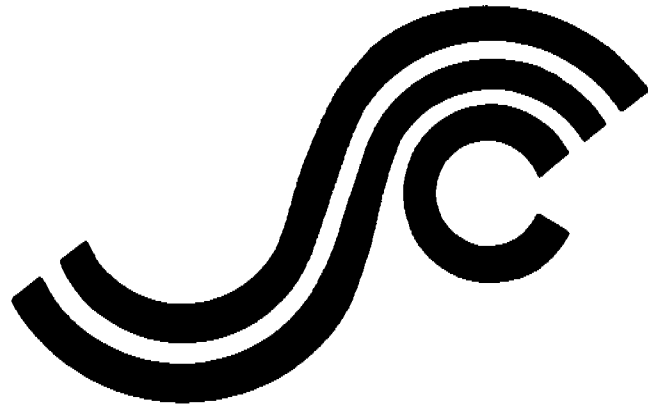
SHIP STRUCTURE COMMITTEE

1990

SHIP STRUCTURE COMMITTEE

The SHIP STRUCTURE COMMITTEE is constituted to prosecute a research program to improve the hull structures of ships and other marine structures by an extension of knowledge pertaining to design, materials, and methods of construction.

RADM J. D. Sipes, USCG, (Chairman)
Chief, Office of Marine Safety, Security
  and Environmental Protection
U. S. Coast Guard

Mr. Alexander Malakhoff
Director, Structural Integrity
  Subgroup (SEA 55Y)
Naval Sea Systems Command

Dr. Donald Liu
Senior Vice President
American Bureau of Shipping

Mr. H. T. Haller
Associate Administrator for Ship-
  building and Ship Operations
Maritime Administration

Mr. Thomas W. Allen
Engineering Officer (N7)
Military Sealift Command

CDR Michael K. Parmelee, USCG,
Secretary, Ship Structure Committee
U. S. Coast Guard

CONTRACTING OFFICER TECHNICAL REPRESENTATIVES

Mr. William J. Siekierka
SEA 55Y3
Naval Sea Systems Command

Mr. Greg D. Woods
SEA 55Y3
Naval Sea Systems Command

SHIP STRUCTURE SUBCOMMITTEE

The SHIP STRUCTURE SUBCOMMITTEE acts for the Ship Structure Committee on technical matters by providing technical coordination for determinating the goals and objectives of the program and by evaluating and interpreting the results in terms of structural design, construction, and operation.

AMERICAN BUREAU OF SHIPPING

Mr. Stephen G. Arntson (Chairman)
Mr. John F. Conlon
Mr. William Hanzalek
Mr. Philip G. Rynn

MILITARY SEALIFT COMMAND

Mr. Albert J. Attermeyer
Mr. Michael W. Touma
Mr. Jeffery E. Beach

MARITIME ADMINISTRATION

Mr. Frederick Seibold
Mr. Norman O. Hammer
Mr. Chao H. Lin
Dr. Walter M. Maclean

NAVAL SEA SYSTEMS COMMAND

Mr. Robert A. Sielski
Mr. Charles L. Null
Mr. W. Thomas Packard
Mr. Allen H. Engle

U. S. COAST GUARD

CAPT T. E. Thompson
CAPT Donald S. Jensen
CDR Mark E. Noll

SHIP STRUCTURE SUBCOMMITTEE LIAISON MEMBERS

U. S. COAST GUARD ACADEMY

LT Bruce Mustain

U. S. MERCHANT MARINE ACADEMY

Dr. C. B. Kim

U. S. NAVAL ACADEMY

Dr. Ramswar Bhattacharyya

STATE UNIVERSITY OF NEW YORK MARITIME COLLEGE

Dr. W. R. Porter

WELDING RESEARCH COUNCIL

Dr. Martin Prager

NATIONAL ACADEMY OF SCIENCES – MARINE BOARD

Mr. Alexander B. Stavovy

NATIONAL ACADEMY OF SCIENCES – COMMITTEE ON MARINE STRUCTURES

Mr. Stanley G. Stiansen

SOCIETY OF NAVAL ARCHITECTS AND MARINE ENGINEERS – HYDRODYNAMICS COMMITTEE

Dr. William Sandberg

AMERICAN IRON AND STEEL INSTITUTE

Mr. Alexander D. Wilson

Ship Structure Committee

An Interagency Advisory Committee
Dedicated to the Improvement of Marine Structures

SSC-342
SR-1313

December 3, 1990

GLOBAL ICE FORCES AND SHIP RESPONSE TO ICE
ANALYSIS OF ICE RAMMING FORCES

This report is the fifth in a series of six that address ice loads, ice forces, and ship response to ice. The data for these reports were obtained during deployments of the U.S. Coast Guard Icebreaker POLAR SEA. This report supplements SSC-341, Global Ice Forces and Ship Response to Ice and contains a discussion of the finite element model that was developed to predict ice ramming forces. The other ice reports are published as SSC-329, SSC-339, SSC-340, SSC-341 and SSC-343.

J. D. SIPES
Rear Admiral, U.S. Coast Guard
Chairman, Ship Structure Committee

1. Report No. SSC-342	2. Government Accession No.	3. Recipient's Catalog No.
4. Title and Subtitle Global Ice Forces and Ship Response to Ice - Analysis of Ice Ramming Forces		**5. Report Date** August 1990
		6. Performing Organization Code
7. Author's) Yung-Kuang Chen, Alfred L. Tunik, Albert P-Y Chen		**8. Performing Organization Report No.** ABS Tech. Rpt. RD-87011 OED-87522
9. Performing Organization Name and Address AMERICAN BUREAU OF SHIPPING 45 Eisenhower Drive Paramus, NJ 07653		**10. Work Unit No. (TRAIS)**
		11. Contract or Grant No.
12. Sponsoring Agency Name and Address Maritime Administration U.S.Dept. of Trans 400 Seventh Street, SW Washington, D.C. 20593	Transport Development Ctr. 200 Dorchester Blvd.,West Suite 601, West Tower Montreal, Quebec Canada H2Z 1X4	**13. Type of Report and Period Covered** Final Report
		14. Sponsoring Agency Code MAR-760

15. Supplementary Notes This was an international joint project between the Ship Structure Committee (USA) and the Transport Development Centre (Canada). The U.S. Maritime Administration served as the sponsoring agency for the interagency Ship Structure Committee.

16. Abstract During September and October of 1985 the Polar Sea conducted ice-impact tests on heavily ridged ice features in the Alaskan portion of the Beaufort Sea. Bending strain gage measurements were used to estimate the longitudinal bending moment distribution of the POLAR SEA during impacts with ice pressure ridges. Compressive strains along the stem and ship acceleration and velocity measurements were also recorded. This paper describes the methodology for determining the global ice impact force from the measurements and presents the results of these tests. A comparison of the results with other available data is also presented. Hull strain, and impact force time histories are presented along with the longitudinal bending and shear distributions during ice impact events. The results indicate that the methodology used in estimating the impact force provided and excellent understanding of ship-ice interaction.

This supplement to the main report (Global Ice Forces and Ship Response to Ice, SSC-341) contains a discussion of a finite element model that was developed to predict ice ramming forces and includes a comparison of the model's results with selected ramming events.

17. Key Words Design Criteria Ice Loads Icebreakers Shipboard Loads Measurement	18. Distribution Statement Document is available to the U.S. Public through the National Technical Information Service, Springfield, VA 22161

19. Security Classif. (of this report) Unclassified	20. Security Classif. (of this page) Unclassified	21. No. of Pages	22. Price

Form DOT F 1700.7 (8-72)   Reproduction of completed page authorized

METRIC CONVERSION FACTORS

Approximate Conversions to Metric Measures

Symbol	When You Know	Multiply by	To Find	Symbol
		LENGTH		
in	inches	*2.5	centimeters	cm
ft	feet	30	centimeters	cm
yd	yards	0.9	meters	m
mi	miles	1.6	kilometers	km
		AREA		
in²	square inches	6.5	square centimeters	cm²
ft²	square feet	0.09	square meters	m²
yd²	square yards	0.8	square meters	m²
mi²	square miles	2.6	square kilometers	km²
	acres	0.4	hectares	ha
		MASS (weight)		
oz	ounces	28	grams	g
lb	pounds	0.45	kilograms	kg
	short tons (2000 lb)	0.9	tonnes	t
		VOLUME		
tsp	teaspoons	5	milliliters	ml
Tbsp	tablespoons	15	milliliters	ml
fl oz	fluid ounces	30	milliliters	ml
c	cups	0.24	liters	l
pt	pints	0.47	liters	l
qt	quarts	0.95	liters	l
gal	gallons	3.8	liters	l
ft³	cubic feet	0.03	cubic meters	m³
yd³	cubic yards	0.76	cubic meters	m³
		TEMPERATURE (exact)		
°F	Fahrenheit temperature	5/9 (after subtracting 32)	Celsius temperature	°C

*1 in. = 2.54 cm (exactly). For other exact conversions and more detail tables see NBS Misc. Publ. 286. Units of Weight and Measures. Price $2.25 SD Catalog No. C13 10 286.
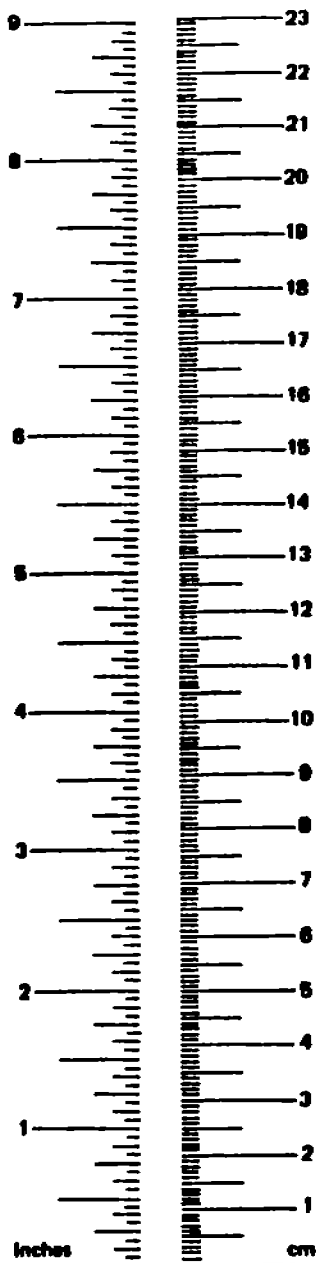
Approximate Conversions from Metric Measures

Symbol	When You Know	Multiply by	To Find	Symbol
		LENGTH		
mm	millimeters	0.04	inches	in
cm	centimeters	0.4	inches	in
m	meters	3.3	feet	ft
m	meters	1.1	yards	yd
km	kilometers	0.6	miles	mi
		AREA		
cm²	square centimeters	0.16	square inches	in²
m²	square meters	1.2	square yards	yd²
km²	square kilometers	0.4	square miles	mi²
ha	hectares (10,000 m²)	2.5	acres	
		MASS (weight)		
g	grams	0.035	ounces	oz
kg	kilograms	2.2	pounds	lb
t	tonnes (1000 kg)	1.1	short tons	
		VOLUME		
ml	milliliters	0.03	fluid ounces	fl oz
l	liters	2.1	pints	pt
l	liters	1.06	quarts	qt
l	liters	0.26	gallons	gal
m³	cubic meters	36	cubic feet	ft³
m³	cubic meters	1.3	cubic yards	yd³
		TEMPERATURE (exact)		
°C	Celsius temperature	9/5 (then add 32)	Fahrenheit temperature	°F

°F
-40   0   32 40   80 98.6 120   160   200 212
-40   -20   0   20   37 40   60   80   100
°C

TABLE OF CONTENTS

1. INTRODUCTION

The strain gauge measurement records acquired during the USCG POLAR SEA winter deployment represent a unique data base for predicting ice induced forces due to ramming icebreaking. The overall objective of such tests is aimed at development of an analytical model capable of describing the ship/ice impact interaction. The model can be used as an effective tool in developing rational strength standards, in designing icebreakers and icebreaking cargo ships, in evaluating ultimate capabilities of the ships in various ice conditions and other applications.

Two principal questions arise when analyzing the data and developing a model. First, what is the nature of relationships between the ice-induced load parameters (pressure, total force, duration and time history, etc.) and the initial impact characteristics (the masses, rigidities, mechanical properties of the ship and the ice, and their impact velocities and locations). Secondly, what is the relationship between the actual ice load parameters and the measured response of the ship structure, or in other words, how to interpret the recorded data. This report is addressed to answering both questions.

In Section II the analytical model of ship/ice interaction is briefly described. The recorded data of the ramming forces, their durations and time histories, ramming velocity records, and the locations of the ramming forces are analyzed and compared with those predicted by the analytical model for the actual testing conditions. The work releated to this section was performed by the Ocean Engineering Division of the American Bureau of Shipping.

In Section III the dynamic response of the hull structure subject to various impact loads is analysed. The purpose of this analysis is to justify the applicability and determine the accuracy of the beam idealization used in interpreting the ice impact load measurements, as well as to study in detail the dynamic reponse of the complex hull structure to time varying impact loads due to ramming icebreaking. The work of this section was carried out by ABS/Research and Development Division.

The dynamic structural analysis was performed using a three-dimensional finite element model representing the entire vessel including the deckhouse and other superstructures. At the forward end of the vessel where the ice impact loads occurred, a fine mesh model was used to connect through a transition segment to a coarser mesh representation of the remainder of the vessel. This is to ensure that the structural response in the areas of interest could be determined accurately.

A free vibration analysis was first carried out to determine the natural frequencies and mode shapes representing the coupled hull girder and deckhouse vibration. Then, a forced vibration was performed to obtain the transient response of the vessel to time varying impact loads. The ice impact loads used in the analysis were obtained from the measured data corresponding to Ram 14 and Ram 39. Case studies were also included for ice impact loads with predefined shapes of time functions, including the ABS analytical model described in Section II.

2. RAMMING FORCE ANALYSIS

2.1 ANALYTICAL MODEL
Nomenclature

A   -   parameter characterizing dynamic crushing strength of ice, $MPa(s/m^3)^{1/4}$;

B   -   ship breadth, m;

C_B -   block coefficient;

D   -   displacement measured in force units, MN;

d   -   ship draft

F_n -   global impact force normal to the stem, MN;

F_v -   vertical component of F_n, MN;

F(t)   -   dimensionless force history factor which is force F_n at instantaneous time "t" normalized with respect to its maximum;

R   -   parameter characterizing ridge size, m;

S   -   shape factor

T   -   peak force duration, sec

t   -   dimensionless instantaneous time normalized with respect to T;

β -   frame flare angle between the vertical and the frame tangent line measured at the stem line in the vertical plane perpendicular to the center plane, (see Fig. 6), deg.;

ψ -   stem inclination angle to the horizon, (see Fig. 6), deg.;

In accordance with the overall objective of the POLAR SEA deployment, the ice loads recorded during ramming ice-breaking should be used as a database for development of an analytical model. The model is to be capable of predicting impact ice loads on ships of various displacements and shapes navigating in various ice conditions.

The analytical model, of solid/ice impact developed by Kheisin and Kurdyumov in 1970's [3; 4] appears to be most suitable for this purpose. In a generalized form [7] the model describes the ice impact loads on

ships as functions of ship and ice masses, their dimensional and inertial characteristics, contact zone shapes, the mechanical properties of ice, and the relative impact velocity.

It should be emphasized that the model describes the impact penetration of a solid into ice. Static or quasi-static interactions are beyond the scope of this model. Ship/ice interaction during ramming has usually two distinguishable phases: the initial phase of impact penetration into ice accompanied by ice crushing, and the following beaching phase. Higher forces are usually (but not necessarily) generated during the impact phase. In this report only the impact forces clearly distinguishable in the records are analyzed using the analytical model.

The model has been used to analyze impact ice loads for the following applications:

- field tests of a steel ball dropped on flat ice surface [3, 4 and others];

- laboratory tests of a steel pendulum impacting ice samples [2, 7];

- ramming ice-breaking [8];

- iceberg / structure impacts [1, 6].

For icebreakers ramming massive ice features the ice load parameters are expressed in [8] as follows:

$$F_n = K_F D^d V^v A^a S F(t) \tag{1}$$

$$T = K_T DV/F_n \tag{2}$$

where coefficients (K_F, K_T), exponents (d, v, a), force time history factor F(t) and shape factor (S) vary depending on particular slopes of the ship bow and the ice feature. For ramming ice-breaking the range of variations of the exponents and force history factor is given in Table 1 and Figure 1 whose data represent some idealized shapes of ships and ice.

TABLE 1

Exponent	Wedge-shaped bow		Spoon-shaped bow	
	Rectangular ice edge	Rounded ice edge	Rectangular ice edge	Rounded ice edge
d	5/7	7/11	2/3	5/9
v	3/2	15/11	17/12	11/9
a	2/7	4/11	1/3	4/9
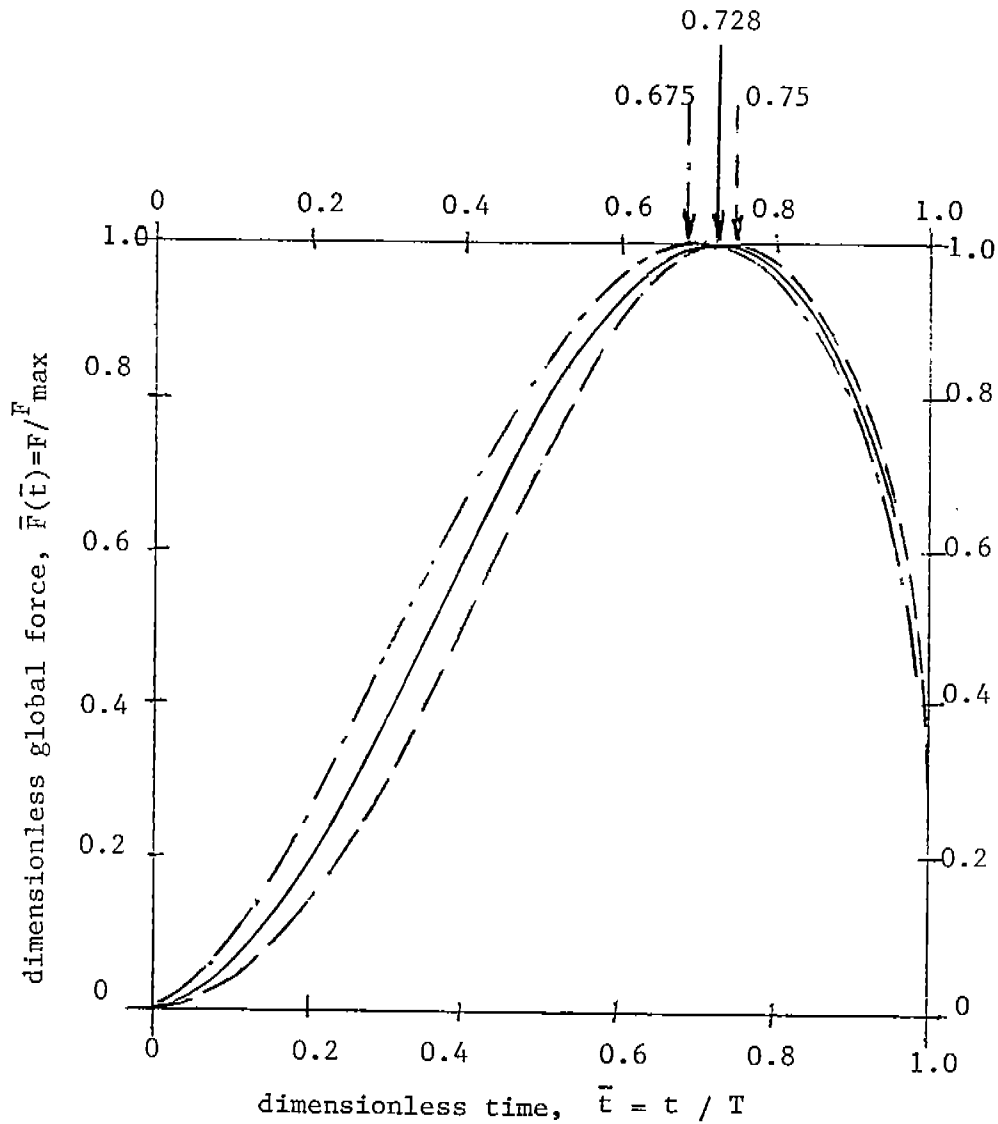
Fig. 1. Theoretical force time history curves

_____ used in the analysis

___ · ___· predicted for drop ball test

– – – – predicted for a side impact

Those idealizations represent some extremities limiting the actual shapes. Therefore, the numerical values of the exponents should be selected within the range of the extremities. The values selected for practical applications should be regarded as approximations.

The coefficients (K_F and K_T) also incorporate various idealizations and simplifications used in deriving equations (1) - (2) (e.g. added water mass effects, ice edge spalling effects, pressure distribution over the crushed ice layer's thickness, etc; for details - see [4; 7]). In practical applications, their numerical values should be adjusted in accordance with test data.

The POLAR SEA has a wedge-shaped bow, though not the perfect wedge. Her bow flare angles at the stem are very high (exceeding 60°) while the stem inclination angle is small (less than 20° at the design waterline area) and variable. Such a dull wedge can be treated as an intermediate shape between the perfect wedge and a spoon-shaped bow, though much closer to the wedge.

The shapes of ice ridges vary greatly and individual ridges can differ significantly from each other and from any idealization. Such variety of shapes was also characteristic for the ridges being rammed during the deployment (see survey data in ref. 18 of the Report). Moreover, they are often composed of separate ice blocks connected more or less loosely. The presence of multi-year ice inclusions was observed visually. Coring and thermal drilling also showed the presence of large cavities.

For such testing conditions the values of exponents given in third column of Table 1 or slightly lower can be most suitable. In this analysis the equations (1) and (2) are used in the following form:

$$F_n = 0.22 D^{7/11} V^{15/11} A^{4/11} S F (t) \tag{3}$$

$$T = 0.06 DV/F_n \tag{4}$$

$$\text{where:} \quad S = R^{3/11} S_b \tag{5}$$

R - parameter characterizing ridge height.

$$S_b = (0.5 \tan \beta \sin 2\varphi)^{4/11} \sin\varphi [(q+\tan^2\varphi) \cos^2\varphi]^{7/11} \tag{6}$$

$$q = [1 + \frac{2 C_w^2 B/d}{3 C_B (1+C_w)}]^{-1} + \frac{3.57}{C_B} [1 + \frac{B/d}{(3-2C_w)(3-C_w)}]^{-1} \tag{6a}$$

C_B - block coefficient
C_W - waterplane coefficient
B/d - breadth-to-draft ratio

The relationship between the vertical and normal components of the global force is:

$$F_v = F_n \cos\varphi \qquad\qquad (7)$$

2.2 GENERAL EVALUATION OF THE TEST RECORDS

2.2.1 Force Records

Of the thirty eight ram records listed in Table 2 and 6 of the ARCTEC's Report, only the records of the rams for which higher forces have been recorded are requested for the analysis. The submitted records contain almost all peak forces exceeding 14 MN. The 25-second records of the global force and velocity histories are reproduced in Figures 2a through 2n.

It should be kept in mind that global ramming force records are not what had been directly measured during the trial. The sensors have registered strains in ship structures, and the measured strains are converted to stresses based on the linear stress-strain relationship. The next steps of expressing the bending moments and shear forces via the stresses are based on beam theory with some idealizations and approximations of the stress distribution in the hull girder acted upon by a bow force.

The beam idealization used in the Arctec's program can result in some inaccuracy when interpreting the strain gauge readings into vertical ramming forces. However, such inaccuracy, if found, can be of a systematic type and does not affect the capability of the analytical model to fit and explain the experimental data. Therefore, the force records presented in Figure 2 are presumed to be true sensor readings.

All of the force records in Figure 2 distinctly show a peak at the beginning of the ram. For a number of events there are several peaks during the ram. Durations of each peak force do not exceed 1.0 - 1.5 seconds. For some events there is only a single peak followed by a significantly lower beaching forces (rams 2, 14, 15, 25). For rams 37 and 38 beaching forces are of the same or higher values as the initial impact peak forces. The beaching force duration range typically from 5 to 10 seconds but can be longer as recorded for rams 37 and 38. The presence of several peaks (rams 3, 9, 17, 26, 33, 34, 37) implies that the rammed ice ridges were composed of several ice hummocks or blocks relatively loosely connected with each other - the fact which was actually recorded in the ridge survey report (see ref. 18 of the Report). However, from the field survey data it is impossible to specify the separate ridge components. Ram 38 is the only ram for which the beaching force exceeds the initial impact force and, moreover, the latter is not easy to distinguish. This ram record is not included for further analysis of the impact forces.

2.2.2 Velocity records

Ship speed histories recorded from doppler log readings for the rams in question are shown in Figure 2 right under corresponding force records, except rams 37 and 38 for which the speed histories are not available.
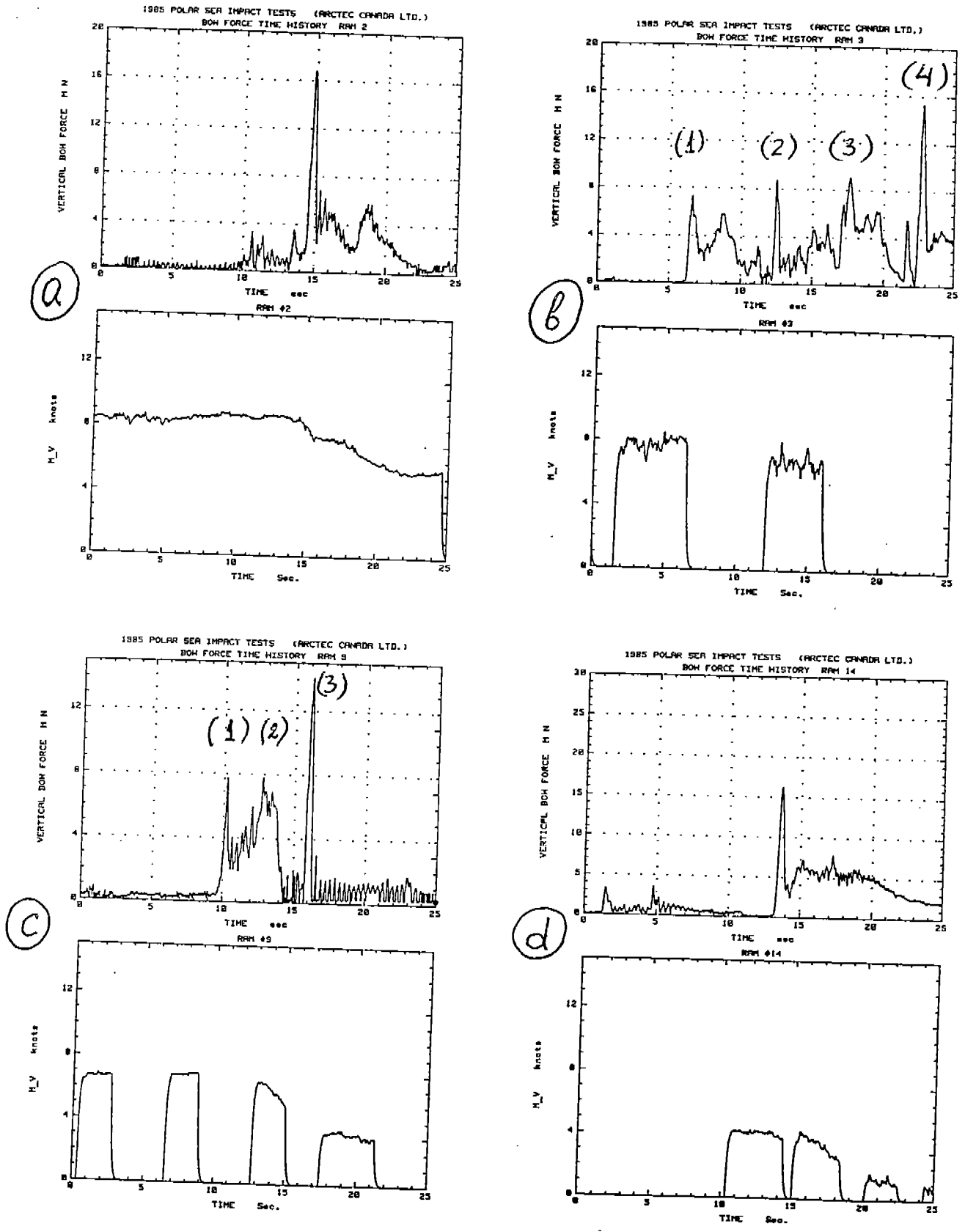
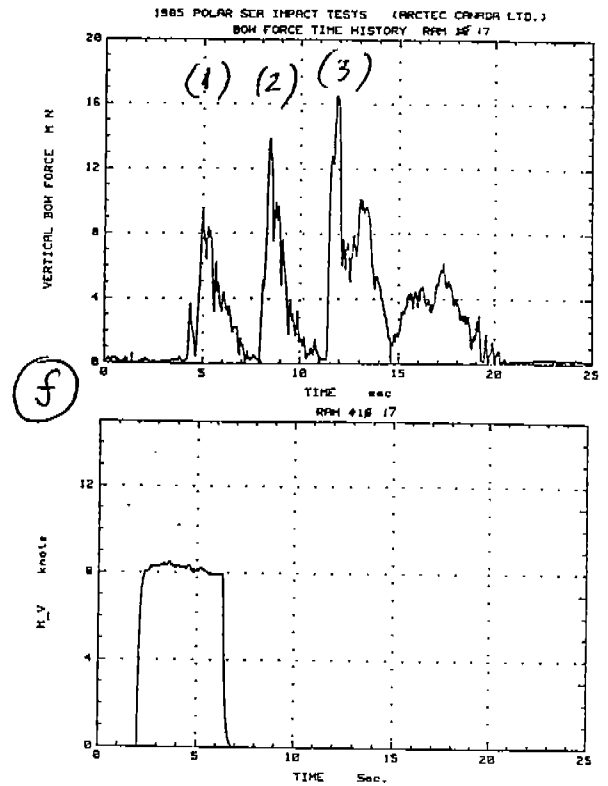Fig. 2 . Force and velocity histories of rams 2; 3; 9 and 14
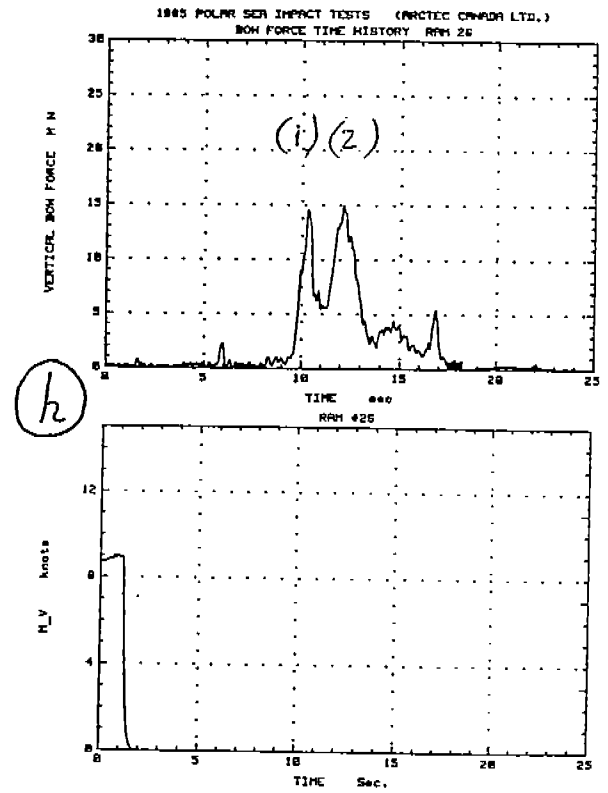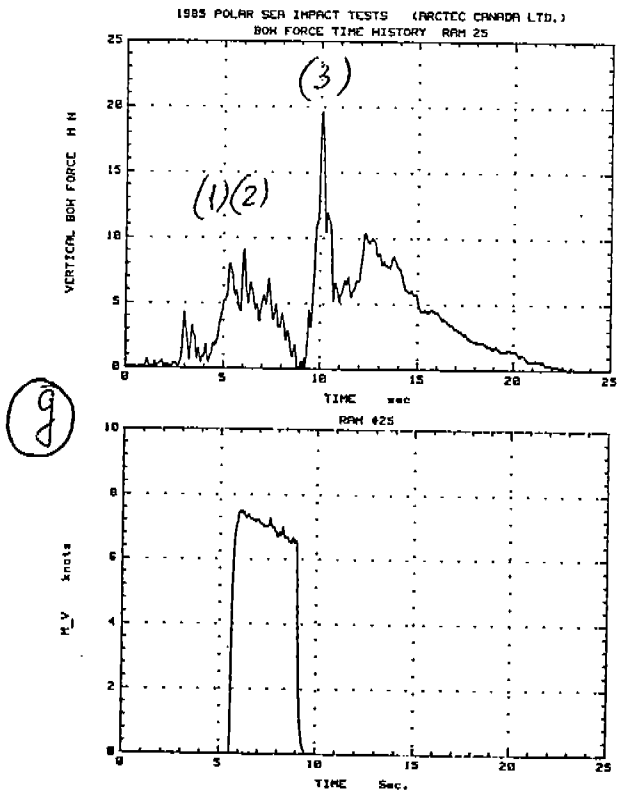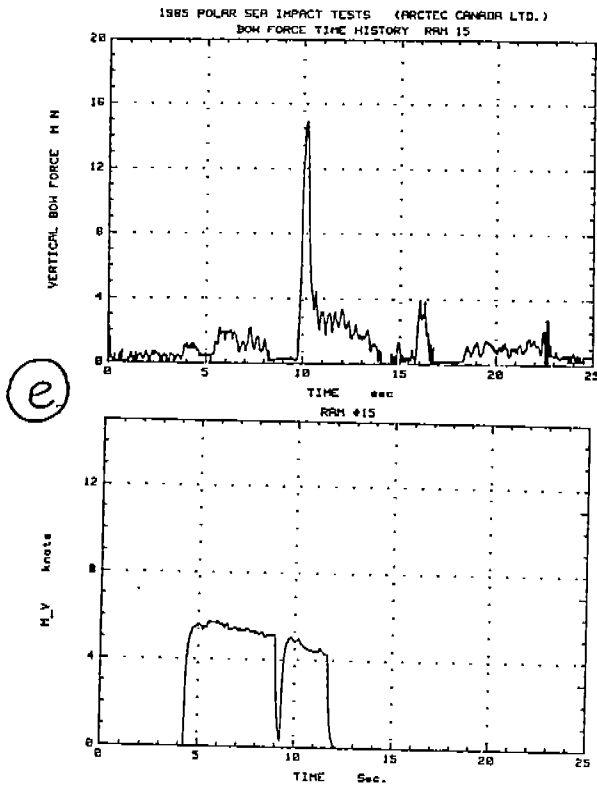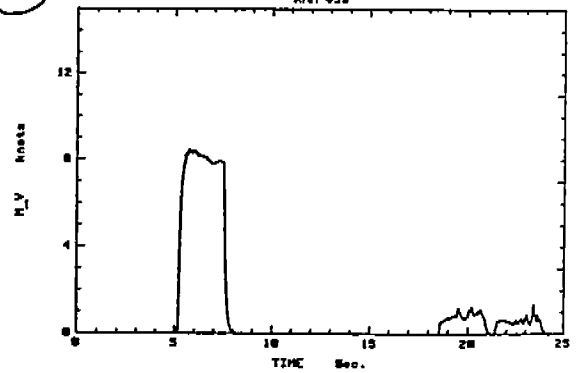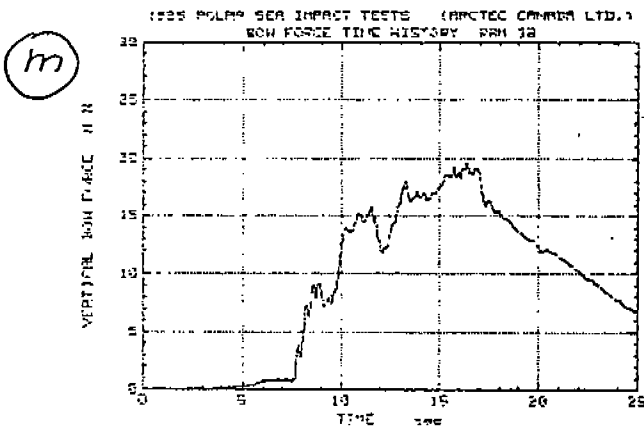
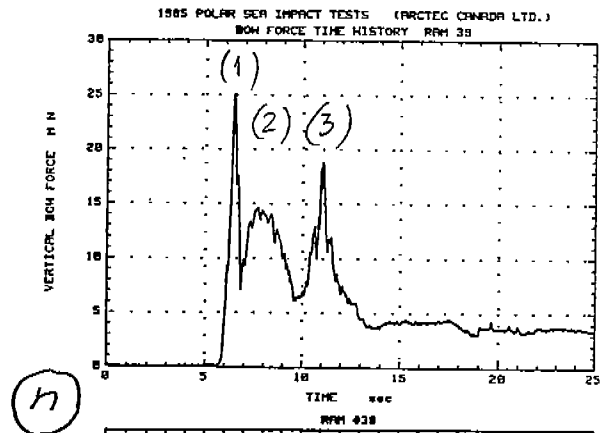Fig. 2 .   Force and velocity histories of rams 15; 17; 25 and 26
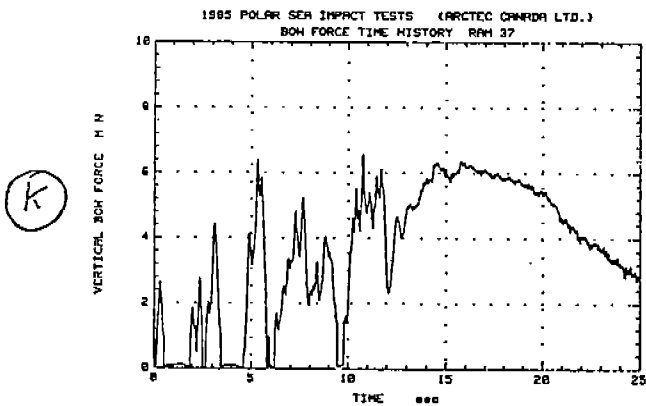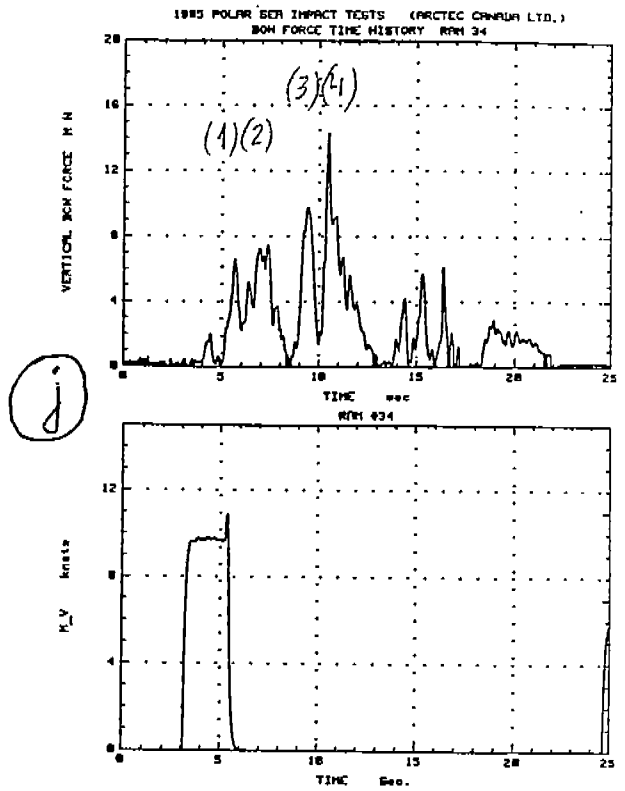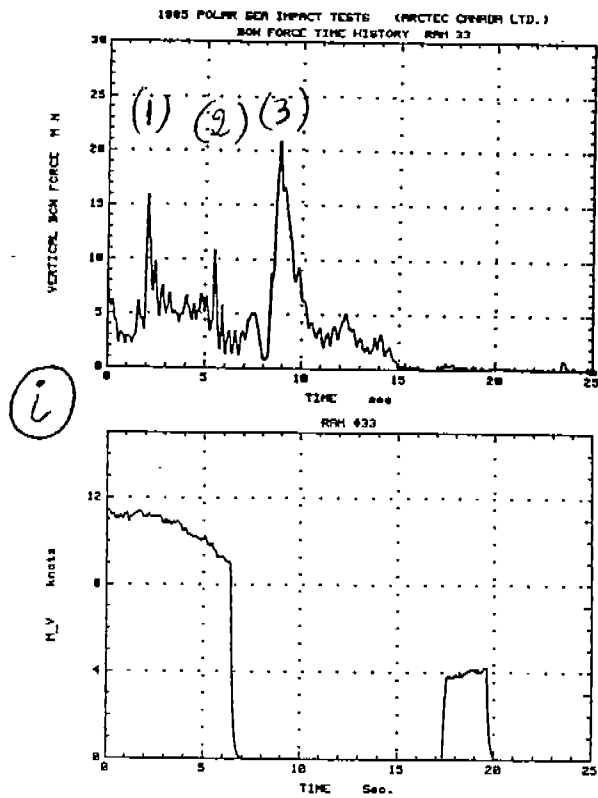
Fig. 2. Force and velocity histories of rams 33; 34; 37; 38 and 39
No velocity histories are available for rams 37 and 38

Doppler logs usually give reliable and sufficiently accurate information on ship speed in broken ice. However, the speed records shown in Fig. 2 contain certain contradictions. For a number of rams the speed records are interrupted (rams 3, 9, 14, 33, 34, 39). It is supposed that the drops occurred whenever the doppler radar failed to receive an echo. Probably the same cause can explain such speed records as those of rams 15, 17, 25, 26. With this explanation the speed records with relatively short-time drops could be somehow bridged. However, the accuracy of the bridged records would be questionable. At best, it can give only an estimate of the velocity changes after initial ship/ice contact. No such estimates are possible for rams 3, 15 ,17, 25, 26. For ram 34 the gap between the drops was almost 20 seconds during which time the effect of the propeller thrust on the speed can be noticeable. Therefore, only the initial speed data recorded prior to ship/ice ridge contact can be assumed reliable. The estimates made by bridging the velocity gaps should be treated cautiously and compared with the estimates based on other sources.

In addition, the radar measured only the horizontal speeds. Vertical and angular speed components (heaving and pitching) have not been measured; so were the accelerations. Therefore, the speed records do not provide sufficient data to describe the kinematics of the rams, which, in turn, makes it difficult to analyze the interaction forces. This is especially so at the post-impact beaching phase when the vertical components of bow speed are essential.

2.3 ANALYSIS OF THE GLOBAL FORCES

2.3.1 Analysis of the Force History Records

Each distinct peak on the force history records is considered to be a separate impact. All of the impacts are analyzed in accordance with equations (3) - (4). Fig. 3 shows a comparison of dimensionless force histories predicted theoretically (Fig. 1) and recorded (Fig. 2). The peak force records stretched in the time scale are normalized with respect to their maxima ($F = F/F_{max}$) and peak durations ($t = t/T$). The duration "T" of a peak force record is determined by fitting together the theoretical (Fig. 1) and recorded pulses. Fig. 4 shows individual comparisons of the dimensional peak forces with the force history curve of Fig. 1 dimensionalized with respect to the recorded maximum force and the duration (i.e. the maximum predicted forces are assumed equal to the recorded peaks).

As seen from Fig. 3 and 4 the theoretical model fairly well describes the impact process in time. For rams 2, 3-(1), 3-(4), 14, 15, 17-(2), 34-(3), 34-(4), and 39, the theoretical curve fits the records almost perfectly.

The force history records differ from the theoretical curve mainly at their lower ascending and descending branches. The beginning of impact interactions is often influenced by the ice features situated in front of the ridge, whereas the latest impact stage is influenced by the post-
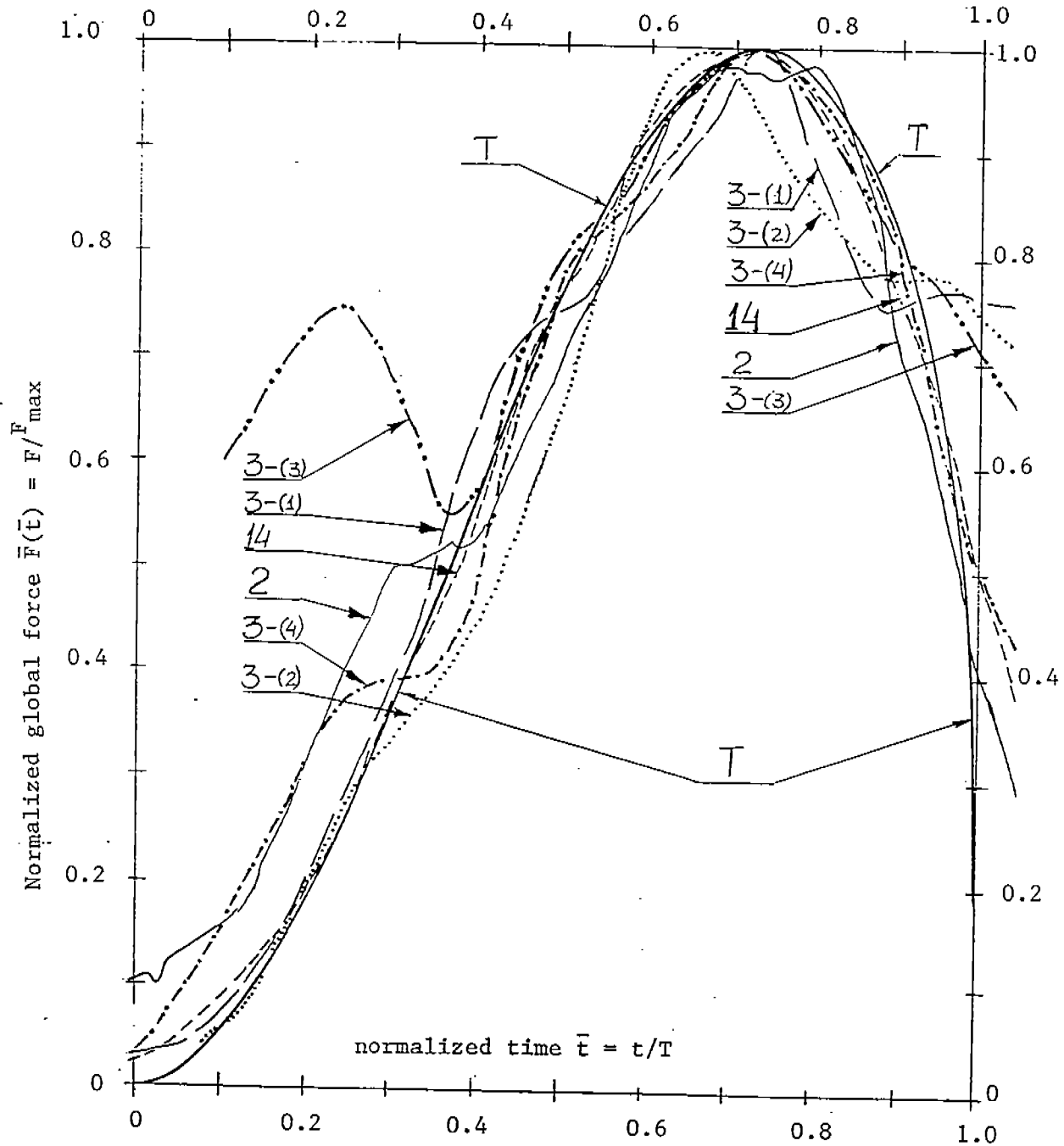
Fig. 3 Force history curves for separate rams and force peaks, normalized with respect to the force maxima and durations, and plotted together with the theoretical force history shown in Figure 1.
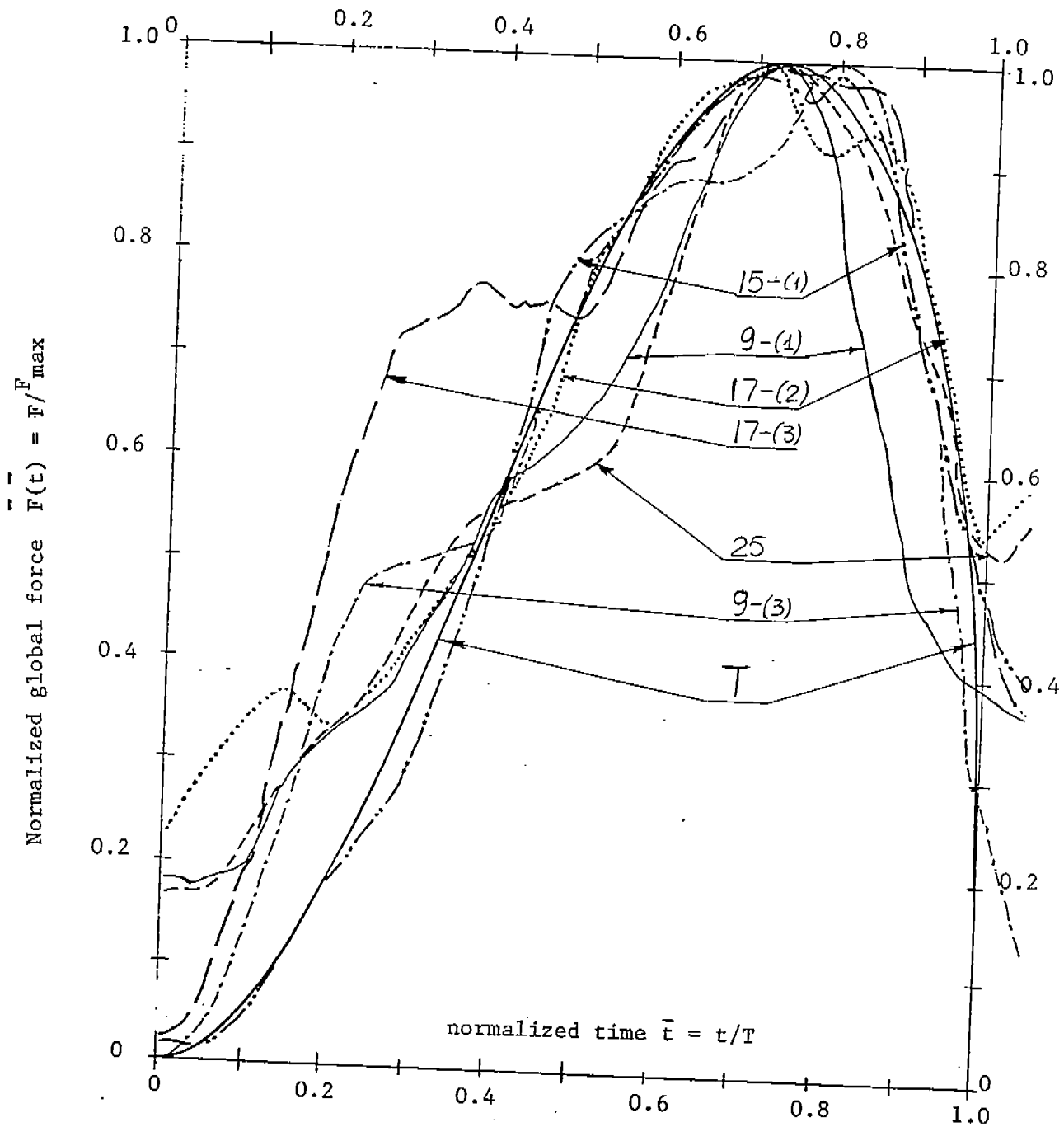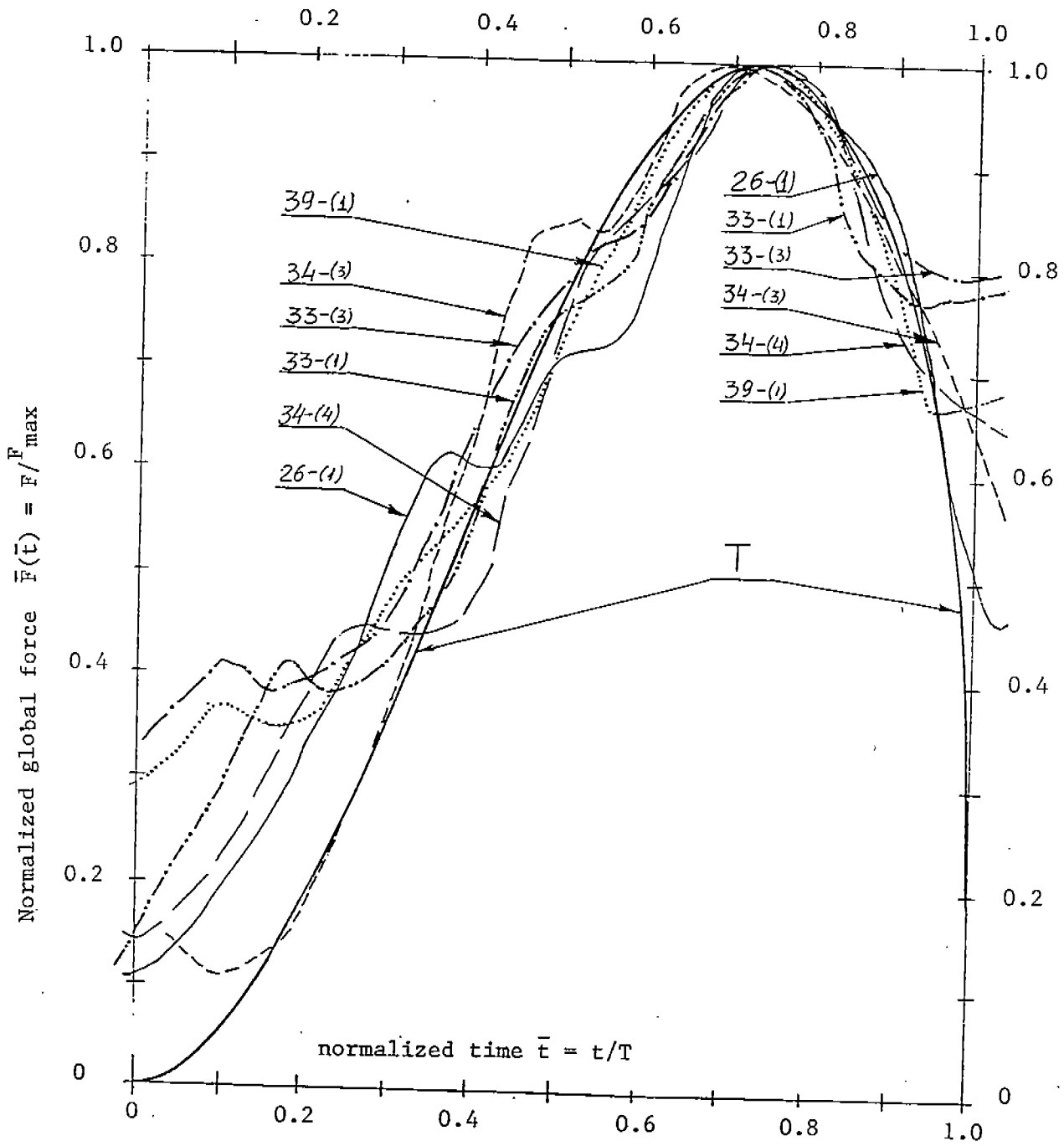
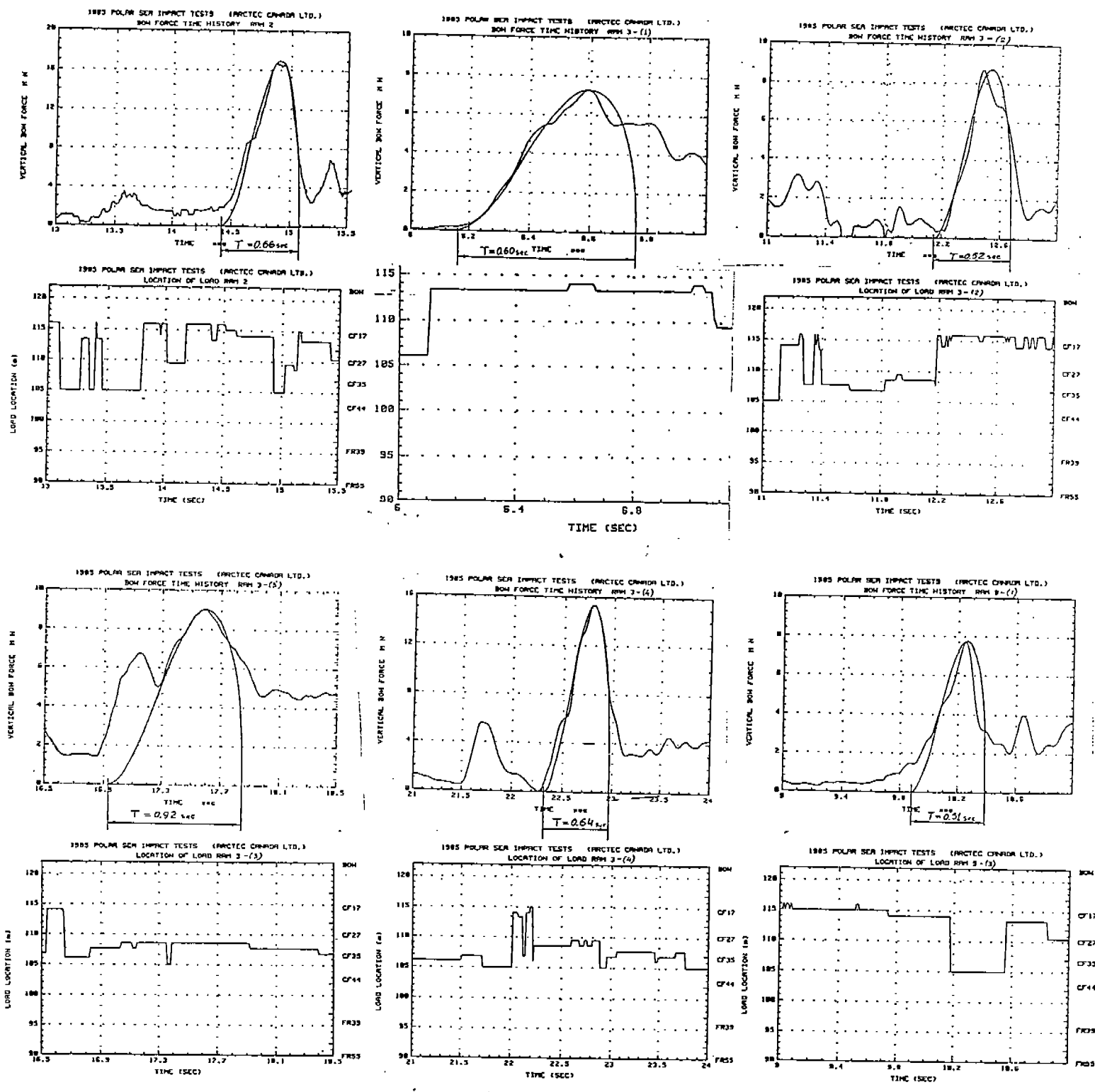Fig. 3 (continuation)

Fig. 3 (continuation)

Fig. 4 Recorded force histories as compared with the theoretical curve of
Fig. 1 dimensionalized with respect to the recorded peak force.
The load location records of the recorded peak forces are placed
below the corresponding force records at the same time scale.

Fig. 4   (continuation)

- 15 -
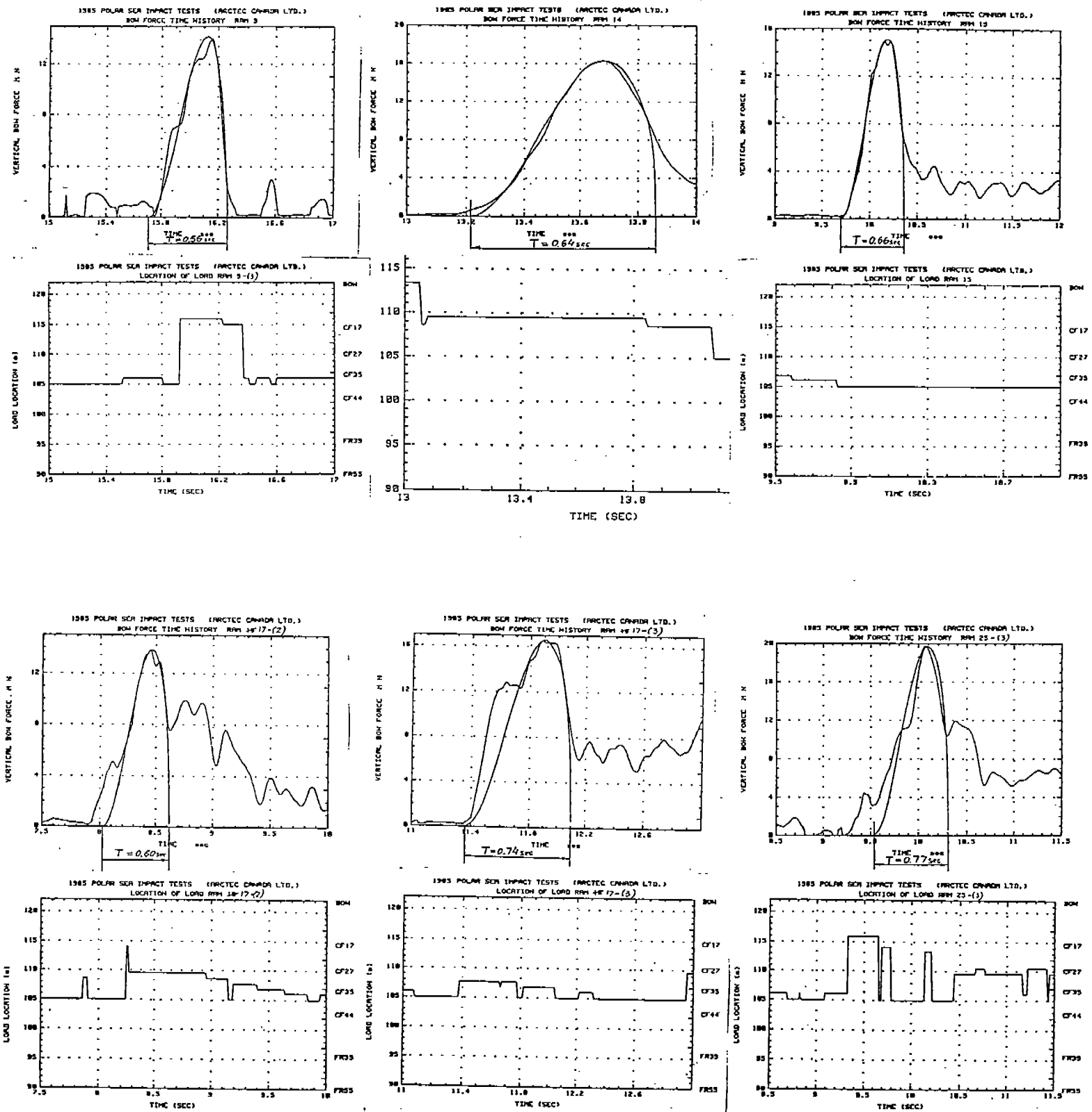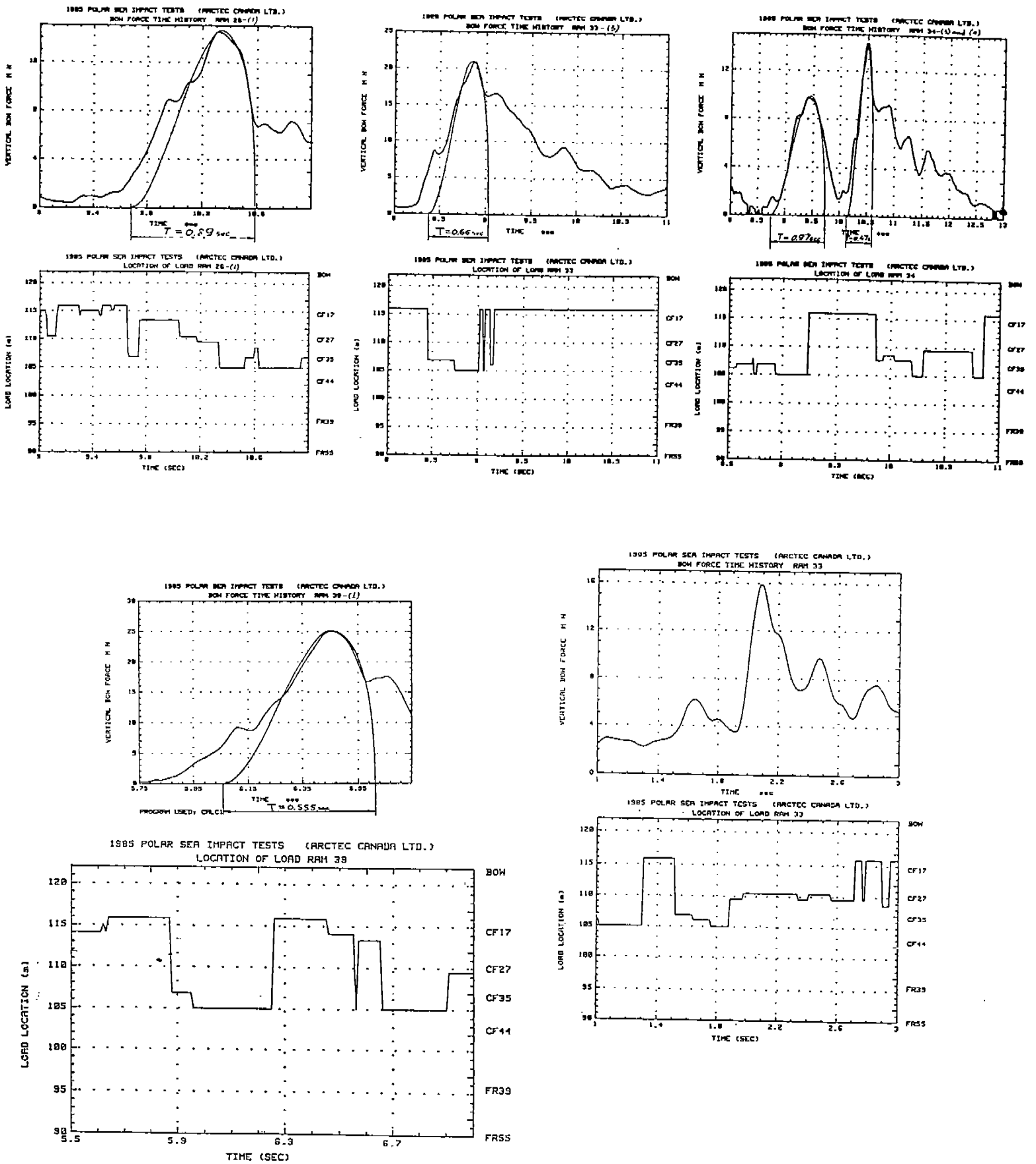
Fig. 4 (continuation)

impact sliding up on the ice (beaching phase). The records of rams 3-(2), 9-(1), 9-(3), 25-(3), 33-(3) also fit the curve but not as perfectly as formers. The records of rams 3-(3), 17-(3), 26-(1), 34-(3), 39-(1) have smaller peaks on its ascending branches which are apparently caused by failure of local ice blocks within the ridge being rammed. If these local peaks are shifted, the ascending and upper descending branches of these records would fit the theoretical curve much better.

Thus, the fact that the model is capable of describing the impacts in time domain enables one to use it for prediction of main impact parameters, namely forces, pressures, durations.

2.3.2 Ship Mass

The displacement of the Polar Sea was changing during the 10-day trial, so that at earlier rams (2 and 3) she was heavier by about 100-200 t as compared with the latest rams (37-39). However, this change makes up to 1-2% of the displacement. Since the records of actual drafts during the deployment are not available, a constant value of 110 $MN \cdot s^2/m$ (11,040 LT) is used in this analysis.

2.3.3 Bow Shape Factor

The bow shape factor S_b specified by equation (5) is a function of frame flare angle β and stem inclination angle φ. The two angles vary along the stem as shown in Fig. 5 whose data are obtained from the bow lines of the icebreaker (Fig. 6). Consequently, the factor S_b varies as plotted in Fig. 5. To use the values of the bow shape factor in eq. (5) it is necessary to specify the impact locations. The latter is assumed to be the location of maximum compressive strains in the centerplane web attached to the stem. The records of the maximum strain locations are shown in Fig. 4 in which the load location records are reproduced right below the corresponding force peaks. For a majority of the impact peaks, the load location was rather uncertain during the beginning of the impact, traveling sometimes along the whole stem length from CF15 to CF40 or vise versa. The load location uncertainty at the beginning stage can be explained by the influence of interactions with the ice features crushed moments before hitting the ridge. However, as soon as the interaction with the ridge itself becomes prevalent and the global force reaches 30-50% of its maximum, the load location stabilizes and remains permanent (or sometimes displaces within 2-3 cant frame spacings) at least until the global force begins to decline. This pattern is common for all peaks except 26-(1) and 33-(3) for which the maximum strain locations jumps from one to another end of the stem. The load locations stability implies that dynamic penetration into ice is predominant during this stage. The load location at the latest impact stage, when the global force rapidly declines, sometimes changes, as in peaks 2, 9-(1), 26-(1), 33-(3), 34-(3). Therefore, the load location
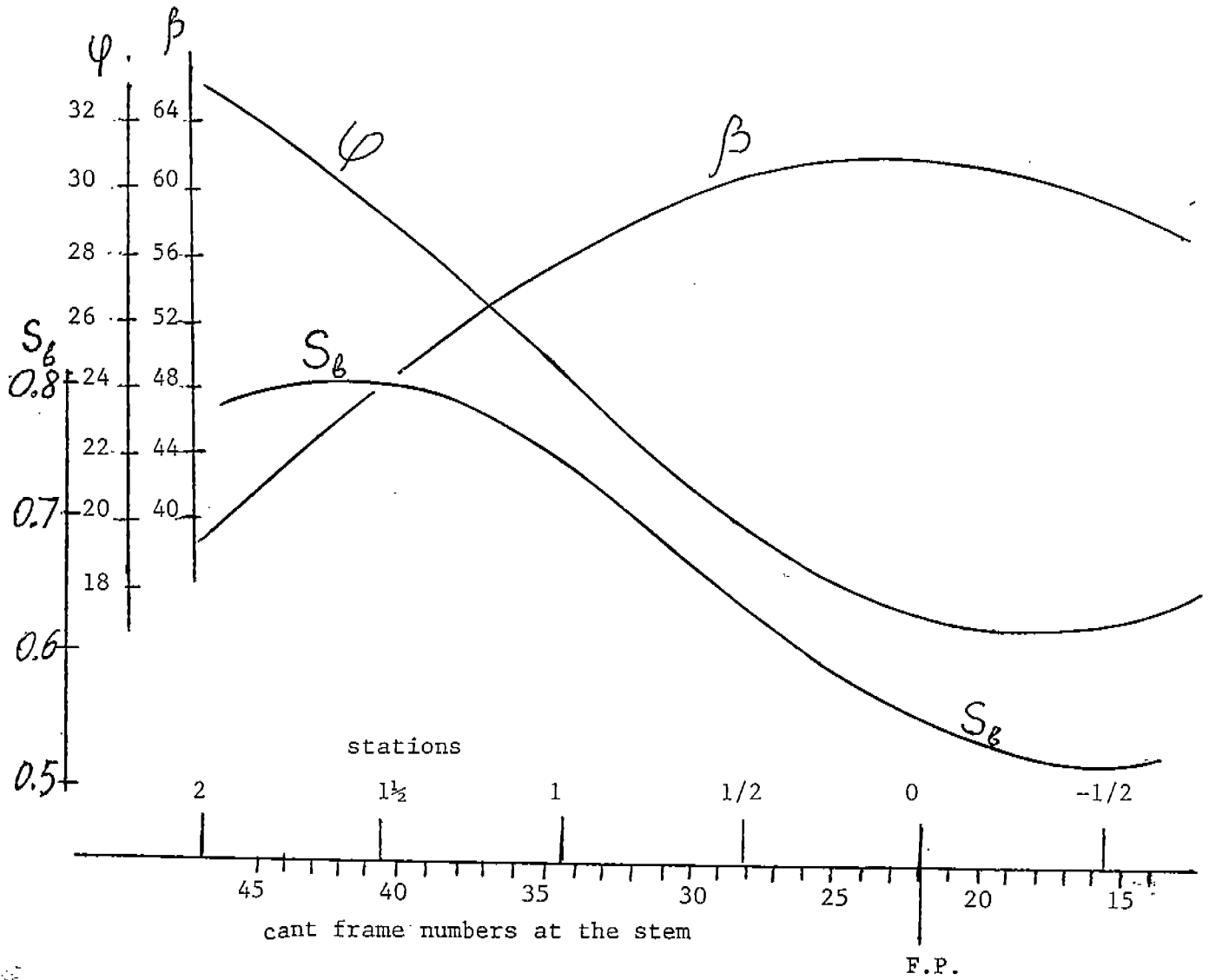
Fig. 5   Stem inclination angle "φ", frame flare angle "β",
and bow shape factor S_b along the ship bow length
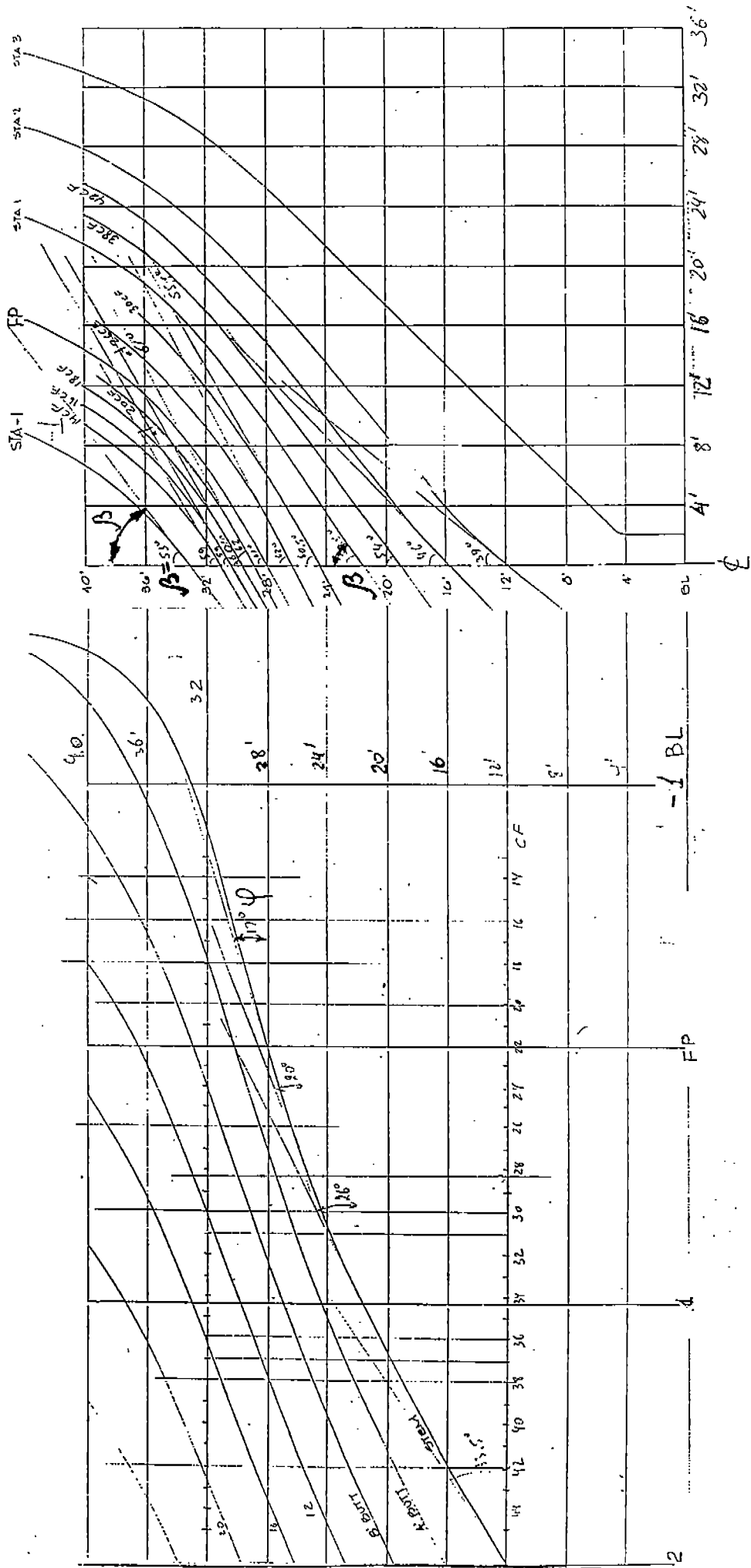for the POLAR SEA

Fig. 6. The bow lines of the POLAR SEA

φ – Stem inclination angle

β – Frame flare angle

TABLE 2

Global Force Locations & Bow Shape Factors in Accordance with Fig. 4 & 5

Ram & Peak	Load location CF #	Stem angle φ degrees	Flare angle β degrees	Bow Shape factor S_b (Fig. 5)	Comments
2	19	17	60.5	0.53	changes for CF40 at descending branch
3-(1)	21	17	62	0.55	
3-(2)	15-17	17	60	0.52	
3-(3)	30	21	60	0.67	
3-(4)	28-30	20.5	60.5	0.65	
9-(1)	40	29	49	0.80	changes from CF18 to CF40 at the middle of the peak
9-(3)	15	17	59	0.52	
14	28	20	61	0.63	
15-(1)	39	28	50	0.79	
17-(2)	28	20	61	0.63	
17-(3)	31-33	22.5	58.5	0.70	
25-(3)	37-38	27	52	0.78	
26-(1)	20-28	18	62	0.58	
33-(1)	26	19	62	0.61	
33-(3)	35-39	27	52.5	0.78	
34-(3)	39-15	19	62	0.61	changes from CF39 to CF15 at the middle of the peak
34-(4)	39-29	24	57	0.74	
39-(1)	15	17	59	0.52	

corresponding to the upper half of the ascending branch of the peak force is assumed to be the global force location. The force locations for the peaks shown in Fig. 4 are given in Table 2 with corresponding values of bow shape factor S_b.

2.3.4 Ice Ridge Shape

Although some of the rammed ridges have been surveyed and profiled at two or three sections, their shapes are somewhat uncertain and cannot be accurately described using one or several parameters. Moreover, the location and orientation of the ram can hardly be related to a particular profile. This fact together with the variability of ridge profiles, makes it very difficult, if not impossible, to specify the ridge shape accurately. Since the structure of equations (1)-(2) depends (though not very significantly) on the ice shapes, a certain idealization of the latter should be assumed. Equations (3)-(5) are derived assuming a rounded profile of a uniform cross-section ridge whose characteristic size R in equation (5) relates to ridge height. Keeping in mind that any idealization can be rather far from the real ridges being rammed, and taking into consideration the relatively low sensitivity of the total force to ridge shape variations, it is assumed here that parameter R is specified as:

$$R = 0.5 \ (Sail + Keel)$$
$$\text{but} \quad 4m \le R \le 8m.$$

When no information on the ridge being rammed is available $R = 6m$ is assumed. The values used in this analysis are given in Table 3 based on the survey data (see reference 18 of the Report).

TABLE 3

Ram #	Site #	Sail (m)	Keel (m)	R	$R^{3/11}$
2	2	4.0	7.0	5.5	1.59
3	3	3.4	6.1	4.7	1.53
9	-	--	--	6	1.63
14-15	5	3.3	9.1	6.2	1.64
17	6	5.6	14.0	8.0	1.76
25-26	7	4.8	14.4	8.0	1.76
33-39	-	--	--	6.0	1.63

2.3.5 Dynamic Crushing Strength of Ice

This parameter has not been measured during the tests. Its direct relationship with other strength characteristics of ice (e.g. with the compressive strength) has not yet been studied. A rough estimate of its approximate values can be found in [7, 8] based on analysis of laboratory tests [2, 3] and ship trials [5]. For autumnal first and second-year ice of the Northern Beaufort Sea, the estimate may vary from $A \approx 4$ to $A \approx 8 MPa(s/m^3)^{1/4}$. Since no particular data on its variations during the trial are available, a constant value of $A = 6MPa(s/m^3)^{1/4}$ is used for all rams.

2.3.6 Impact Velocities

Equations (1)-(2) are derived considering only that part of the kinetic energy of the ship penetrating into ice which is absorbed by ice crushing. It is associated with the change in the velocity component normal to the stem from its initial to final values. The latter is zero unless the ship breaks through the ice ridge. For the horizontal translational motion the relationship between the horizontal ship speed "V_k" and her speed component normal to the stem "V_R" is obvious (Fig.7):

$$V_n = V_h \, Sin \, \varphi \qquad (8)$$

Therefore, the impact force is expressed via the ship speed "V_h" designated as "V" in equations (1)-(2).

Ramming an ice ridge, formed by a number of ice blocks more or less tightly connected with each other, is a process consisting of one or several ice crushing impacts followed by beachings. The ram finishes when the ship either breaks through the ridge or is stopped on it and begins sliding back. When the initial phase (the impact) ends the ship gradually begins beaching up on the ice. The beaching motion is composed of translational and pitching motions. The velocity component normal to the stem (penetrating velocity) quickly diminishes to zero, and equation (8) is not valid during beaching. The resulting velocity of the ship bow "V_b" relates to its horizontal component "V_h" as follows (Fig. 7):

$$V_h = V_b \, Cos \, (\varphi - \gamma) \qquad (9)$$

where γ - pitching angle (Fig. 7)

The doppler radar used in the trial was directed to a distant reflector (an ice feature) measuring the horizontal speed only. These measured speeds (Fig. 2) can be associated with the impact velocity "V" used in equation (1)-(2) only when no pitching and/or heaving takes place, that

- 22 -

is at the beginning (or before) of the first impact peak and long after the ship broke through the ice ridge. Moreover, since the radar was located at the bridge, the bridge's own rotation due to pitching could be a source of significant errors during beachings (Fig. 7). As a result, intermediate readings might be inappropriate for the impact force analysis. For these reasons and due to the numerous gaps in the velocity records, the latter are used in the impact force analysis as follows. The difference between the initial ramming velocity recorded before the first peak and the final velocity of the ram is considered to be a total velocity loss due to all impacts (distinct peaks) within the ram. The velocity losses for each particular impact are estimated by substituting the recorded peak forces "F" and durations "T" (Fig. 2) into equation (4) solved for the velocity "V":

$$V = 0.1515 \ TF_v / Cos \ \varphi \tag{10}$$

The results of using such procedure to the distinct peaks in the force records are given in Table 4. The total velocity changes calculated for each ram "V_c" are close to those obtained from the initial and final readings - "V_r". For ram 34 it is unclear whether the velocity jump at the last second of the recorded period should be treated as the final speed. Similar question arises for ram 2. The mean V_c/V_r-ratio is 1.04.
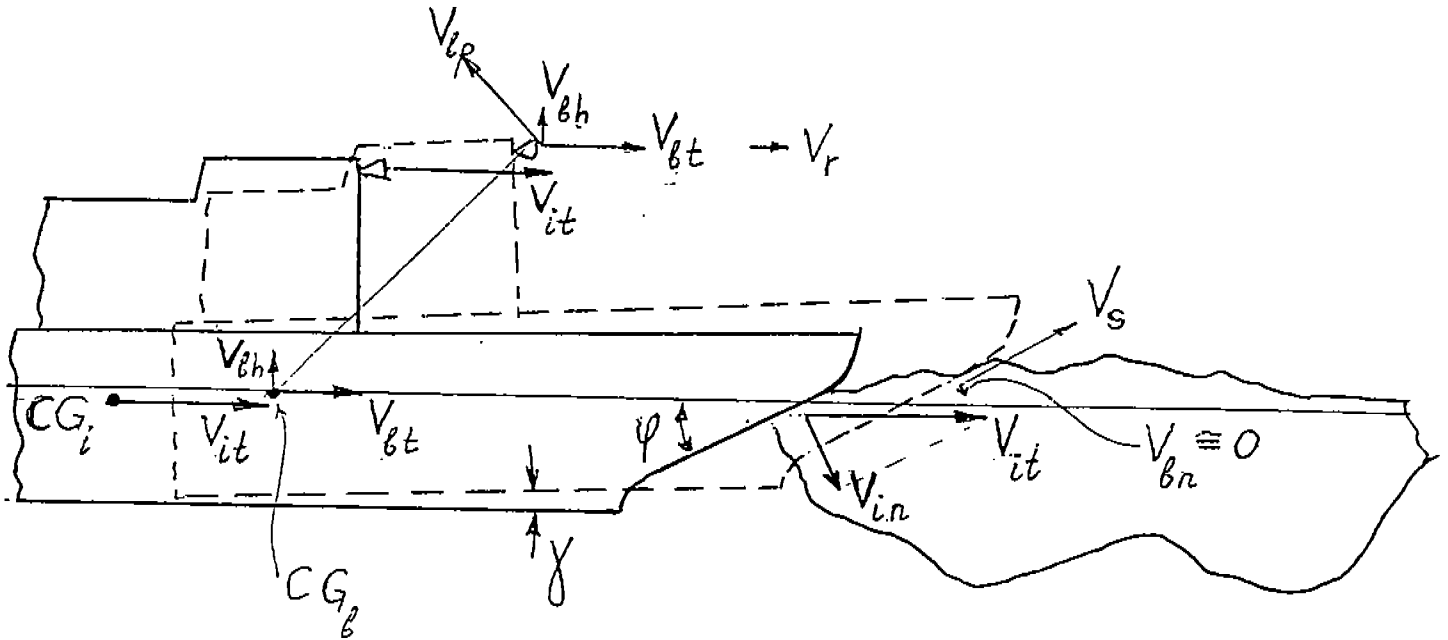
Fig. 7. Velocity Components at the Stem and the Radar
During The Impact and Beaching Phases of a Ram

◁   —   radar

CG —   center of gravity at the impact (CG_i) and beaching (CG_b) phases
γ —   pitching angle
φ —   stem inclination angle

Impact phase velocity components:

V_{it} —   translational (horizontal) velocity

V_{in} —   normal (penetration) velocity

Beaching phase velocity components:

V_{bt} —   translational (horizontal) velocity at the CG

$V_{bn} = 0$ —   normal (penetration) velocity at the stem

V_s —   sliding velocity

V_{bh} —   heaving velocity

V_{bp} —   pitching velocity of the radar

V_r —   horizontal velocity recorded by the radar

TABLE 4

Ram & Peak #	Recorded vertical force F_v, MN	Peak duration from records T, sec	Velocity change calculated using equation (10) V_c; m/s (kn)	Recorded velocity change for entire ram V_r, kn	V_c/V_r
2	16.9	0.66	1.80 (3.50)	3.2	1.09
3-(1)	7.3	0.60	0.69 (1.35)	-	-
3-(2)	8.65	0.52	0.75 (1.47)	-	-
3-(3)	9.0	0.92	1.35 (2.62)	-	-
3-(4)	15.3	0.64	1.59 (3.09)	-	-
Total for 3	-	-	4.23 (8.55)	8.5	1.01
9-(1)	7.8	0.51	0.69 (1.33)	-	-
9-(2)	7.8	0.5*	0.63 (1.22)	-	-
9-(3)	14.1	0.56	1.25 (2.43)	-	-
Total for 9	-	-	2.57 (4.98)	3.7	1.35
14	16.1	0.64	1.66 (3.23)	3.0	1.08
15-(1)	15.0	0.66	1.70 (3.30)	-	-
15-(2)	4.0	0.65*	0.42 (0.82)	-	-
Total for 15	-	-	2.12 (4.12)	5.4	0.77
17-(1)	9.5	1.0*	1.53 (2.98)	-	-
17-(2)	13.8	0.60	1.34 (2.60)	-	-
17-(3)	16.5	0.74	2.00 (3.90)	-	-
Total for 17	-	-	4.87 (9.48)	8.3	1.14
25-(1)	8.0	0.7*	0.90 (1.76)	-	-
25-(2)	9.2	0.4*	0.59 (1.15)	-	-
25-(3)	19.7	0.77	2.58 (5.02)	-	-
Total for 25	-	-	4.07 (7.93)	7.5	1.13
26-(1)	14.6	0.89	2.06 (4.02)	-	-
26-(2)	15.0	1.1*	2.66 (5.18)	-	-
Total for 26	-	-	4.72 (9.20)	9.0	1.02
33-(1)	15.9	0.5*	1.28 (2.49)	-	-
33-(2)	11.0	0.4*	0.71 (1.38)	-	-
33-(3)	21.0	0.66	2.35 (4.58)	-	-
Total for 33	-	-	4.34 (8.45)	7.7	1.07
34-(1)	6.5	0.55*	0.58 (1.12)	-	-
34-(2)	7.4	0.8 *	0.95 (1.86)	-	-
34-(3)	9.8	0.97	1.52 (2.96)	-	-
34-(4)	14.3	0.50	1.19 (2.31)	-	-
Total for 34	-	-	4.05 (8.25)	9.7/4.0	0.85/2.06
39-(1)	25.0	0.56	2.22 (4.32)	-	-
39-(2)	18.8	0.5*	1.52 (2.95)	-	-
Total for 39	-	-	3.74 (7.27)	7.5	0.97

*Peak duration was estimated, and its location was assumed to be at CF28

2.3.7 Impact Forces

The velocities calculated in Table 4 give a reasonable reconstruction of the total velocity losses for each ram. With a certain precaution they can be used as appropriate estimates of the velocities "V" in equation (3). The use of these estimates in equation (3) yields the peak forces prediction as given in Table 5. Only the peak forces with known location are included in Table 5. The best agreement between the predicted and recorded vertical forces takes place for the rams with a single distinct peak force. These are rams 2, 14, 15 for which the ratio of predicted-to-recorded vertical forces is, respectively, 0.89, 1.01 and 1.39. For rams with several impact peaks the ratio varies more significantly (mean value is 1.06 ± 0.40).

The peak forces calculated using the estimated speeds should consequently be treated as estimates which might be incorrect for particular impacts due to the incompleteness, variability and uncertainty of the environmental data (ridge shapes and ice strength characteristics). For example, the presence of several peaks on the force record of a ram implies that several consecutive impacts against separate (or loosely connected) ice feature took place during the ram.

Constant values of parameters R, A, S_b (characterizing the shape and size of the ice features and dynamic crushing strength of ice) are used in analyzing each of the peaks. However, in reality perhaps they varied significantly from block to block. Moreover, several rams were done sometimes at the same ridge but at different locations of the ridge (rams 14 and 15 at ridge 5; rams 25 and 26 at ridge 7). The ice data for these rams might also vary as much as for ridges in different geographic areas. These variations can be the sources of the apparent disagreements between predicted and recorded forces as seen in Table 5 for rams 3, 9 (ice data are completely unknown), 17, 25, and 26.

Table 5

	Force Calculated		Vertical Force recorded F_v;MN	$\dfrac{F\ calc}{F\ recorded}$
	F_n - using equation (10) MN	$F_v = F_n Cos\varphi$ MN		
2	15.78	15.09	16.9	0.89
3-(1)	4.26	4.08	7.3	0.56
3-(2)	4.51	4.32	8.65	0.50
3-(3)	12.88	12.03	9.0	1.34
3-(4)	15.64	14.65	15.3	0.96
9-(1)	6.60	5.78	7.8	0.74
9-(3)	9.65	9.23	14.1	0.65
14	17.32	16.28	16.1	1.01
15-(1)	22.44	19.81	15.0	1.32
17-(2)	13.88	13.05	13.8	0.95
17-(3)	26.63	24.60	16.5	1.49
25-(3)	42.00	38.80	19.7	1.97
26-(1)	22.97	21.85	14.6	1.50
33-(3)	25.46	22.69	21.0	1.08
34-(3)	14.78	13.98	9 8	1.43
34-(4)	12.84	11.73	14 3	0.82
39-(1)	21.12	20.20	25.0	0.81

THIS PAGE INTENTIONALLY LEFT BLANK

THIS PAGE INTENTIONALLY LEFT BLANK

3. HULL STRUCTURAL RESPONSE

3.1 Method of Analysis

The dynamic structural analysis was performed for the vessel ramming in ice at a head-on condition. This predicates a condition of symmetry about the centerline plane of the vessel, allowing the analysis to be performed on a model representing only one half of the ship, in this case the port side. No lateral or torsional response of the vessel was considered since the ice impact loads are expected to be approximately symmetric with respect to the centerline plane of the ship, and the lateral and torsional response is assumed to be insignificant.

The mathematical model has a fairly fine distribution of elements forward, and a much coaser distribution aft, with a smooth transition in between. This was done so that the dynamic response in the bow and fore body of the vessel could be determined with a reasonable degree of accuracy, while still providing a good representation of the stiffness and inertia characteristics of the entire vessel. An accurate representation of the hull girder structure is reflected in the calculation of the natural frequencies and mode shapes of the three-dimensional model.

The static characteristics of the vessel afloat were determined by using the ABS/SHIPMOM program for the calculation of the buoyancy springs. The output from SHIPMOM program was then used to determine the dynamic characteristics of the vessel for the calculation of added mass with the aid of the ABS/ADDMASS program, which is based on the linearized ideal fluid theory and the use of the boundary integral method.

The global ice impact loads for the vessel were determined based on the load analysis presented in the preceeding sections. The effects of internal and hydrodynamic damping were introduced in the pertinent calculations of structural response.

The free vibration characteristics and the dynamic response of the mathematical model to the ice impact loads were calculated by means of the SAP-V program. Details of the various steps, processes and aalculations are given in the following sections.

3.2 Mathematical Modeling

3.2.1 Three-dimensional Finite Element Model

A three-dimensional finite element model consisting of the port side of the entire vessel including the deckhouse was used for the dynamic response analysis. A fine mesh model of the fore end is connected through a transition segment amidships to a coarse mesh representation of the remainder of the vessel.

A judicious selection of nodes, elements and degrees of freedom was used to represent the elastic and inertia properties of the structure while keeping the complexity of the data generation and the size of the model within manageable limits. Lumping of plates and stiffeners, use of equivalent thicknesses and other such techniques were used for this purpose.

The structural elements, whose geometry, configuration and stiffness approximate the actual ship's structure, are of three types:

(a) Bar elements, with axial stiffness only and constant cross-sectional area.

(b) Three-dimensional beam elements, with axial, bi-directional shear, torsional and bi-directional bending stiffnesses (six degrees of freedom) and constant properties.

(c) Thin plate and shell elements, with bi-axial and in-plane shear stiffnesses and bi-directional bending stiffness and constant thickness, both triangular and quadrilateral in shape.

The buoyancy effect of the water on the ship was simulated by the introduction in the model of bar elements as buoyancy springs.

The finite element model has 35 transverse frames. An isometric view of the model is shown in Figure 3.1. The various sections of the model are shown in Appendix A. A summary of the characteristics of the model is shown below:

```
Number of nodes  ....................... 1383
Number of degrees of freedom  ......... 3651
Number of elements:
    Truss elements  .................... 960
    Beam elments  ..................... 805
    Plate elements  ................... 1954
                                        ─────
                        Total  ..... 3719
```
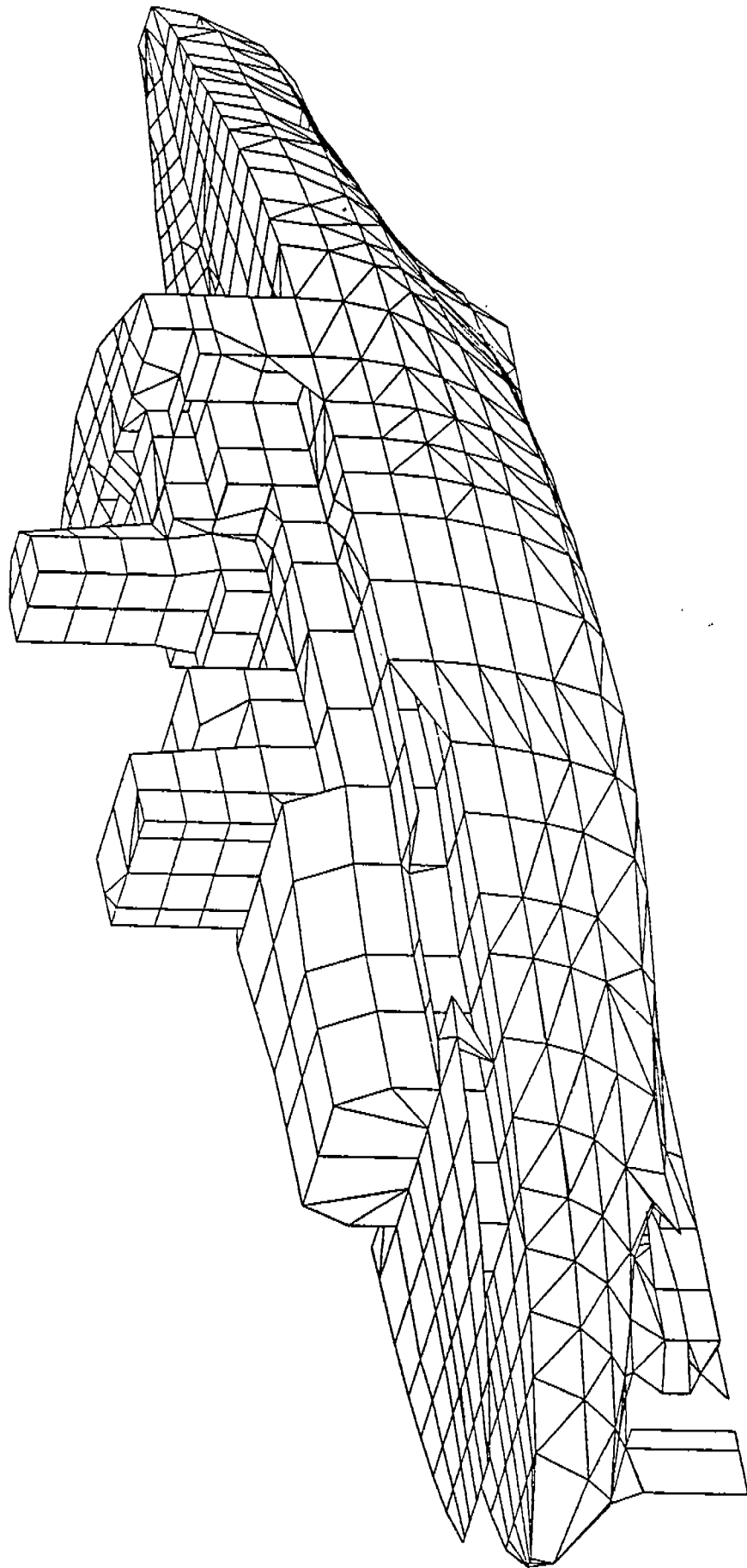
Figure 3.1 Isometric View of Finite Element Model

3.2.2 Buoyancy Springs

The effect of buoyancy of the water on the ship was simulated by introducing vertical springs whose stiffnesses are equivalent to the buoyancy effects at the corresponding ship stations. Each node located along the wetted surface of the ship connects to an axial bar, acting as a column, which is the equivalent of the buoyancy spring.

The equivalent vertical buoyancy stiffness at a ship station for a given draft is the vertical force necessary to produce a unit vertical deflection at that station. This stiffness can be expressed as

$$K = \rho BS$$

where

ρ = density of water
B = breadth of ship at waterline
S = station spacing

The stiffness of an axial bar acting as a column is given by

$$K' = AE/L$$

where

A = cross-sectional area of the bar
E = modulus of elasticity of the bar
L = length of the bar

Equating the two stiffnesses, we get

$$A = \rho BSL/E$$

All values of L are conveniently chosen as 24 inches in this study, and the modulus of elasticity of the bars chosen to match the modulus of elasticity of the ship structure, i.e., $E = 29. \times 10^6$ psi.

The cross-sectional area obtained from above is the total equivalent area at a ship station. This area is then distributed to the various nodes in contact with water, in approximate proportion to an effective transverse width associated with each node.

Table 3.1 shows the calculation of the equivalent areas of the buoyancy springs at the 35 stations of the mathematical model.

Table 3.1   Calculation Of Buoyancy Springs

Model Fr. No.	Ship Fr. No.	Spacing (in)	W.L. Beam (in)	Area (whole ship) (in**2 x 10**-5)
1	275	96.00	0.00	0.00
2	263	184.00	146.04	5.72
3	253	168.24	321.00	11.50
4	243	160.20	466.80	15.90
5	233	160.08	578.52	19.70
6	223	176.04	664.44	24.90
7	211	208.08	742.08	32.90
8	197	232.08	814.08	39.90
9	182	208.08	861.48	38.20
10	171	208.08	887.28	39.30
11	156	223.92	909.96	43.40
12	143	223.92	925.32	44.10
13	128	240.00	943.68	48.20
14	113	223.92	949.20	45.20
15	100	168.00	946.32	33.80
16	92	120.00	938.16	24.00
17	85	112.08	926.04	22.10
18	78	127.92	908.64	24.70
19	69	168.00	874.80	31.30
20	57	120.00	807.24	20.60
21	CF-75	72.00	785.76	12.00
22	CF-69	88.08	737.40	13.80
23	CF-64	103.92	691.80	15.30
24	CF-56	104.76	605.44	13.50
25	CF-51	82.08	545.76	9.54
26	CF-45	75.72	477.72	7.70
27	CF-41	69.60	416.88	6.18
28	CF-37	68.88	351.00	5.14
29	CF-33	68.88	279.72	4.10
30	CF-29	68.64	202.20	2.95
31	CF-25	67.56	138.12	1.99
32	CF-21	78.24	84.00	1.40
33	CF-16	88.08	0.00	0.00
34	CF-11	124.20	0.00	0.00
35	CF- 6	80.40	0.00	0.00

3.2.3 Boundary Conditions

The finite element model is supported vertically by the buoyancy springs at the various nodes in contact with water.

Along the centerline plane of the model, appropriate boundary conditions are required to account for the symmetric response, since only the port half of the hull structure was modelled. Namely, the degrees of freedom for all the nodes along the centerline plane should be specfied as follows:

Ux = 0, zero transverse dispacement
θy = 0, zero rotation about the vertical axis
θz = 0, zero rotation about the longitudinal axis

At the aft end, a spring with an arbitrary small stiffness value was used to support the model longitudinally, thus providing another necessary constraint for a statically stable mathematical model.

3.2.4 Loading Conditions

A total lightship, cargo and miscellaneous weight of 11,200 LT was included in the finite element model. This weight of 11,200 LT was the gross weight obtained by excluding 1859 LT of fuel used by vessel to get to the ice fields from the departing gross weight of 13,059 LT.

The concentrated loads of major machinery items and other equipment were directly lumped at the adjacent nodes. The masses corresponding to the cargo, fresh and drinking water, fuel oil and lubricant oil were distributed to the various nodes in the loaded area. The structural weight was taken into account by specifying a material density of the model that would result in the desired total lightship weight.

3.2.5 Hydrodynamic Added Mass

As the ship is vibrating, the hydrodynamic forces acting on the ship hull produce an effect equivalent to a very considerable increase in the the mass of ship, known as "added mass." In ship vibration analysis, the added mass should be properly taken into account since it is the same order of magnitude as the mass of the ship.

The added mass distributions were calculated for a draft of 28 feet by the ABS/ADDMASS program, which was developed based on the linearized ideal fluid theory, using the boundary integral method. The underwater hull geometry is ap-

proximated by contour lines at 35 longitudinal stations. Each contour line is represented by line segments, on which added mass contribution is found. This mass is then lumped at the corresponding nodal points of the finite element model in contact with water.

It is noted that the added mass calculated is the vertical component resulting from heaving oscillation only. No transverse and longitudinal components were included since lateral vibrations were not considered in the analysis and the longitidinal added mass is considered negligible in this case. The lumped values of the added mass for the 35 stations of the finite element model are shown in Table 3.2. The total values of the added mass in the vertical direction was found to be 63966 lb-sec²/in. which is equal to 98 percent of the total displacement of the loaded vessel.

3.2.6 Damping

The damping associated with ship hull vibration is generally considered as the combination of the following:

        (a) Structural damping
        (b) Cargo damping
        (c) Water friction
        (d) Pressure waves generation
        (e) Surface waves generation.

The formulation of expression for the damping forces poses a difficult problem that still requires extensive research. For practical purposes, however, it is assumed that the effects due to structural damping, water damping, water friction and pressure waves generation can be lumped together and the effect of surface waves generation can be neglected.

In this analysis, a damping value equal to 5 percent of critical damping was used. This value was divided into two factors proportional to the mass and stiffness matrices for use in the SAP-V program. The form of Rayleigh damping is:

$$[C] = \alpha [M] + \beta [K]$$

where

        $[C]$ = damping matrix
        $[M]$ = mass matrix
        $[K]$ = stiffness matrix
        α = mass-proportional damping factor
        β = stiffness-proportional damping factor

For a single mode response, the relation between the damping ratio and the two damping factors can be expressed as:

Table 3.2   Hydrodynamic Added Mass

Model Fr. No.	Ship Fr. No.	Spacing (in)	W.L. Beam (in)	M (whole ship) (lb-sec**2/in.)
1	275	96.00	0.00	0.00
2	263	184.00	146.04	83.30
3	253	168.24	321.00	374.31
4	243	160.20	466.80	787.31
5	233	160.08	578.52	1258.60
6	223	176.04	664.44	1820.10
7	211	208.08	742.08	2724.00
8	197	232.08	814.08	3689.30
9	182	208.08	861.48	3911.80
10	171	208.08	887.28	4361.80
11	156	223.92	909.96	5180.00
12	143	223.92	925.32	5496.40
13	128	240.00	943.68	6153.00
14	113	223.92	949.20	5678.20
15	100	168.00	946.32	4151.70
16	92	120.00	938.16	2874.40
17	85	112.08	926.04	2550.50
18	78	127.92	908.64	2714.90
19	69	168.00	874.80	3116.30
20	57	120.00	807.24	1727.20
21	CF-75	72.00	785.76	958.11
22	CF-69	88.08	737.40	1009.20
23	CF-64	103.92	691.80	1031.00
24	CF-56	104.76	605.44	804.94
25	CF-51	82.08	545.76	511.23
26	CF-45	75.72	477.72	365.25
27	CF-41	69.60	416.88	250.91
28	CF-37	68.88	351.00	178.92
29	CF-33	68.88	279.72	109.32
30	CF-29	68.64	202.20	57.18
31	CF-25	67.56	138.12	26.31
32	CF-21	78.24	84.00	10.76
33	CF-16	88.08	0.00	0.00
34	CF-11	124.20	0.00	0.00
35	CF- 6	80.40	0.00	0.00
Total				63966.25

$$\zeta \;=\; (\alpha \,/\, 2\omega) \;+\; (\beta\,\omega\,/2)$$

It is assumed that one half of the damping ratio is mass-dependent and the other half is stiffness-dependent. The α and β damping factors were calculated for the ratio of critical damping ζ equals to 0.05. With the frequency ω of 19.2 rad/sec (3.06 Hz) which corresponds to the two node bending mode of the hull girder, the α and β damping factors were found to be 0.9605 and 0.0026 respectively.

3.3 Free Vibration Analysis

The finite element model with 3651 degrees of freedom representing the hull structure has the same number of natural frequencies and corresponding mode shapes, which may be obtained by solving the generalized eigenvalue problem represented by the equation :

$$[K]\{\phi\} = \omega^2 [M]\{\phi\}$$

where

$[K]$ = symmetrical square stiffness matrix
$[M]$ = diagonal mass matrix
$\{\phi\}$ = column mode shape matrix
ω = natural frequency

This problem of free vibration was solved by means of the SAP-V computer program using a subspace iteration solution.

The lowest 10 modes of the vibration of the ship hull for the specified draft of 28 feet have the following characteristics :

MODE No.	NATURAL FREQUENCY (Hz)	PERIOD (sec)	REMAKRS
1	0.02	62.29	Rigid Body Surge
2	0.45	2.21	Rigid Body Heave
3	0.50	1.99	Rigid Body Pitch
4	3.06	0.33	2-Node Bending
5	5.54	0.18	3-Node Bending
6	7.75	0.13	4-Node Bending
7	9.81	0.10	5-Node Bending
8	10.20	0.098	Deckhouse
9	11.86	0.084	
10	12.60	0.079	

The mode shapes corresponding to the above 10 modes are shown in Figure 3.2. The same scale was used for the internally orthonormalized eigenvectors.

It can be seen from these plots that the first three modes represent the rigid body motions, namely, surge, heave and pitch. The remaining modes represent the elastic deformations.

-39-
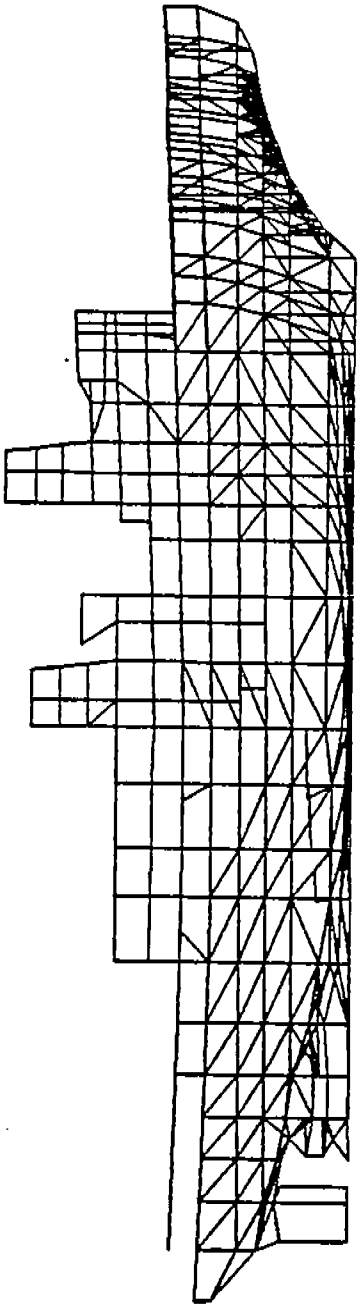
Mode 1 — Surge
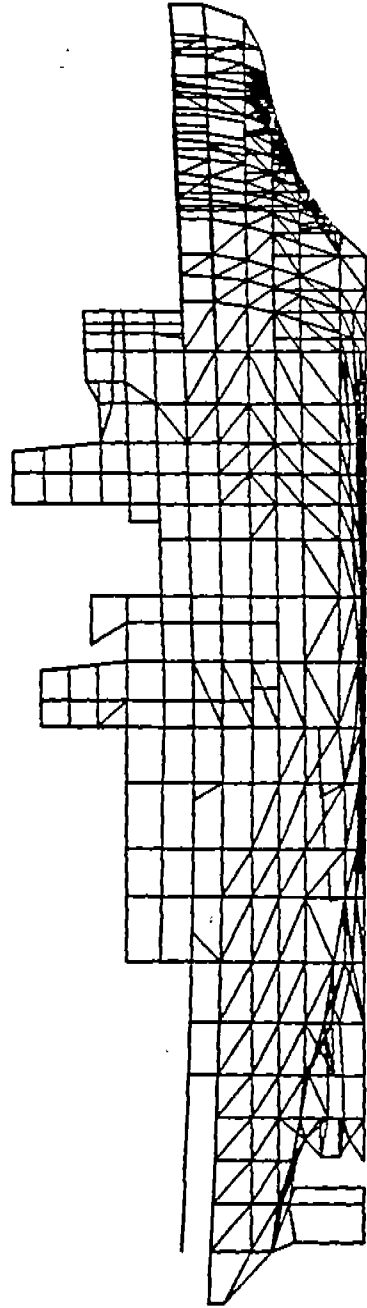
Mode 2 — Heave

Figure 3.2 Vibration Mode Shapes
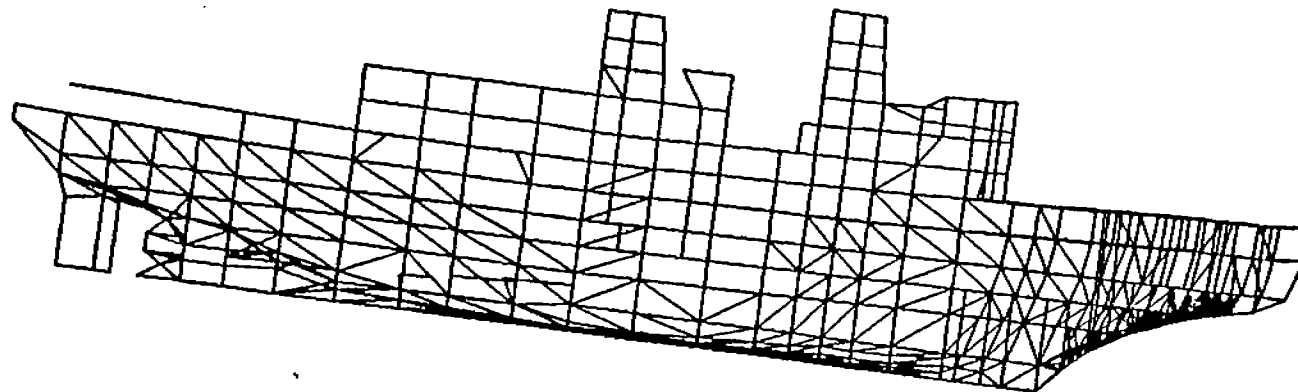
Mode 3 - Pitch

Mode 4 - 2-Node Bending (3.06 Hz)
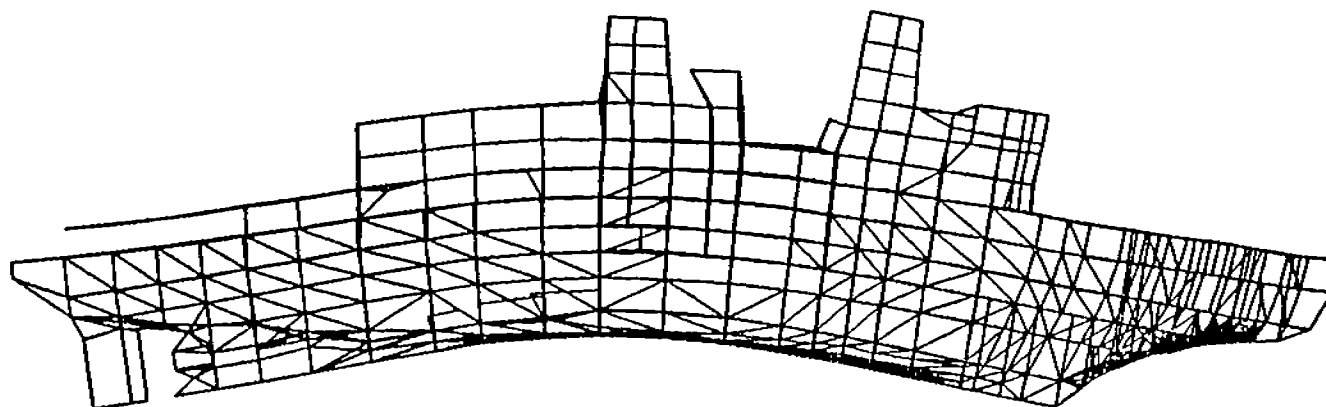
Figure 3.2 Vibration Mode Shapes (continued)
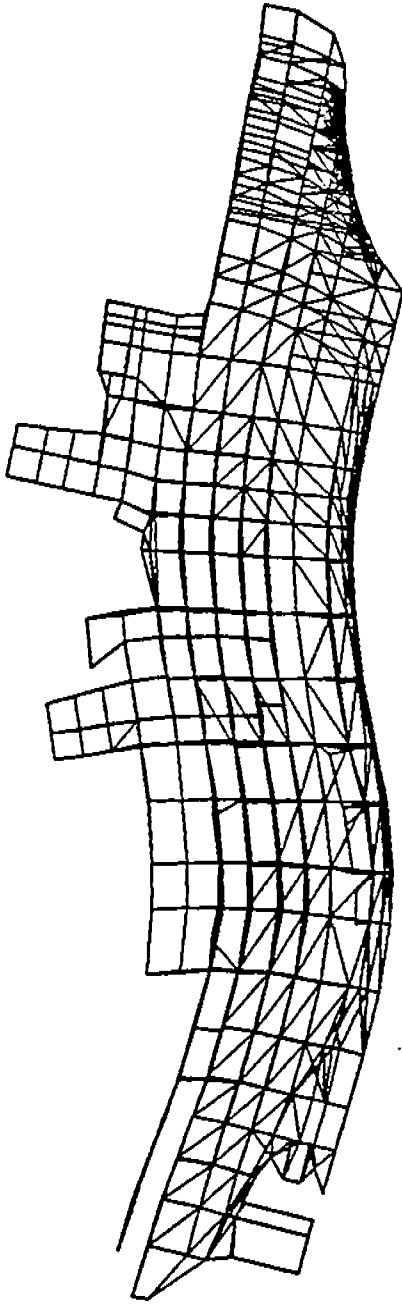
Mode 5 - 3-Node Bending (5.54 Hz)
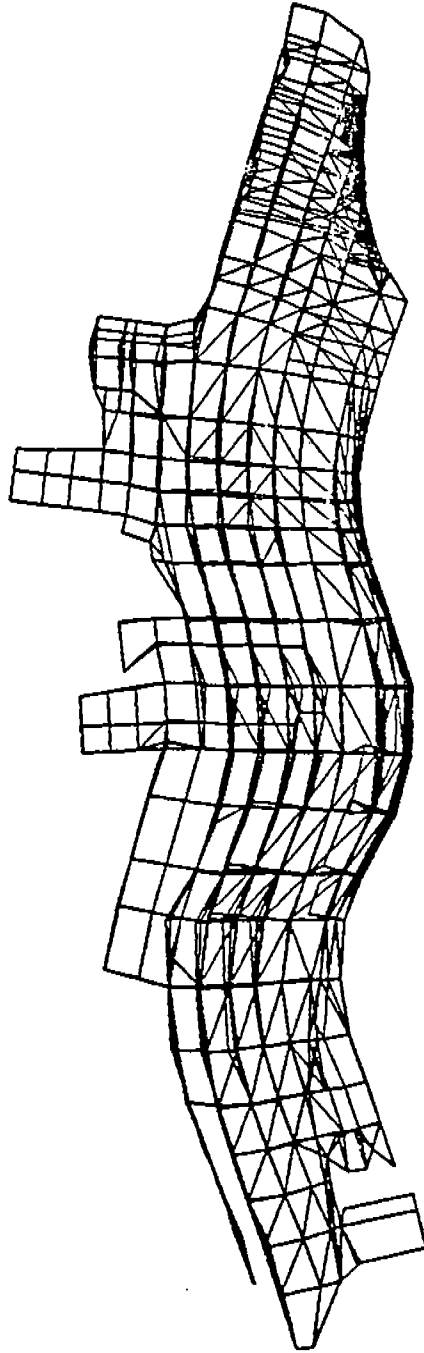
Mode 6 - 4-Node Bending (7.75 Hz)

Figure 3.2 Vibration Mode Shapes (continued)
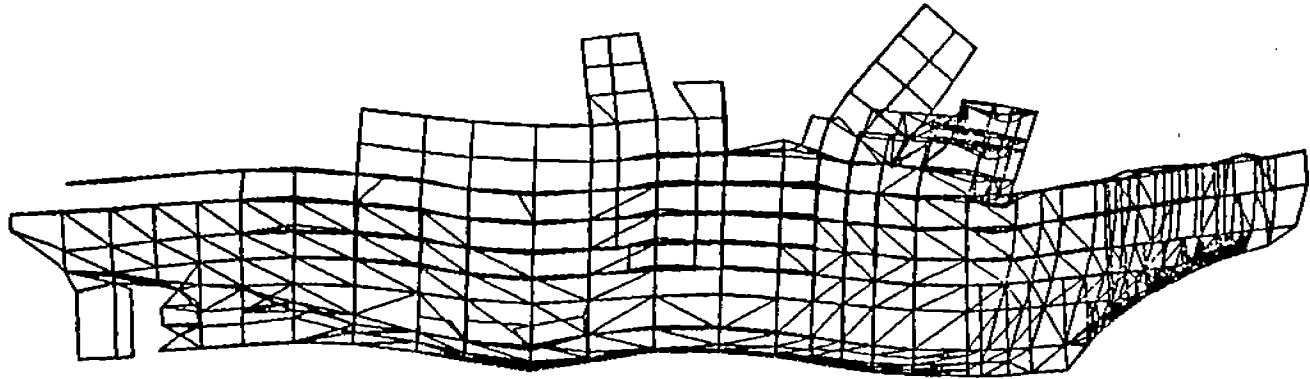
Mode 7 - 5-Node Bending (9.81 Hz)

Mode 8 - Deckhouse (10.20 Hz)
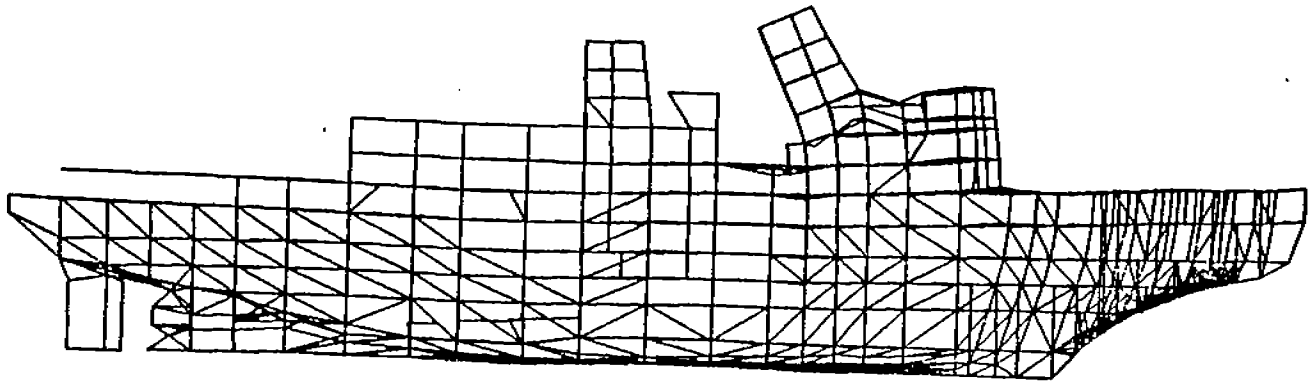
Figure 3.2   Vibration Mode Shapes (continued)
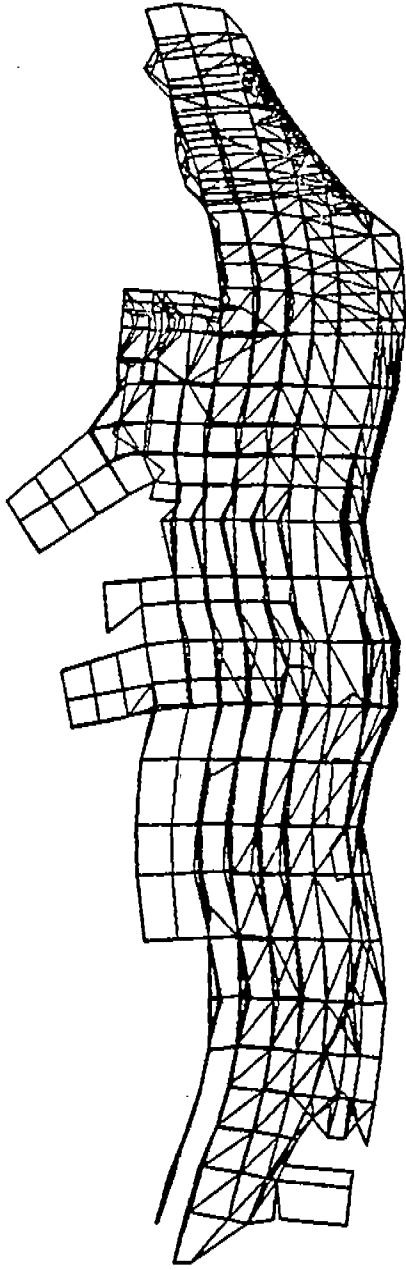
Mode 9 — (11.86 Hz)
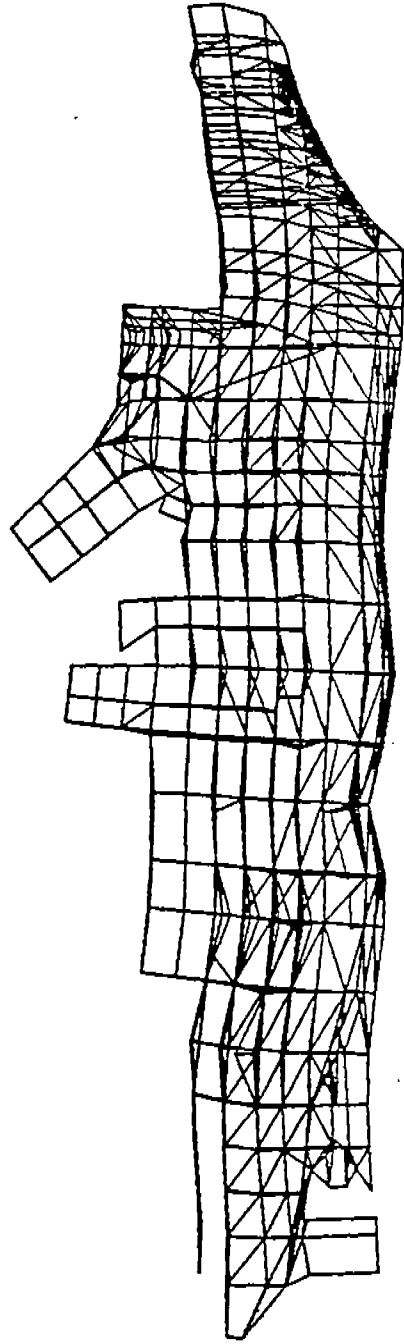
Mode 10 — (12.60 Hz)

Figure 3.2 Vibration Mode Shapes (continued)

The lower elastic modes, fourth to seventh modes, correspond basically to the hull girder's 2-node to 5-node vertical bending vibrations. The higher modes indicate hull girder vibration coupled with deckhouse and local vibrations and must be understood as representing the response of a three-dimensional finite element model as opposed to the usual free-free beam representation of the ship.

3.4 Dynamic Structural Analysis

3.4.1 Problem Formulation

The finite element model of the vessel is subject to time varying loads which represent the impact loads induced by ramming multi-year ice.

The dynamic response is obtained by applying the time varying bow forces to the model and solving the resulting dynamic problem given by the following equations of motion.

$$[M]\{\ddot{u}(t)\} + [C]\{\dot{u}(t)\} + [K]\{u(t)\} = \{F(t)\}$$

where

$[C]$ = damping matrix
$\{\ddot{u}\}$ = column matrix of accelerations
$\{\dot{u}\}$ = column matrix of velocities
$\{u\}$ = column matrix of displacements
$\{F\}$ = column matrix of applied forces

The structural response to this impact loads is of transient in nature. Response time histories for selected nodal displacements and element stresses of interest can be obtained. The problem was solved by the SAP-V computer program using direct integration by the Wilson θ-method, which is unconditionally stable [9].

-46-

3.4.2 Ice Impact Loads

Ice impact loads applied to the structure were represented by time varying loads. In the present study, calculations using different forcing functions were performed first for purposes of comparing the dynamic response of the hull structure. A total of nine loadcases were selected for the dynamic analysis:

Load case 1   Triangular shape
               Load at location A between cant frames 21 and 25
Load case 2   Concave trigonometric curve
               Load at location A between cant frames 21 and 25
Load case 3   Convex trigonometric curve
               Load at location A between cant frames 21 and 25
Load case 4   ABS theoretical bow force curve
               Load at location A between cant frames 21 and 25
Load case 5   Ram 39 measured bow force
               Load at location A between cant frames 21 and 25
Load case 6   Ram 39 measured bow force
               Load at location B between cant frames 41 and 45
Load case 7   Ram 39 measured bow force
               Moving load from location A to location C
Load case 8   Ram 14 measured bow force
               Load at location D between cant frames 25 and 29
Load case 9   Ram 14 measured bow force
               Load at location C between cant frames 33 and 37

The first three cases were based on predefined forcing functions as shown in Figure 3.3. For these forcing functions, the total duration of the load was assumed to be 1 second. The time to reach the peak value was chosen to be at 0.667 second. The peak value of the unit impact loads was assumed to be 2 MN (449 kips).

The time function for load case 1 corresponds to a triangular shape and that for load cases 2 and 3 has a distribution in the form of concave and convex trigonmetric curves, respectively. The area under the load time history curve represents the energy content of the impact load. By having the three shapes of forcing function as defined above, it is anticipated that as compared to load case 1, load case 3 has a higher energy content of impact whereas load case 2 has a lower energy content.

Load case 4 uses the ABS analytical bow force history curve shown in Figure 3.4. Similar to the first three cases, the duration of the impact load was taken as 1 second. However, the time to reach the peak force in this case was 0.728 second and the peak value of bow force was assumed to be 2 MN.

Based on the measured time histories of bow forces, it was noted that in each of the ramming tests, there were several waves of impact during the measured time of 25 seconds. Each rise and fall of the force was considered to be a wave of impact. From the measured data, the time duration of impact was about 1 second for the first wave of impact before the next wave of impact. Consequently,
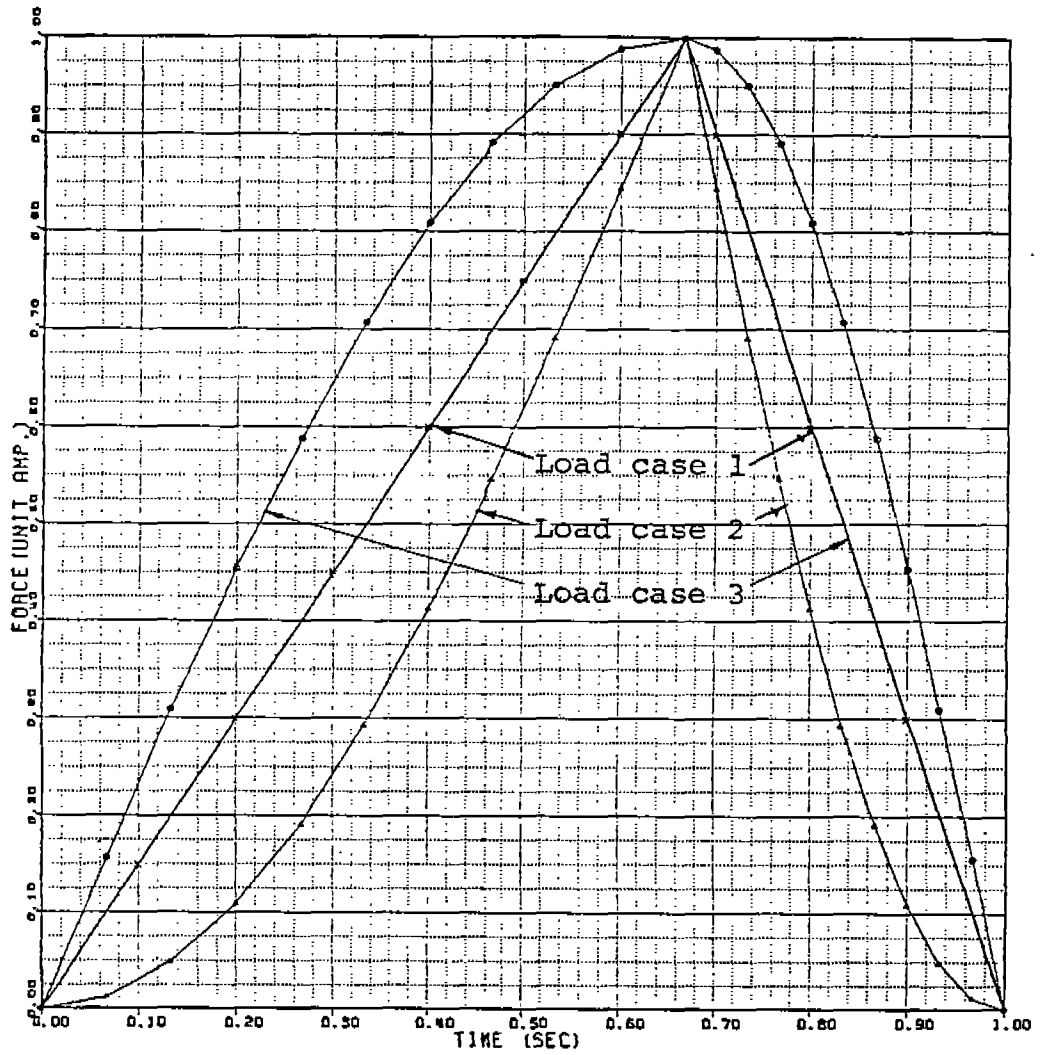
Figure 3.3   Predefined forcing functions for
load cases 1, 2 and 3

-48-
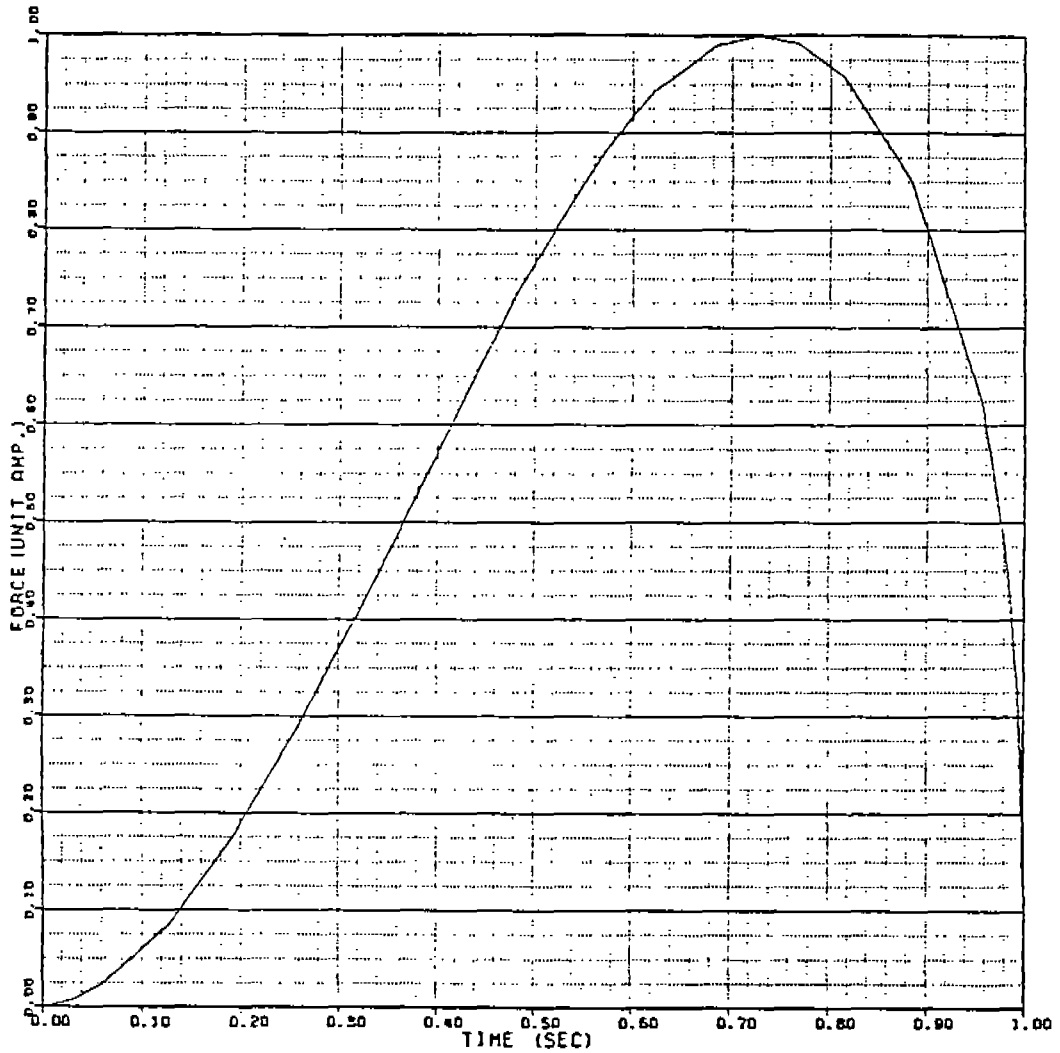
Figure 3.4   ABS analytical bow force history
for load case 4

-49-

in the above four case studies, only one wave of impact having a duration of 1 second was considered. The force level was maintained at zero at the end of the 1 second impacts and the analysis was carried out for additional 2 seconds to obtain the dynamic response of the structure after the impact ended. The location of the impact bow forces for all four load cases was assumed to be at between cant frames 21 and 25 and designated as location A in Figure 3.5. The total load was evenly distributed into 5 nodal points along the center line in the finite element model.

In the second category, the dynamic response was obtained using the acutal bow force time histories recorded during the ice-impact tests of the polar sea. Two cases, namely, Ram 14 and Ram 39 were considered in this study. Ram 39 was chosen in the analysis because it has the highest peak value of the bow force among the 40 rams recorded. Furthermore, the bow force time history indicates that a peak force of 25 MN occurs at the first wave of impact following immediately with very small values of subsequent waves. Other rams showed that the peak bow forces often did not occur in the first wave impact and if it did occur, the peak forces were much lower in magnitude.

For each ramming, the total duration for the bow force measurement was 25 seconds. However, due to the SAP-V program limitation, the dynamic analysis was performed for the initial 3 to 5 seconds only, depending on the size of the time-step used in the analysis.

Using Ram 39 data, three load cases were performed with different locations of the application of the bow force. The location of bow force for load case 5 was the same as in the previous load cases (location A) whereas the location for load case 6 was between cant frames 41 to 45, designated as location B in Figure 3.5. Load case 7 uses a moving load. Initially, the location of the bow force was between cant frames 21 to 25 and the load moved during the loading process. The velocity of the impact load was taken as 4.4 m/sec. The duration of the moving load was 1.2 seconds such that the final position of the load ended between cant frames 33 and 37 (location C in Figure 3.5).

For load cases 5 and 6, the analysis was carried out for 300 time steps with a timestep size of 0.016 second for a total of 4.8 seconds. During the initial 2.4 seconds, the bow force followed the shape the record between 5.6 to 8.0 second for Ram 39. After that, the load was held constant at 14 MN for another 2.4 seconds period.

As for load case 7, the moving bow force lasted for 1.2 seconds. After the initial 1.2 seconds, the load was held at a constant value of 7 MN and was applied stationarily at location C for another 1.8 seconds (see Figure 3.6). The total number of time steps used in this loadcase was 300 steps with a step size of 0.01 second. The reason for allowing the moving load to stop at location C was again due to the limiation of SAP-V program capacity. Nevertheless, this would not affect the analysis as the maximum peak stress was expected to occur at a time instant of about 0.85 seconds and was well within the initial period of 1.2 seconds.

The next two loadcases were carried out using Ram 14 bow force time history record with two different locations of load application. The location for load

case 8 was at location D between cant frames 25 to 29 and for load case 9 was at location C (Figure 3.5). The initial 2 seconds of the load was taken between 13.0 to 15.0 second of the time history shown in Figure 3.7. The analysis was carried out for 300 steps using a time step size of 0.016 second for a total of 4.8 seconds. Ram 14 was considered as a good ram without inducing a beaching motion. The maximum bow force peak value was 16.1 MN and the force was kept constant at 6 MN after initial 2 seconds.

Location A

Location D

Location C

Location B

Y

Z
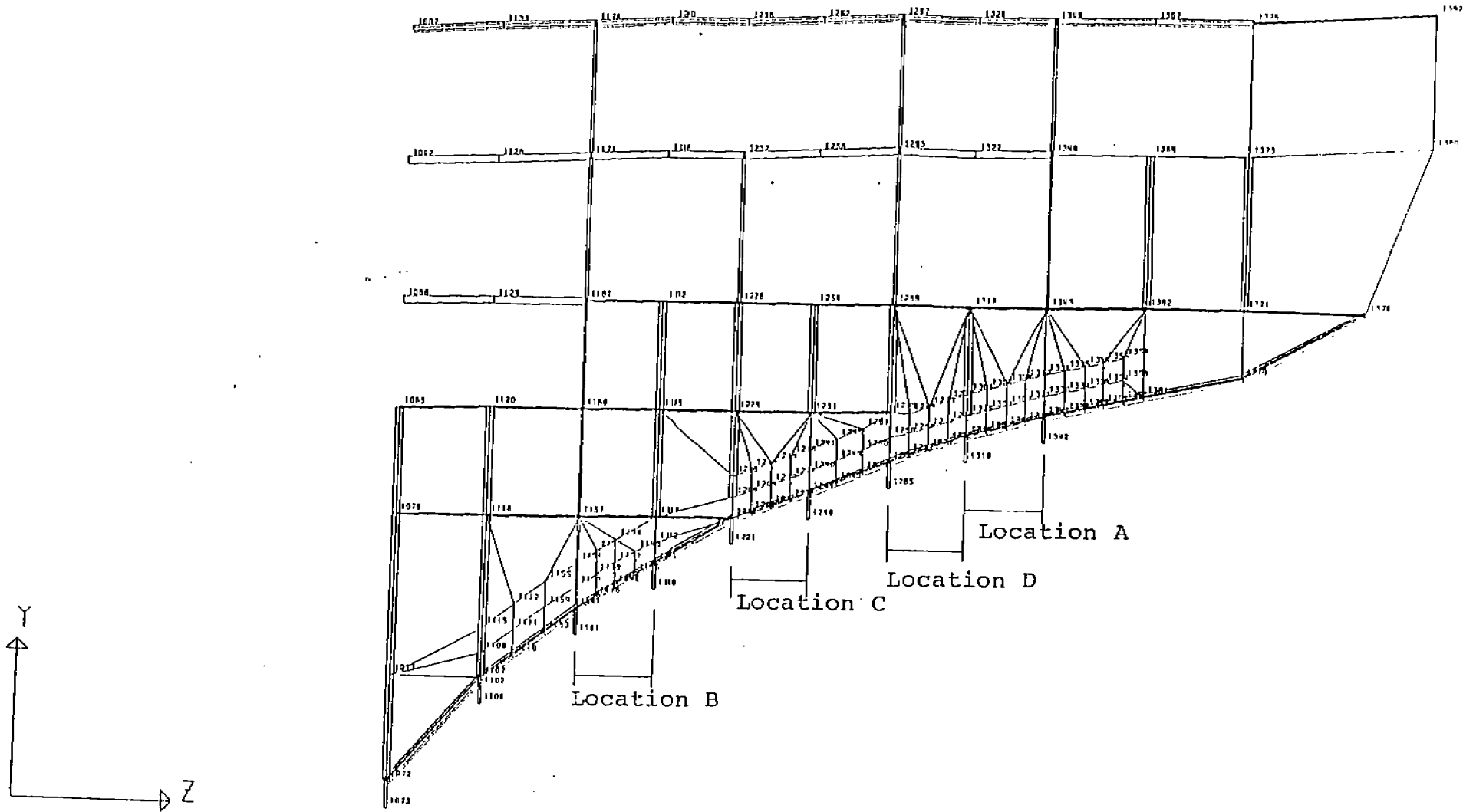
Figure 3.5   Forward end of Center line keel showing
             locations of applied bow force

1985 POLAR SEA IMPACT TESTS   (ARCTEC CANADA LTD.)
BOW FORCE TIME HISTORY   RAM 39

Load cases 5 and 6

Constant load at 14 MN for 2.4 seconds

Load case 7 moving load

Constant load at 7 MN for 1.8 seconds
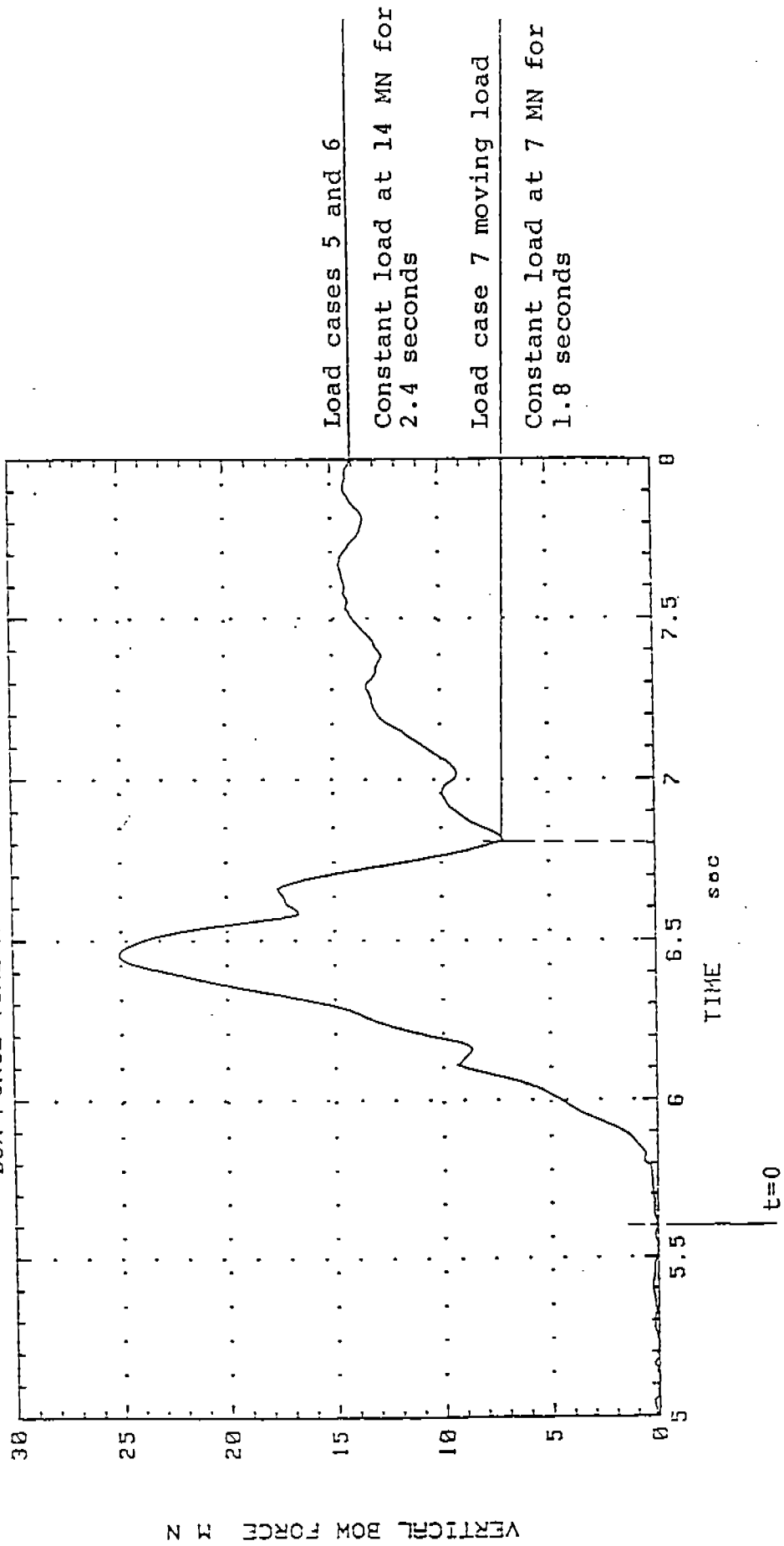
Figure 3.6   Ram 39 bow force history showing cut off points and durations for load cases 5, 6 and 7

-53-
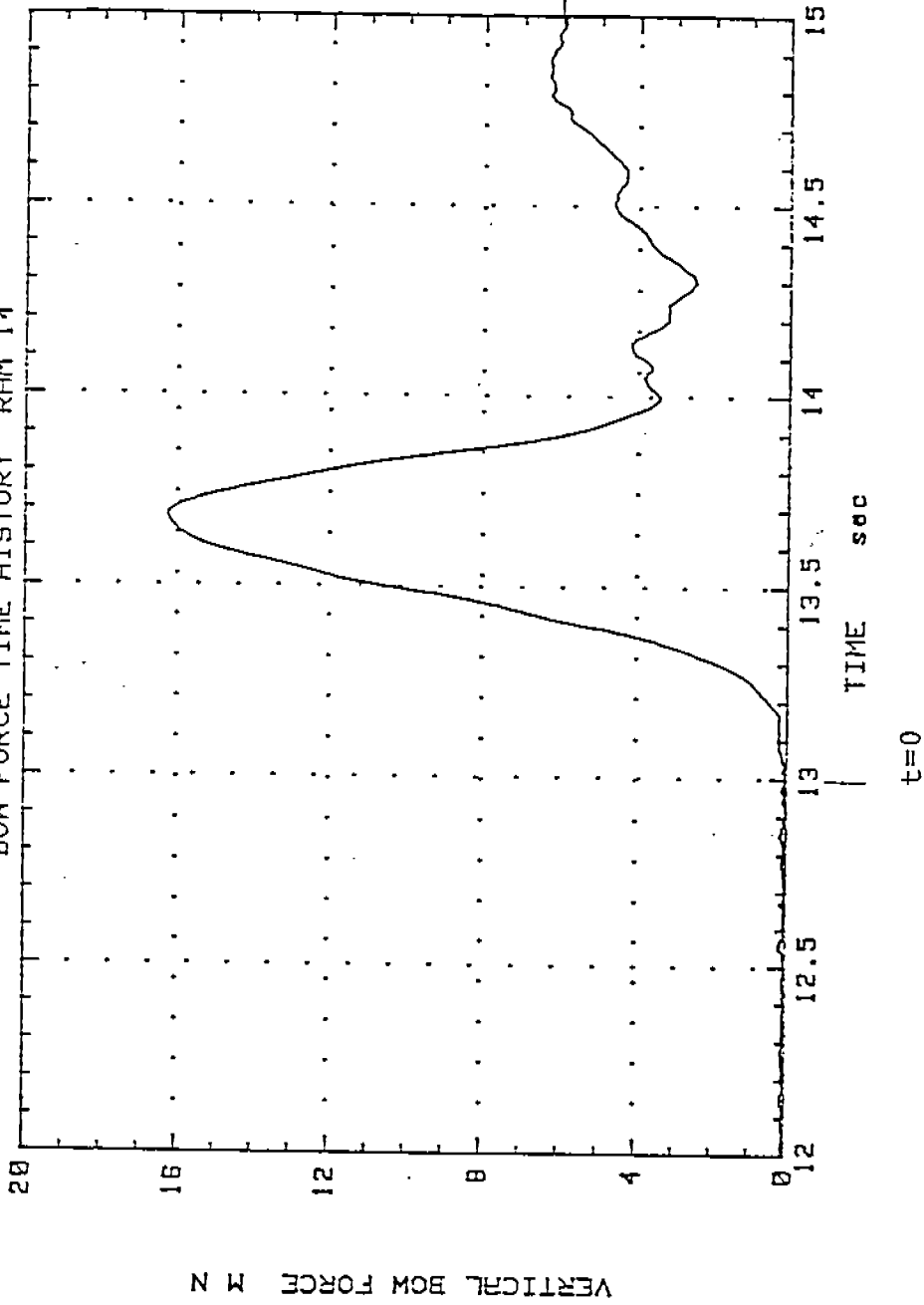
Figure 3.7   Ram 14 bow force history showing cut off points and
durations for load cases 8 and 9

3.5 Discussion of Results

The dynamic response in terms of stress time history was obtained for 31 elements along the side of the 01 deck over the entire ship length (see Figure 3.8). The stress time histories for 9 selected elements corresponding to the strain gage locations are presented in Figures 3.9 to 3.17 for all the various load cases considered. To better evaluate the response of the vessel, the displacement time histories for 7 selected nodal points along the center line of 01 deck are also presented in Figures 3.18 and 3.19 for two load cases.

As can be seen from the stress time history response curves, the peak stress and the time instant at which the peak stress occurs are of primary concern. Tables 3.3 to 3.11 show the values of the peak stresses and the corresponding time instants for all the selected elements on the 01 deck. The strain gage locations related to the element number of the mathematical model are also listed in the tables. A summary of results for the 9 load cases considered is given in Table 3.12.

In the polar sea ice impact tests, the direct measurements were made in terms of the strain time hisotry. These strain time history data were then converted to stress time history for all the strain gage locations to obtain the vertical bow force time history of the ice load. The present analysis is a reverse process. Using the interpreted ice loads, a dynamic transient analysis was performed on the finite element model to obtain the response in terms of stress time history. A comparison is made of the calculated and measured results.

Before using the actual ice load time histories provided by ARCTEC, four load cases using predefined shape of time function for unit ice loads were used in the analysis. The maximum vertical bow force of these unit loads applied to strcuture was taken as 2 MN.

Figure 3.9 shows the results of stress time history corresponding to load case 1, which has a triangular distribution of time function. The maximum peak stress was found to occur at element 914 (B-01-39-P&S) and has a compressive stress value of 610 psi at the time instant of 0.68 second. The stress response curves follow closely to the shape of the applied load time history and the phenomenon was more distinct at the locations such as elements 919 (B-01-C35-P&S) and 921 (B-01-C27-P&S) in way of the frames where the bow force was applied. In addition, hull girder vibration effect was observed near the midship region. This vibration effect can be seen from the stress time history of element 906 (B-01-128-P&S).

The effect of dynamic response as described above is more obvious in load cases 2 and 3 in which the forcing function is in the form of trigonometric functions. Referring to the stress time history of element 906 in Figure 3.10 for load case 2 and Figure 3.11 for load case 3, it can be seen that the dynamic behaviour is similar to the bending stress time history for gage B01-128-S of Ram 9 given in the ARCTEC Report. The frequency of vibration as noted in the stress time histories is 3.06 Hz, which corresponds to the frequency of the two-node bending mode of the hull girder. The two-node bending vibration is seen to be more pronounced amidship and becomes less and less distinct towards
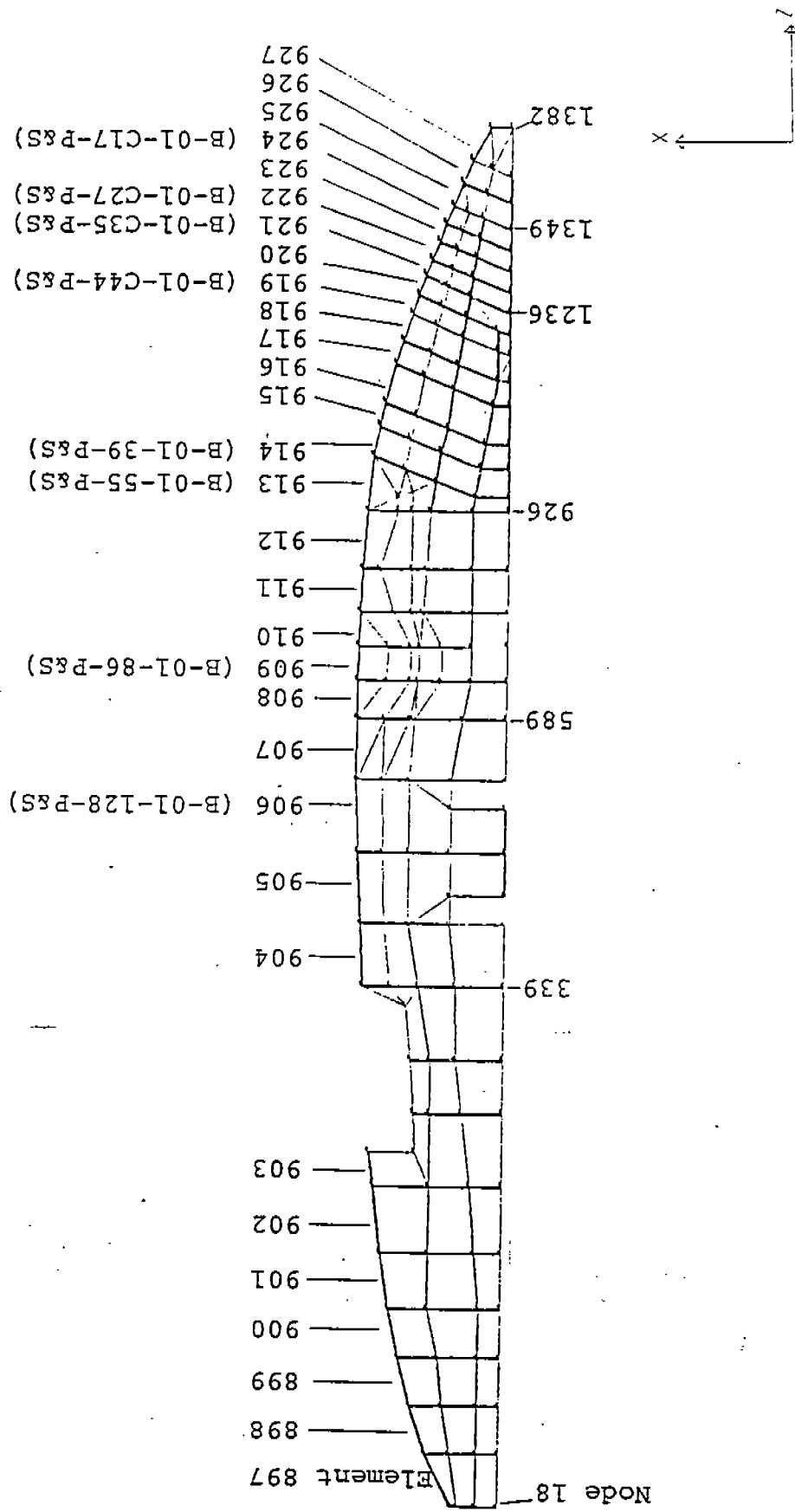
Figure 3.8 Selected elements and nodal points on 01 deck
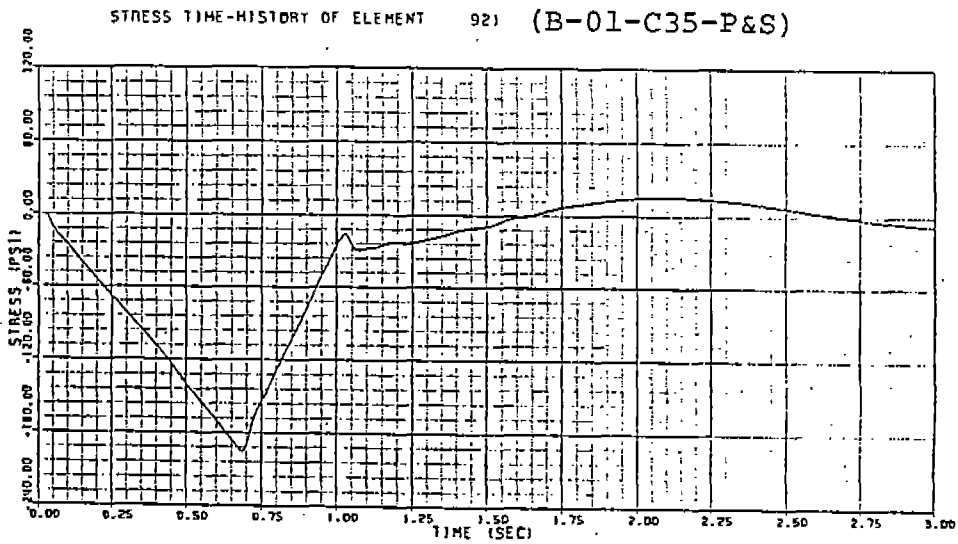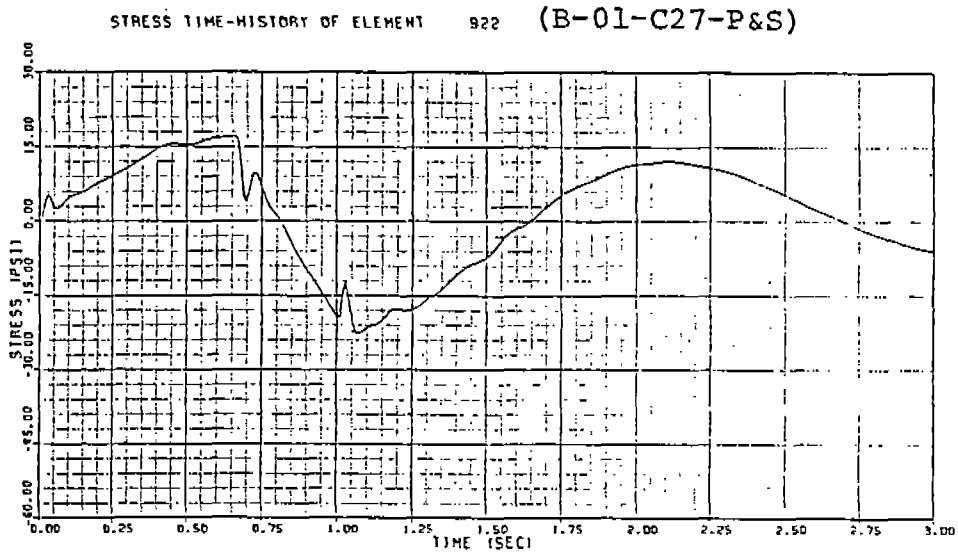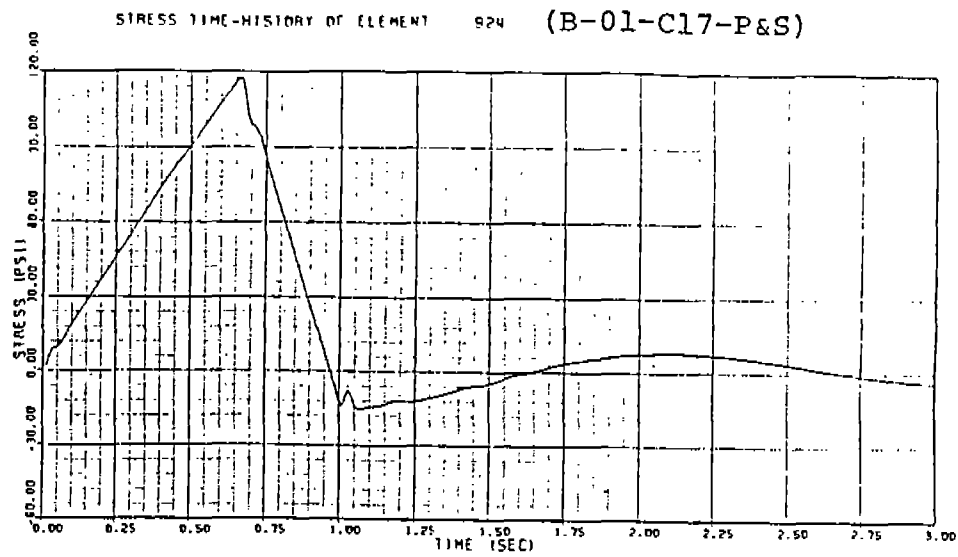
927
926
925
924   (B-01-C17-P&S)
923
922   (B-01-C27-P&S)
921   (B-01-C35-P&S)
920
919   (B-01-C44-P&S)
918
917
916
915
914   (B-01-39-P&S)
913   (B-01-55-P&S)
912
911
910
909   (B-01-98-P&S)
908
907
906   (B-01-128-P&S)
905
904
903
902
901
900
899
898
Element 897

1382
1349
1236
926
589
339

Node 18

STRESS TIME-HISTORY OF ELEMENT   924   (B-01-C17-P&S)

STRESS TIME-HISTORY OF ELEMENT   922   (B-01-C27-P&S)

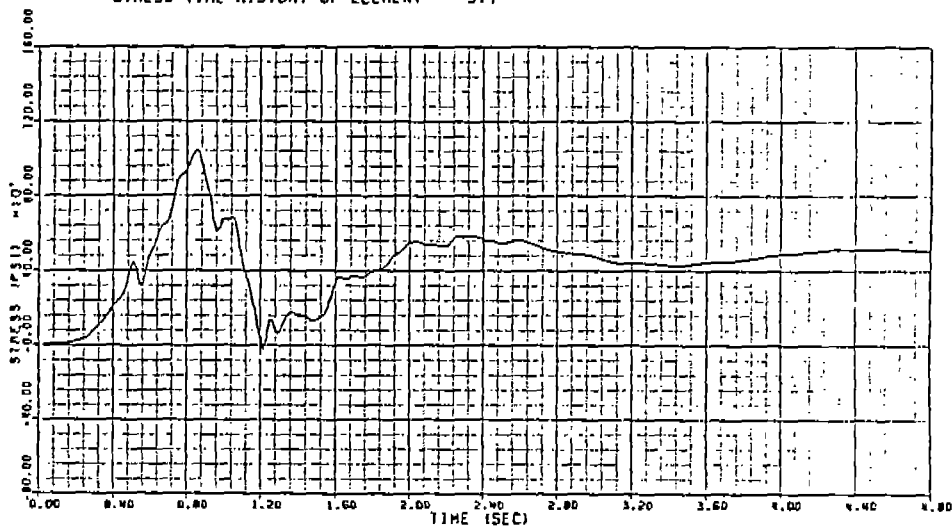STRESS TIME-HISTORY OF ELEMENT   921   (B-01-C35-P&S)

Figure 3.9   Stress Time History for Load case 1

-57-

STRESS TIME-HISTORY OF ELEMENT   919   (B-01-C44-P&S)
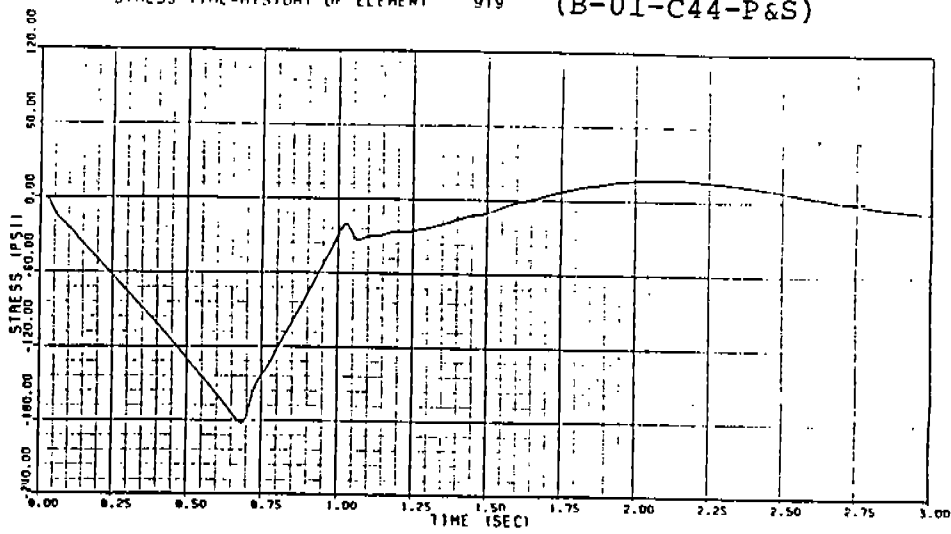
STRESS TIME-HISTORY OF ELEMENT   917
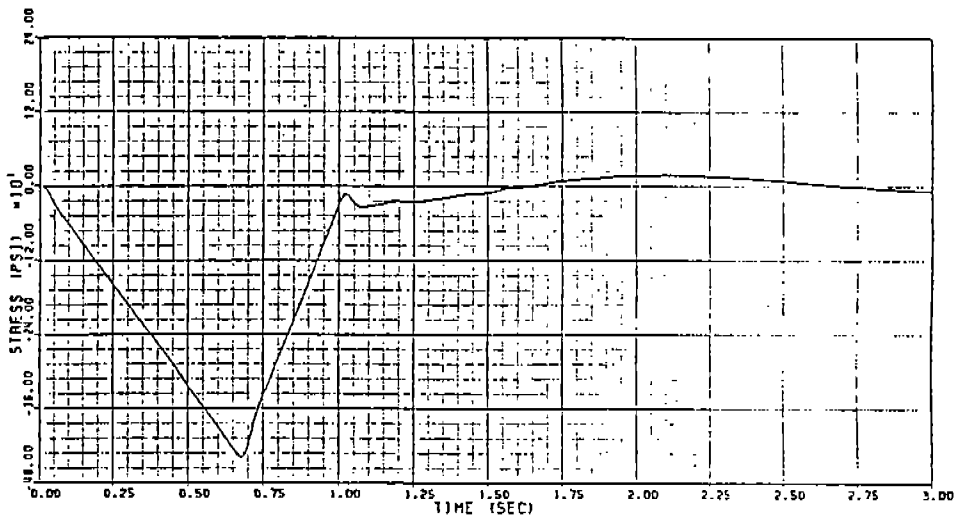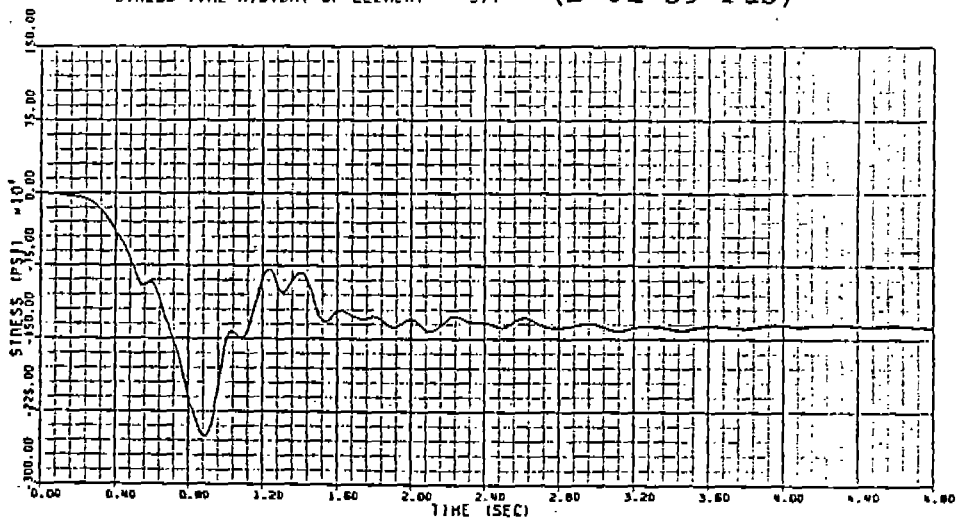

STRESS TIME-HISTORY OF ELEMENT   914   (B-01-39-P&S)
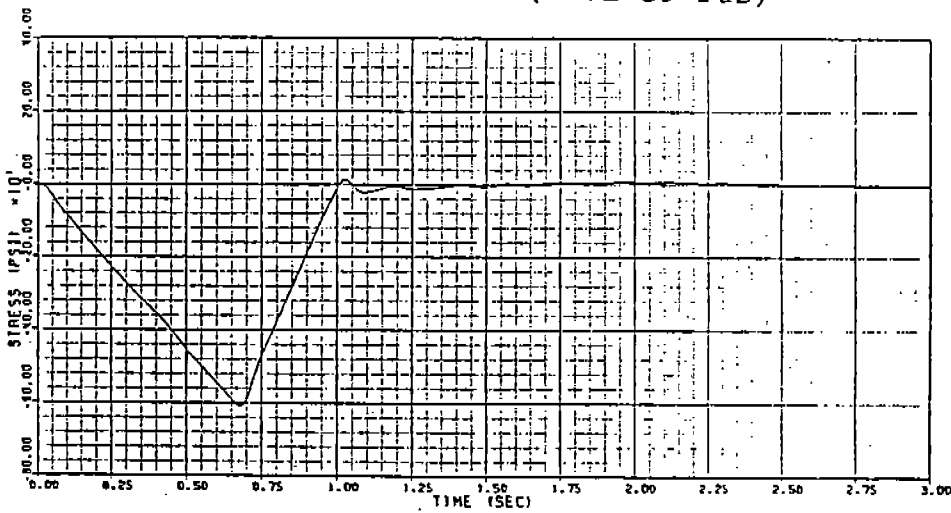
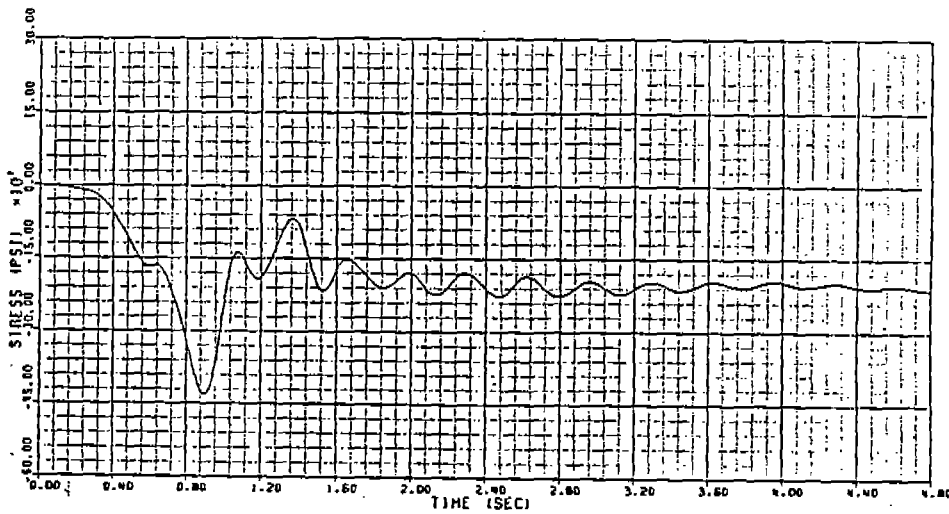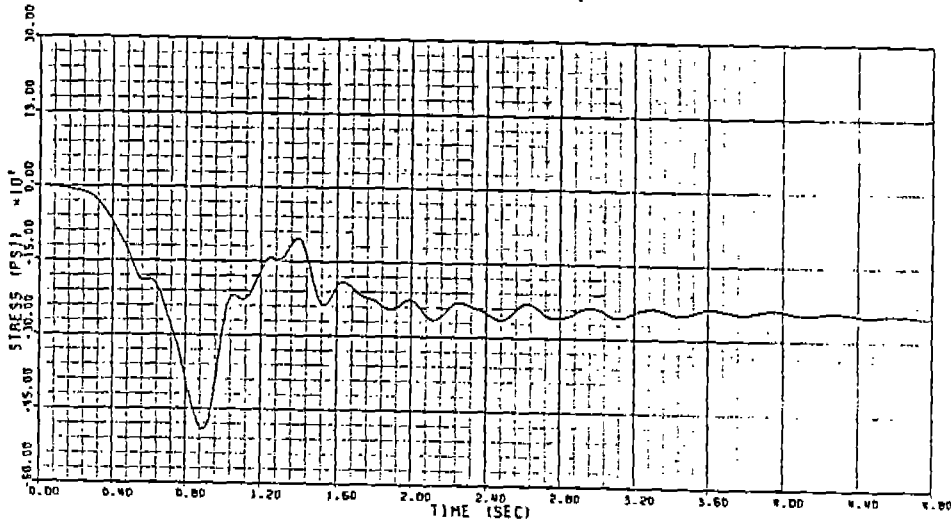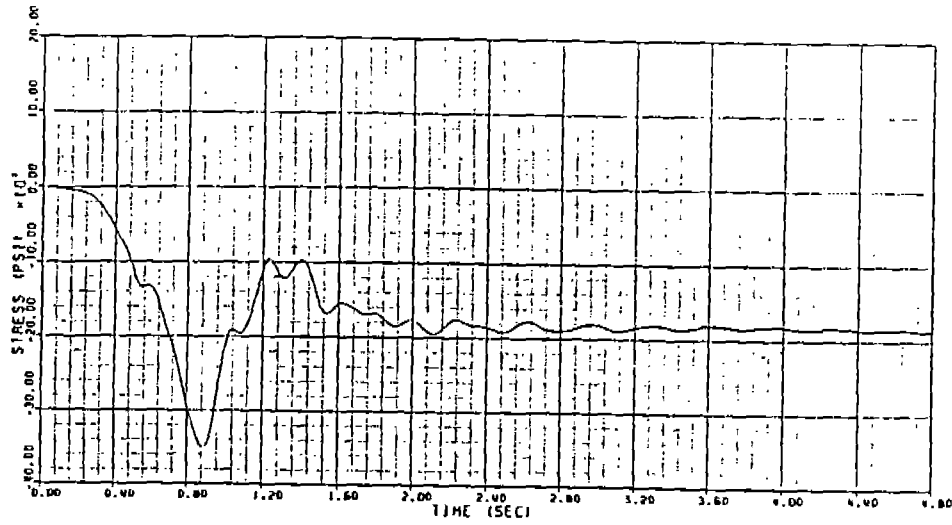

Figure 3.9   Stress Time History for Load case 1 (cont'd)

STRESS TIME-HISTORY OF ELEMENT   913   (B-01-55-P&S)
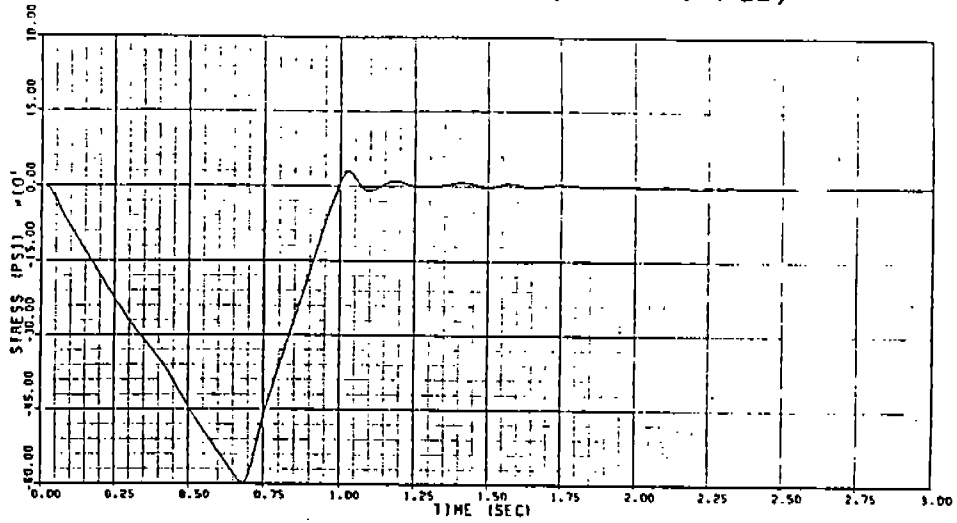
STRESS TIME-HISTORY OF ELEMENT   909   (B-01-86-P&S)
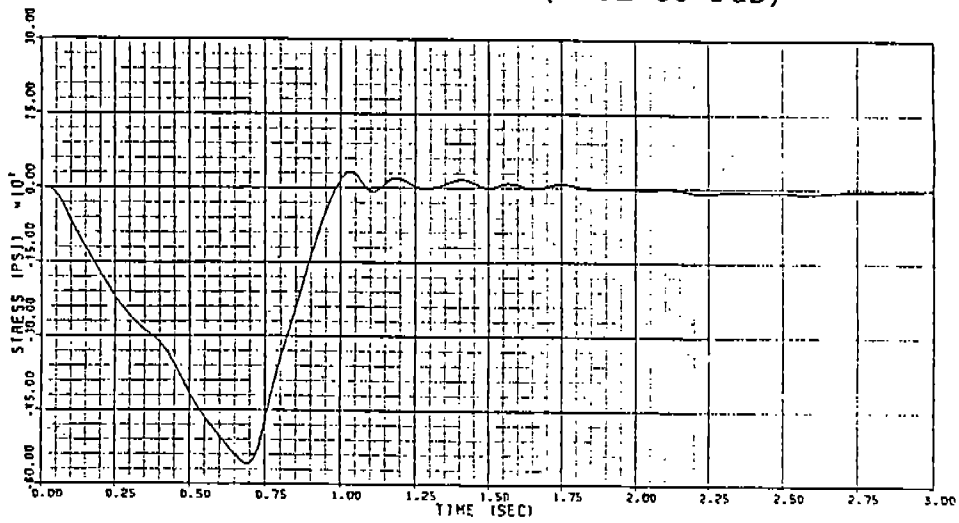
STRESS TIME-HISTORY OF ELEMENT   906   (B-01-128-P&S)
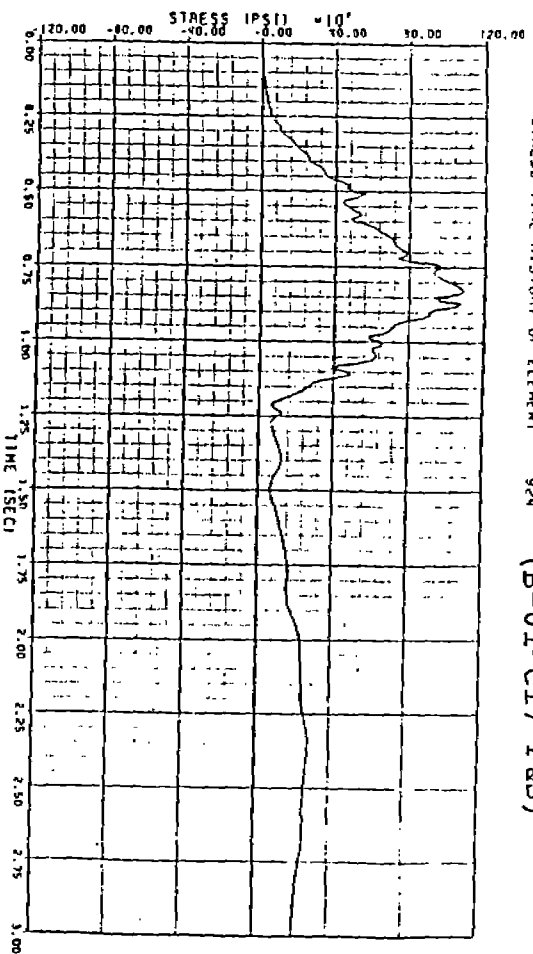
Figure 3.9   Stress Time History for Load case 1 (cont'd)

-59-

STRESS TIME-HISTORY OF ELEMENT   924   (B-01-C17-P&S)
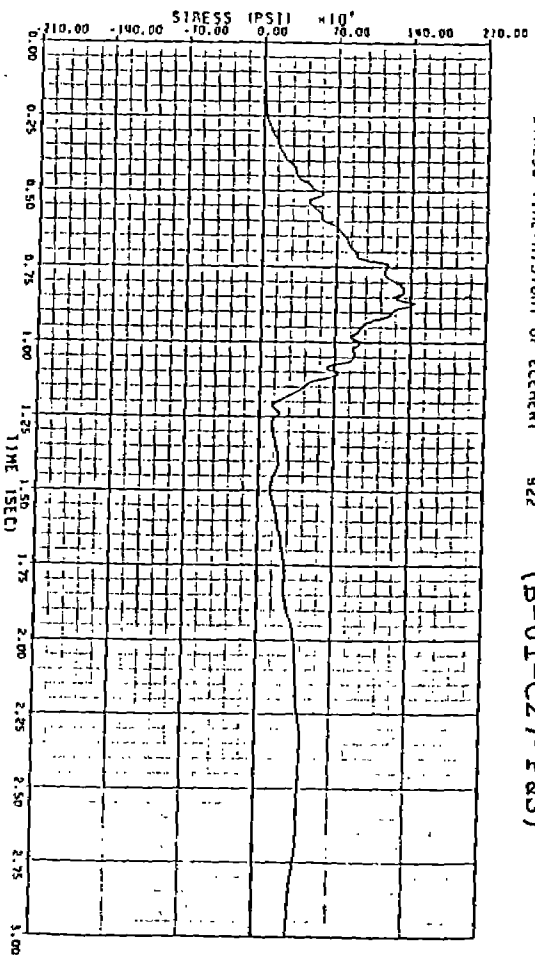
STRESS TIME-HISTORY OF ELEMENT   922   (B-01-C27-P&S)
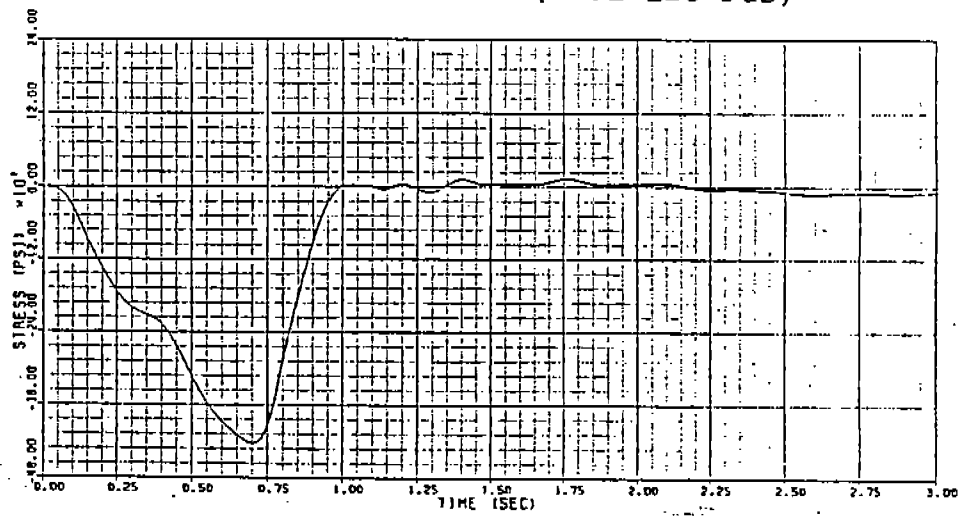
STRESS TIME-HISTORY OF ELEMENT   521   (B-01-C35-P&S)
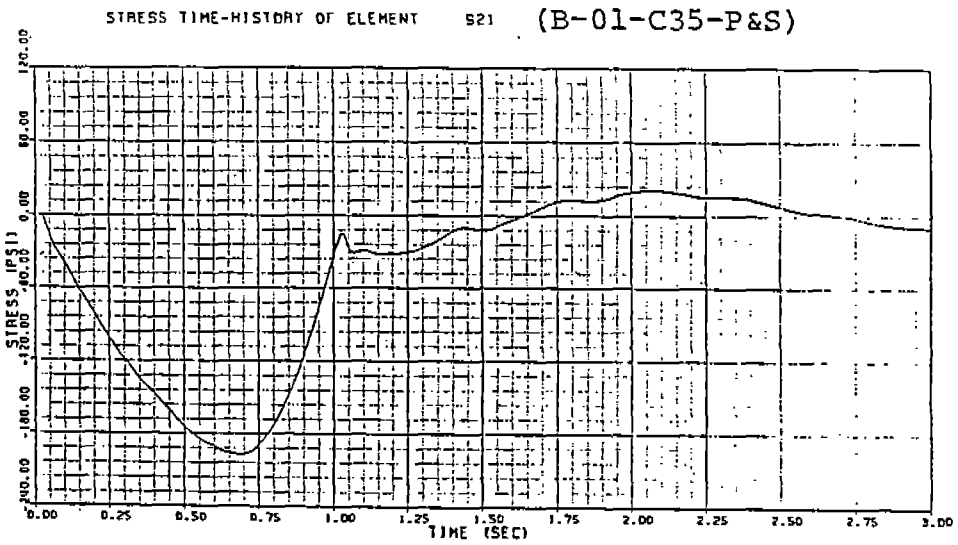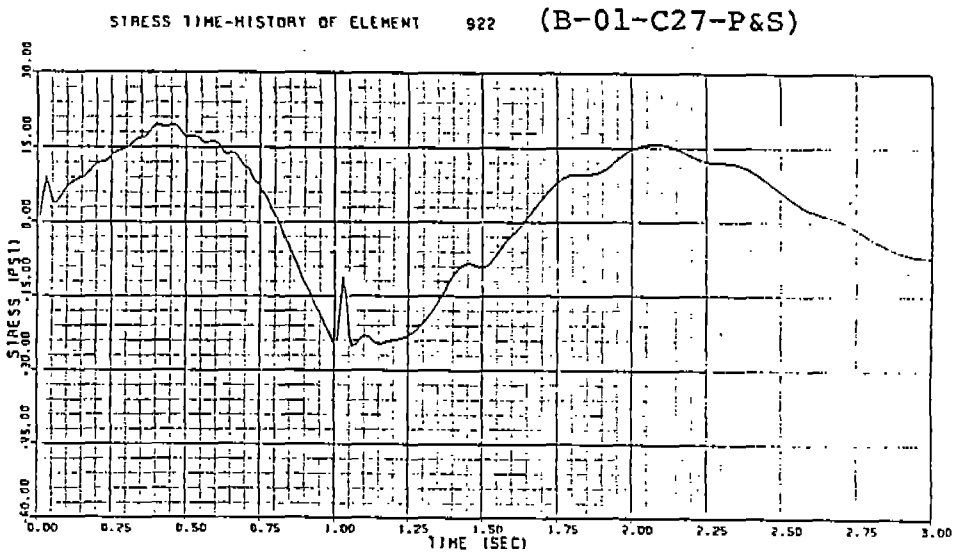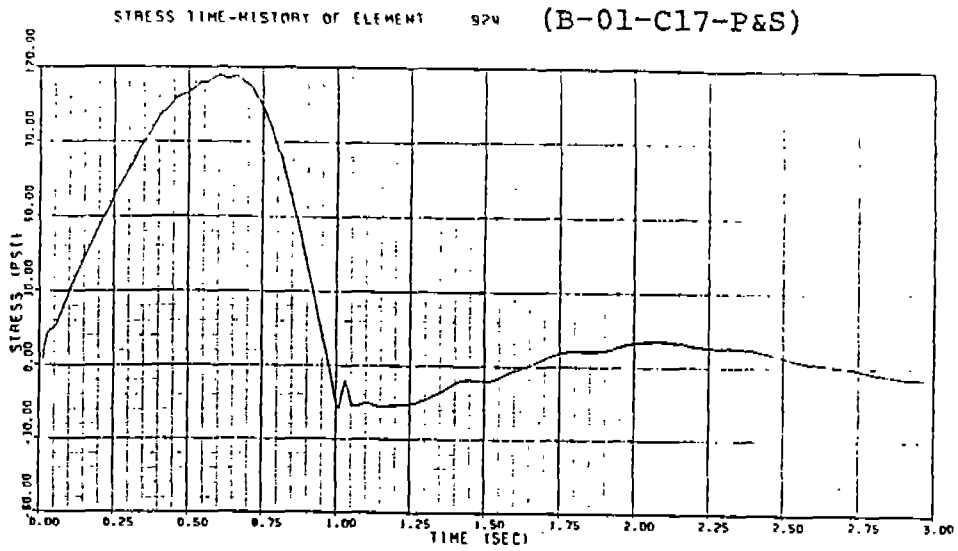
Figure 3.10 Stress Time History for Load case 2

STRESS TIME-HISTORY OF ELEMENT   919   (B-01-C44-P&S)
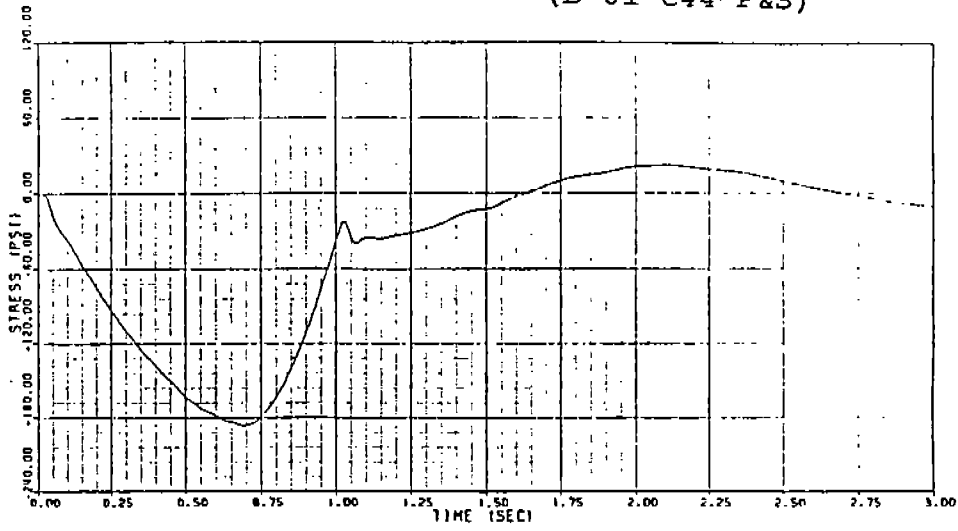
STRESS TIME-HISTORY OF ELEMENT   917
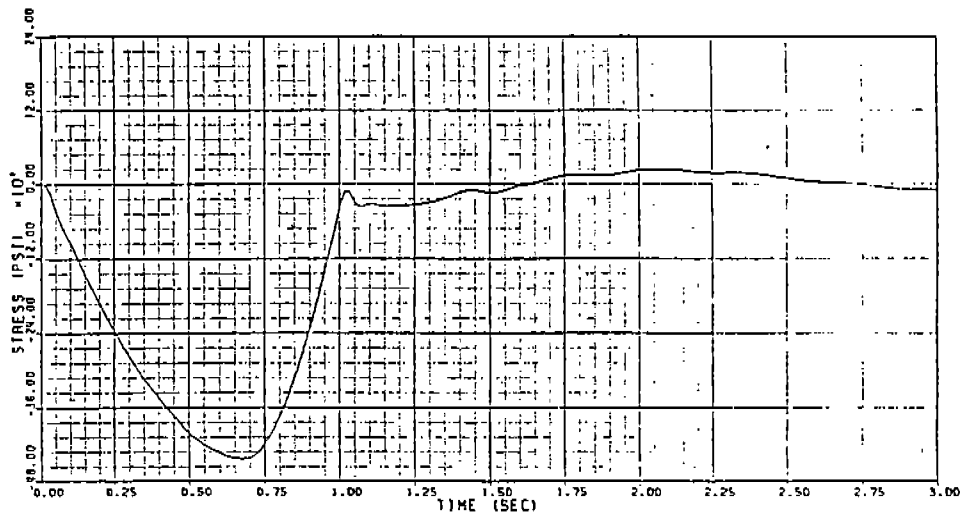
STRESS TIME-HISTORY OF ELEMENT   914   (B-01-39-P&S)

Figure 3.10 Stress Time History for Load case 2 (cont'd)

STRESS TIME-HISTORY OF ELEMENT 913   (B-01-55-P&S)

STRESS TIME-HISTORY OF ELEMENT 909   (B-01-86-P&S)
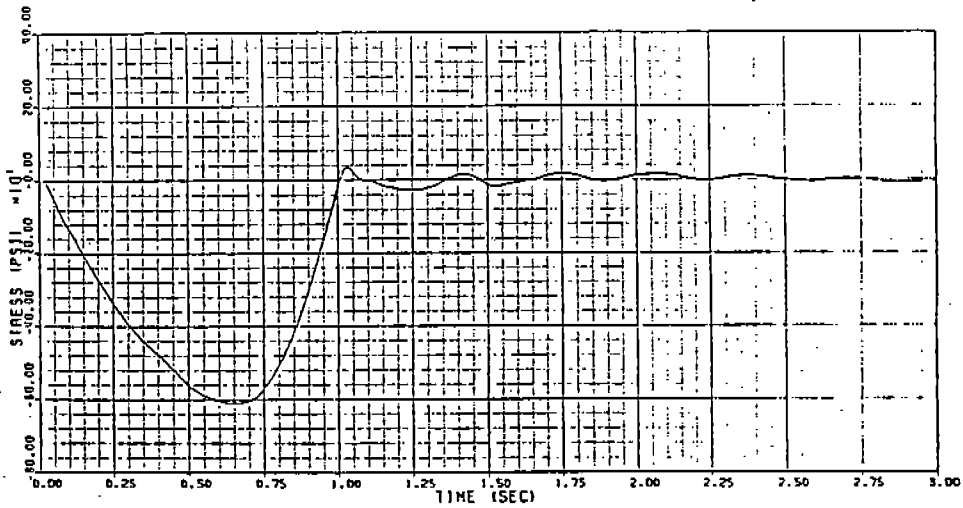
STRESS TIME-HISTORY OF ELEMENT 906   (B-01-128-P&S)

Figure 3.10 Stress Time History for Load case 2 (cont'd)
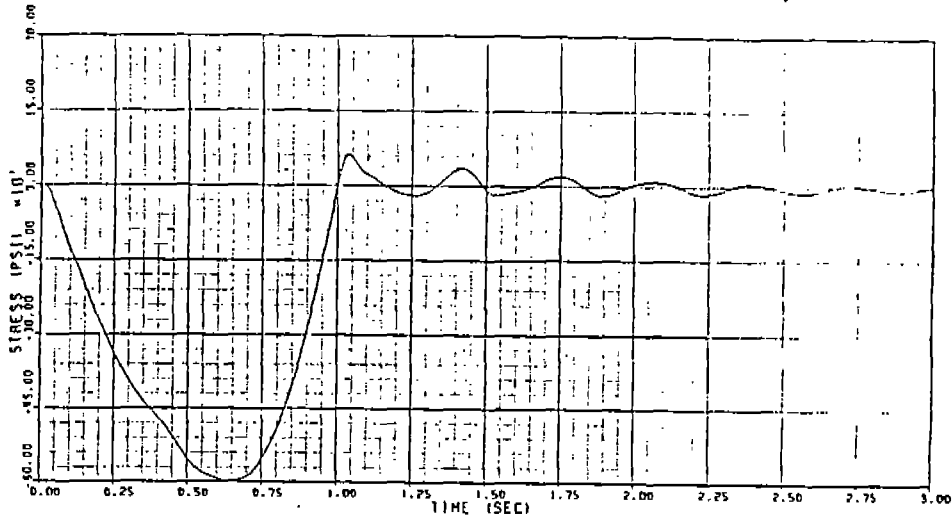
STRESS TIME-HISTORY OF ELEMENT   924   (B-01-C17-P&S)
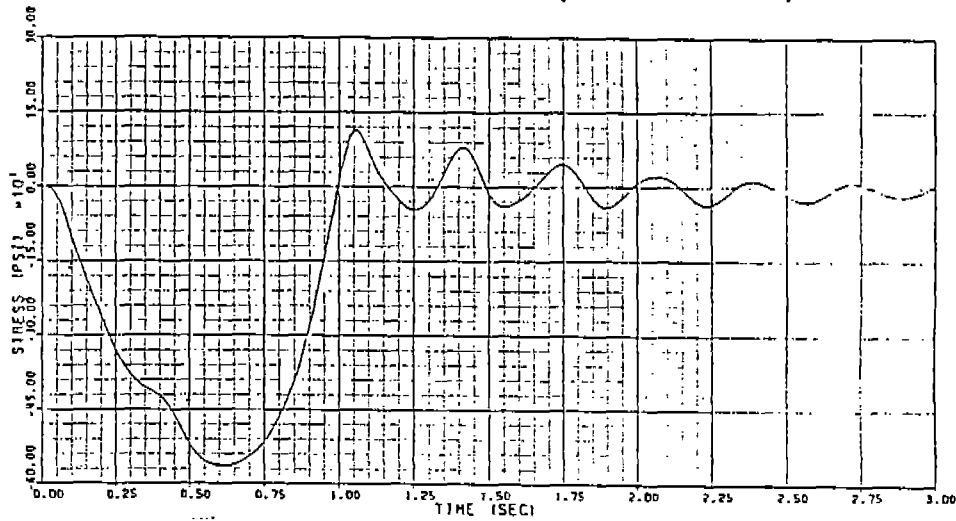
STRESS TIME-HISTORY OF ELEMENT   922   (B-01-C27-P&S)
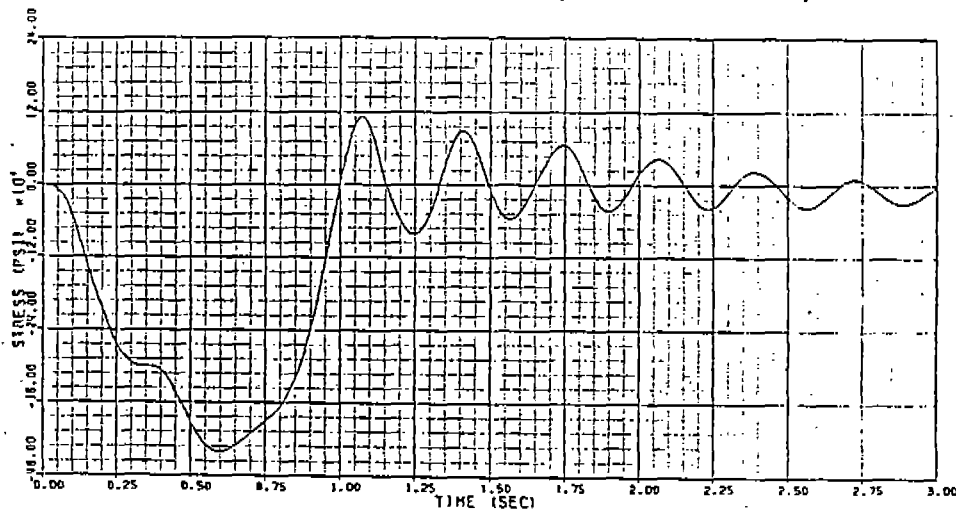
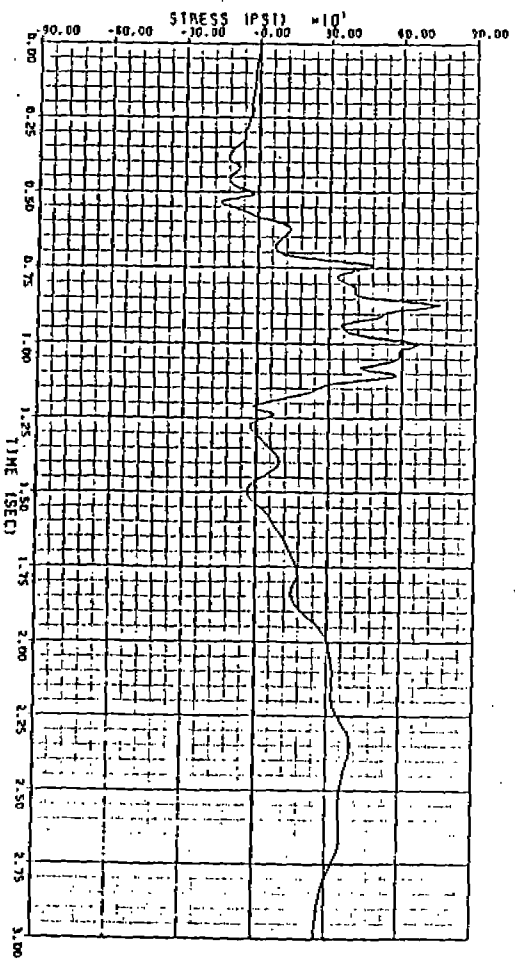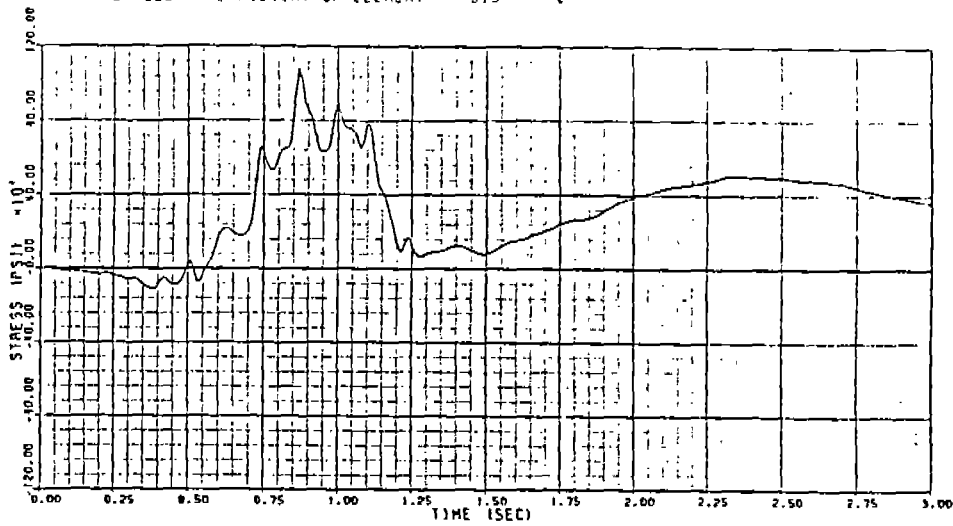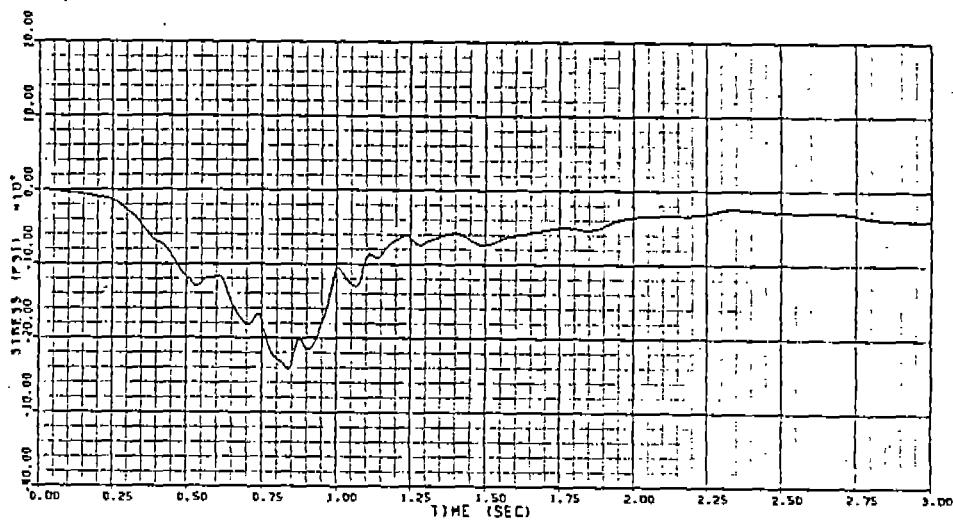STRESS TIME-HISTORY OF ELEMENT   921   (B-01-C35-P&S)
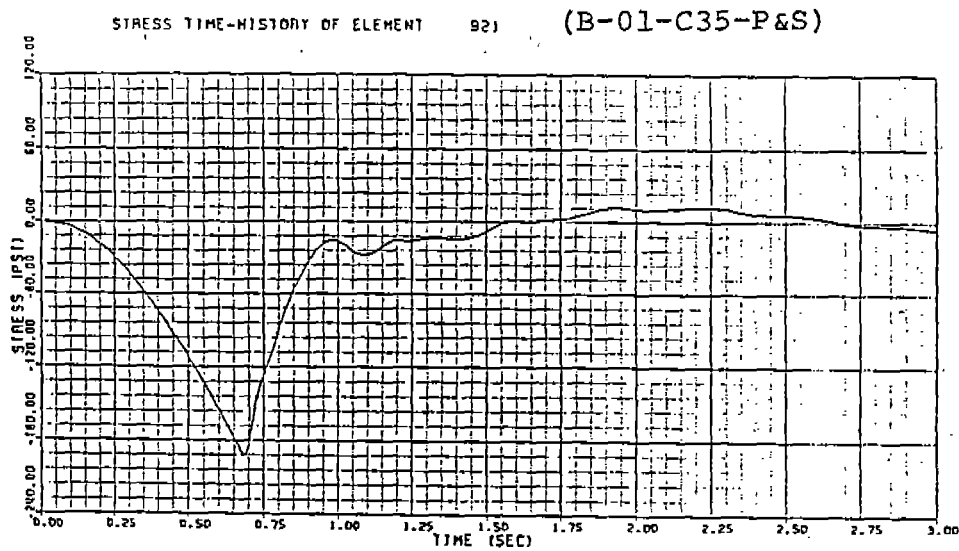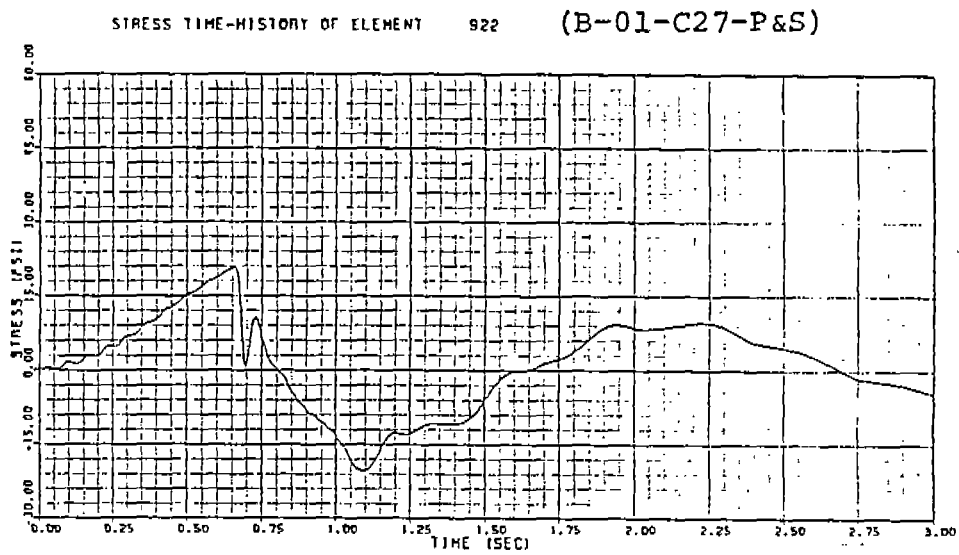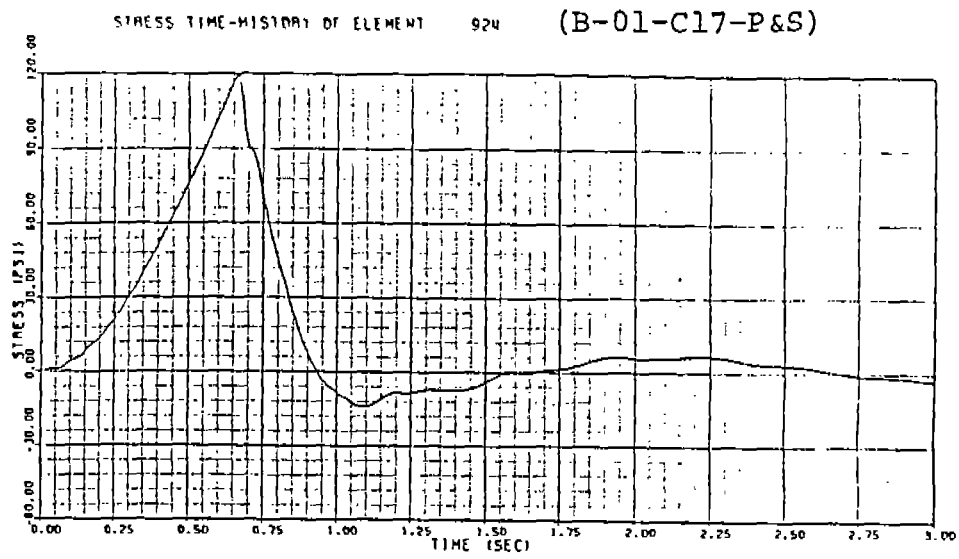
Figure 3.11 Stress Time History for Load case 3

STRESS TIME-HISTORY OF ELEMENT 919 (B-01-C44-P&S)
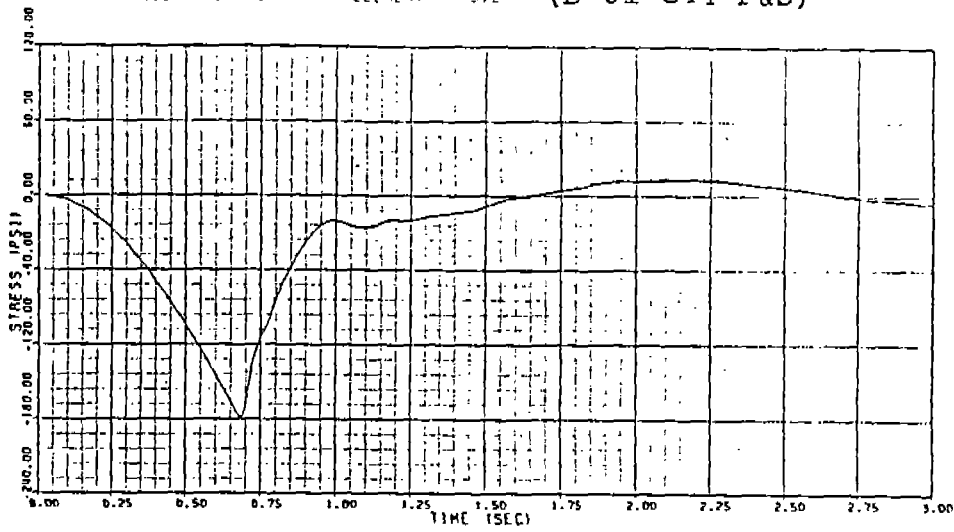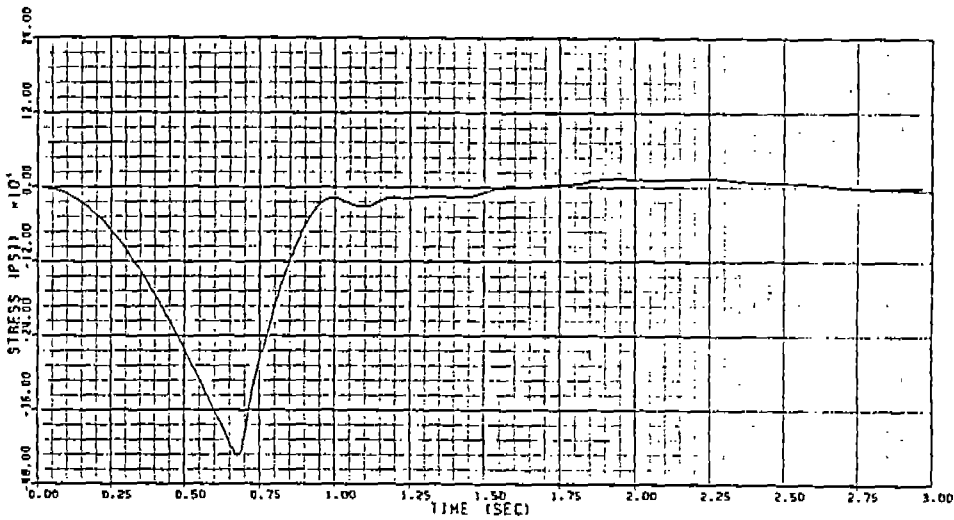
STRESS TIME-HISTORY OF ELEMENT 917

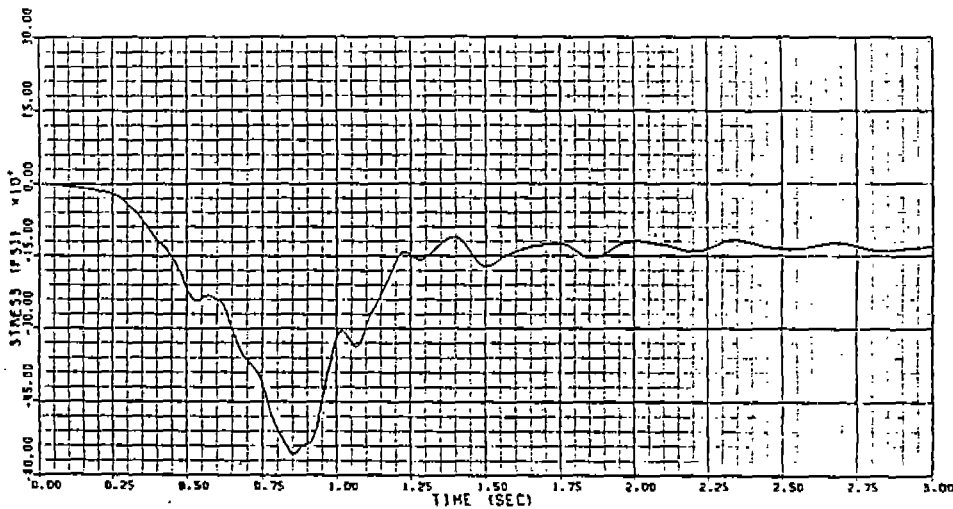STRESS TIME-HISTORY OF ELEMENT 914 (B-01-39-P&S)

Figure 3.11 Stress Time History for Load case 3 (cont'd)
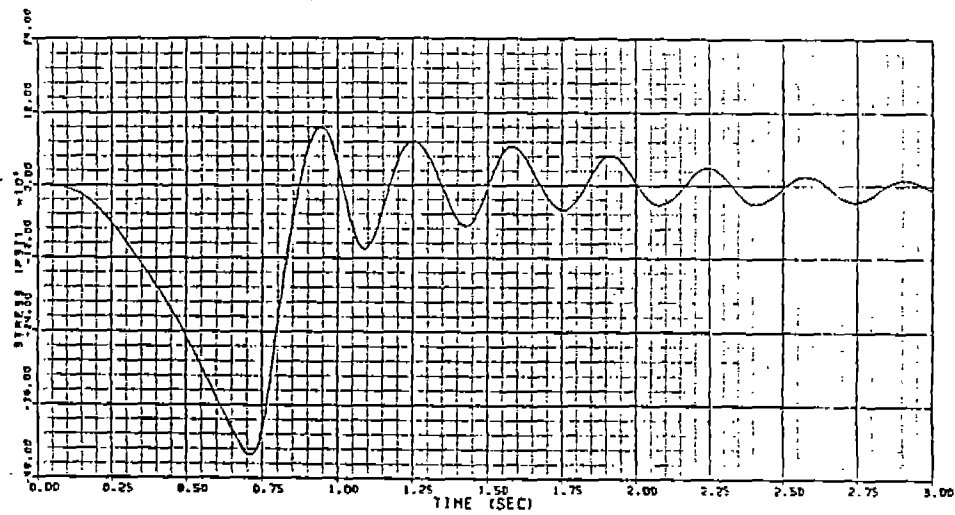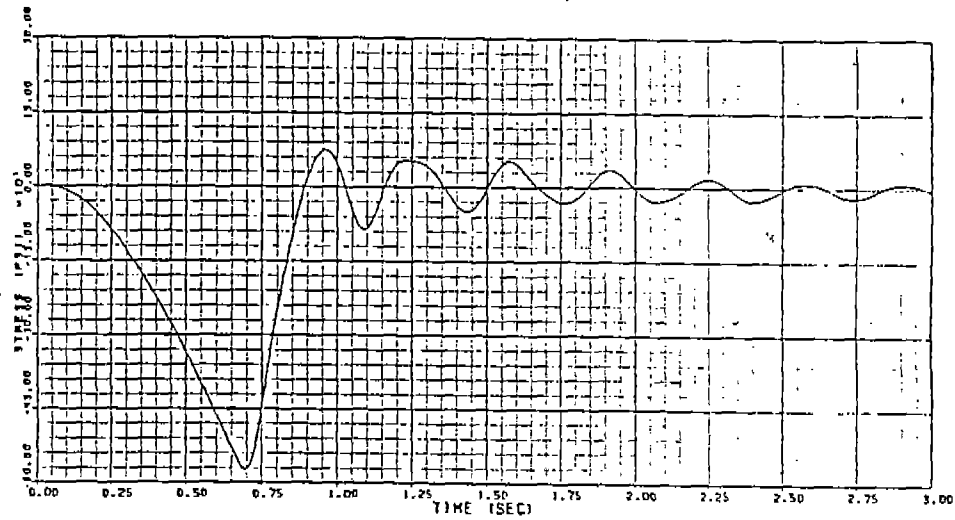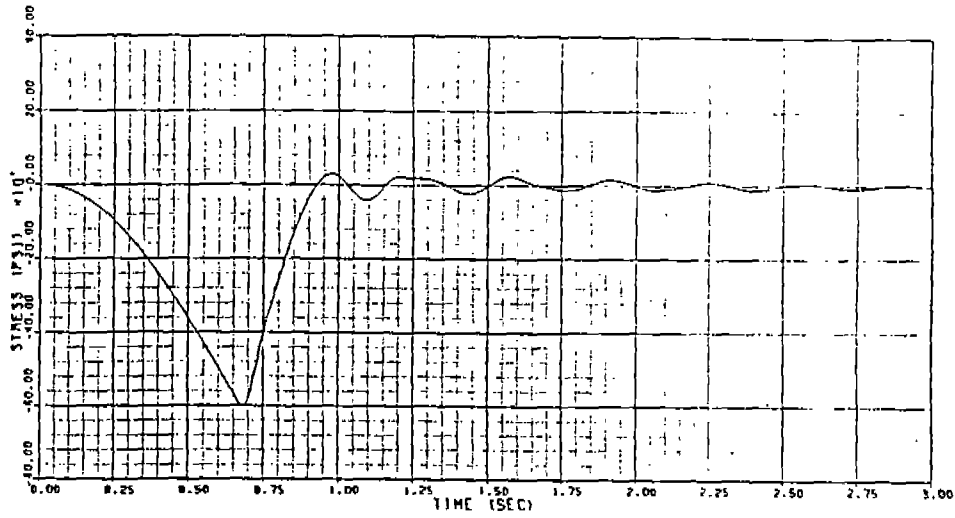
STRESS TIME-HISTORY OF ELEMENT 973 (B-01-55-P&S)

STRESS TIME-HISTORY OF ELEMENT 909 (B-01-86-P&S)

STRESS TIME-HISTORY OF ELEMENT 906 (B-01-128-P&S)

Figure 3.11 Stress Time History for Load case 3 (cont'd)

-65-

STRESS TIME-HISTORY OF ELEMENT   924   (B-01-C17-P&S)

STRESS TIME-HISTORY OF ELEMENT   922   (B-01-C27-P&S)

STRESS TIME-HISTORY OF ELEMENT   921   (B-01-C35-P&S)
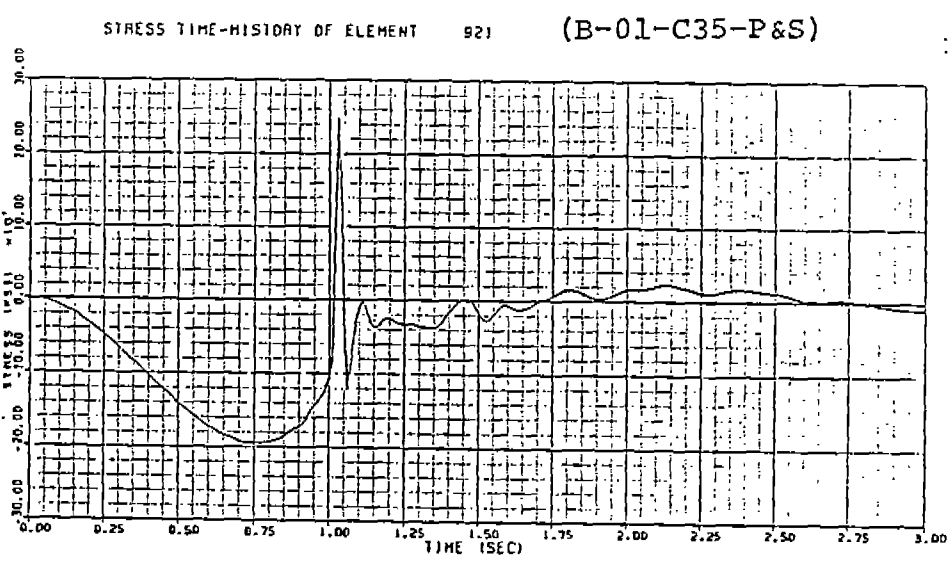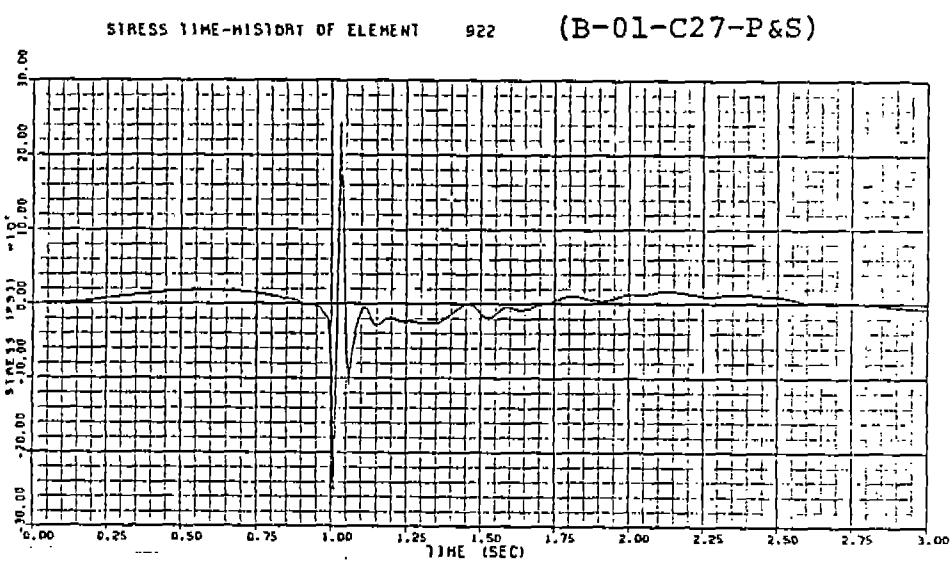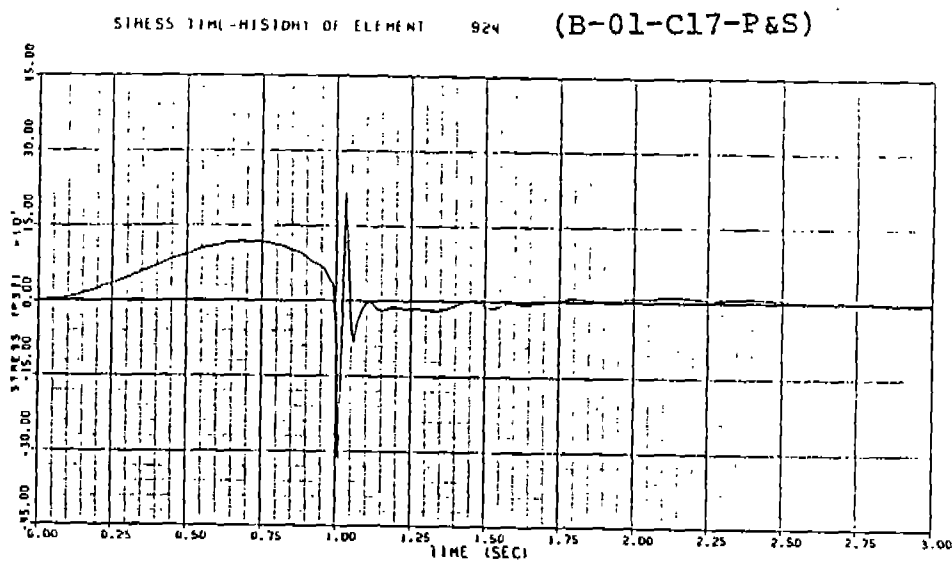
Figure 3.12 Stress Time History for Load case 4

STRESS TIME-HISTORY OF ELEMENT   919   (B-01-C44-P&S)
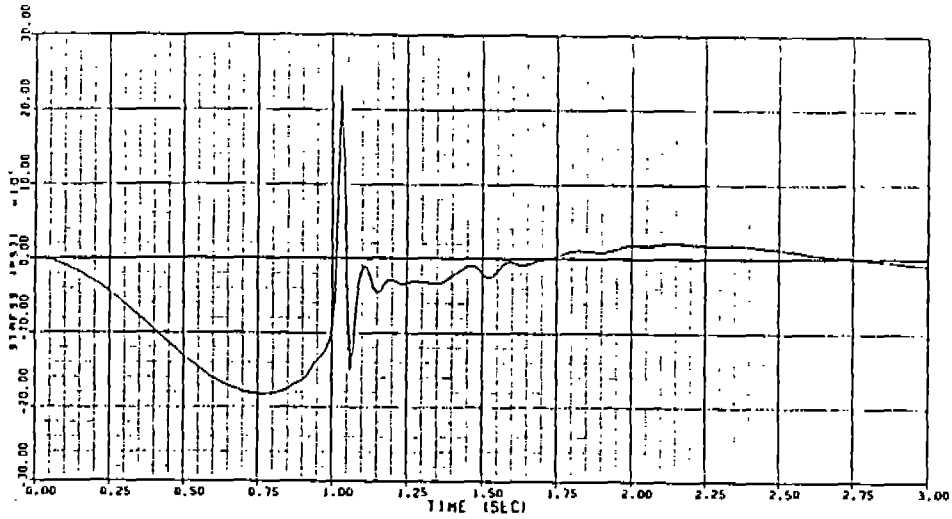
STRESS TIME-HISTORY OF ELEMENT   917

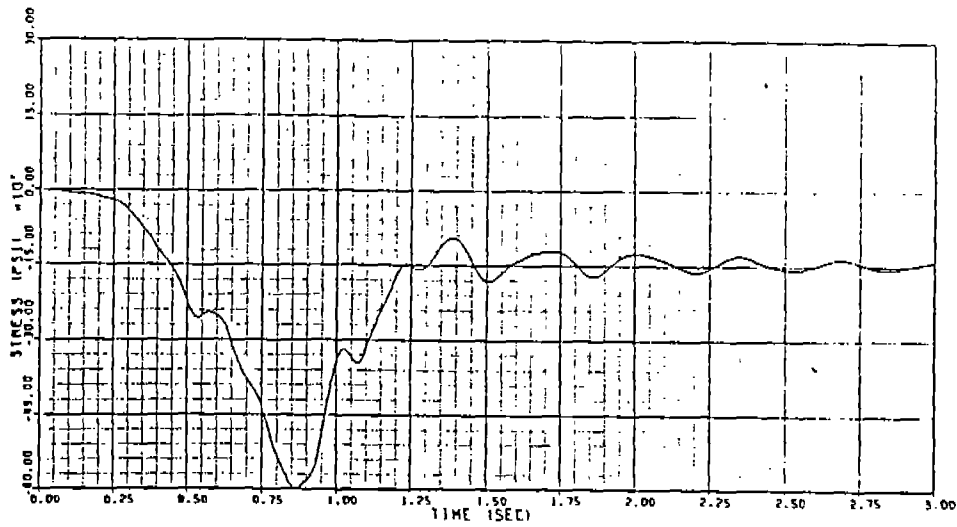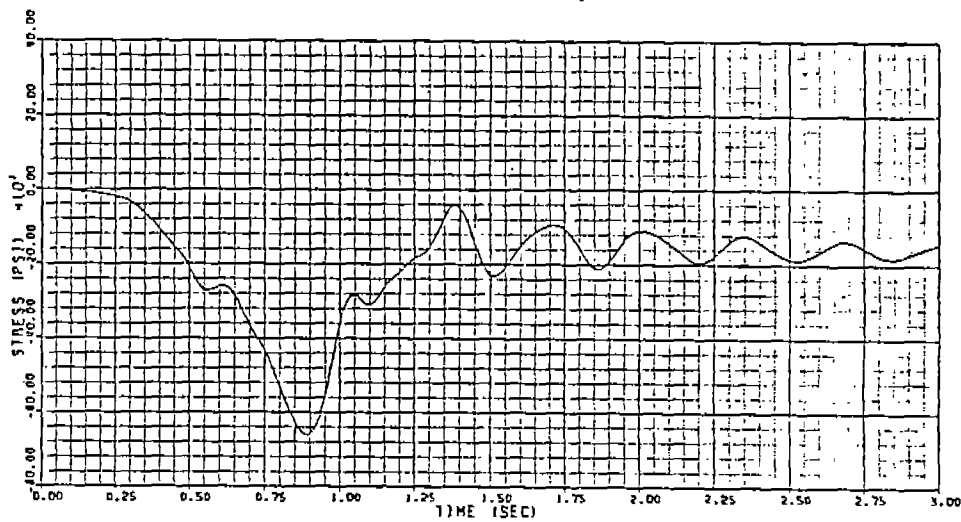STRESS TIME-HISTORY OF ELEMENT   914   (B-01-39-P&S)

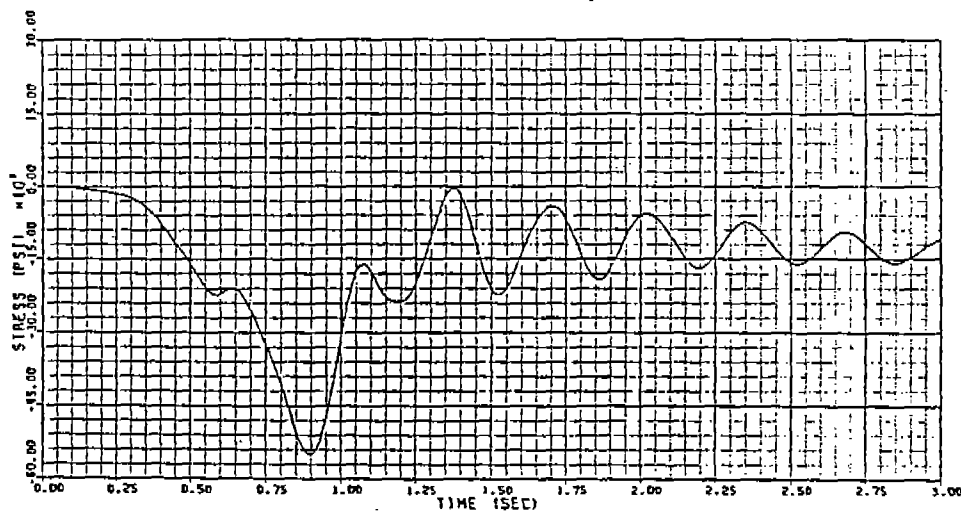Figure 3.12 Stress Time History for Load case 4 (cont'd)
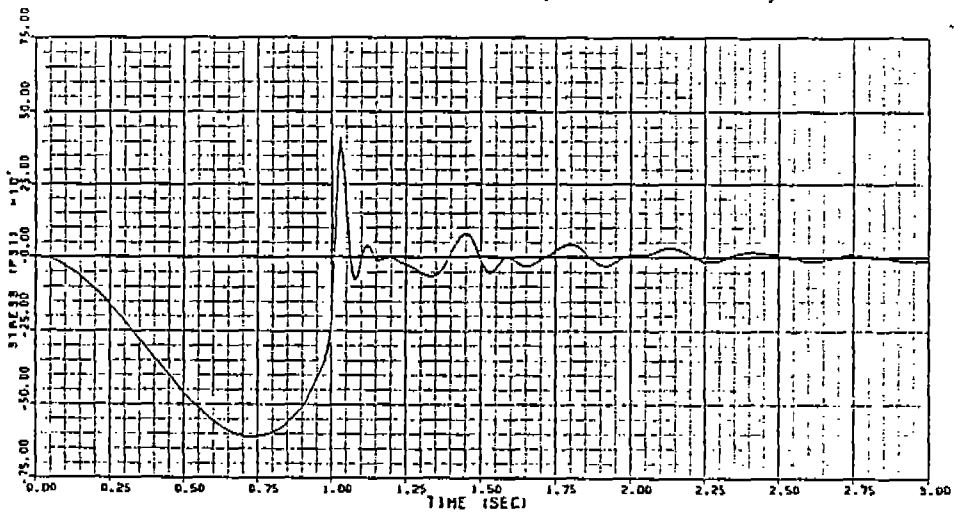
Figure 3.12 Stress Time History for Load case 4 (cont'd)

STRESS TIME-HISTORY OF ELEMENT   924   (B-01-C17-P&S)
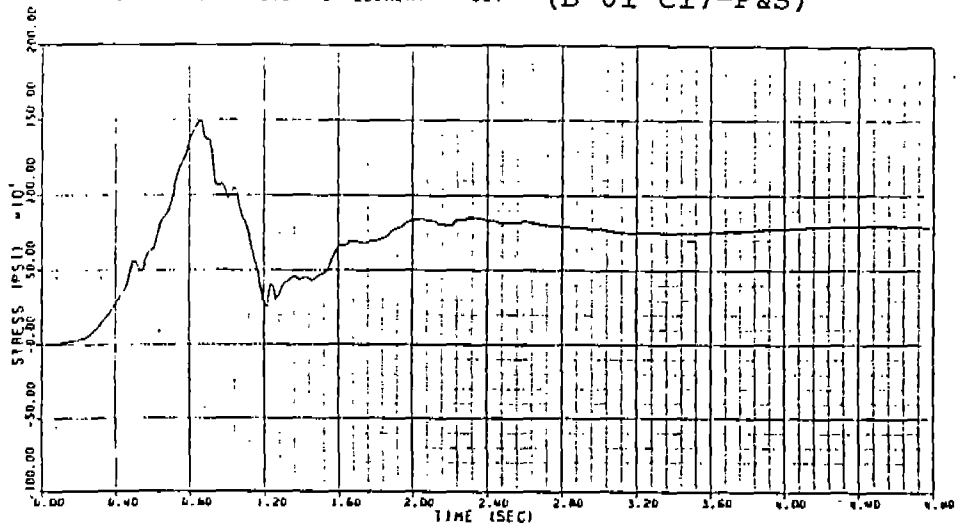
STRESS TIME-HISTORY OF ELEMENT   922   (B-01-C27-P&S)
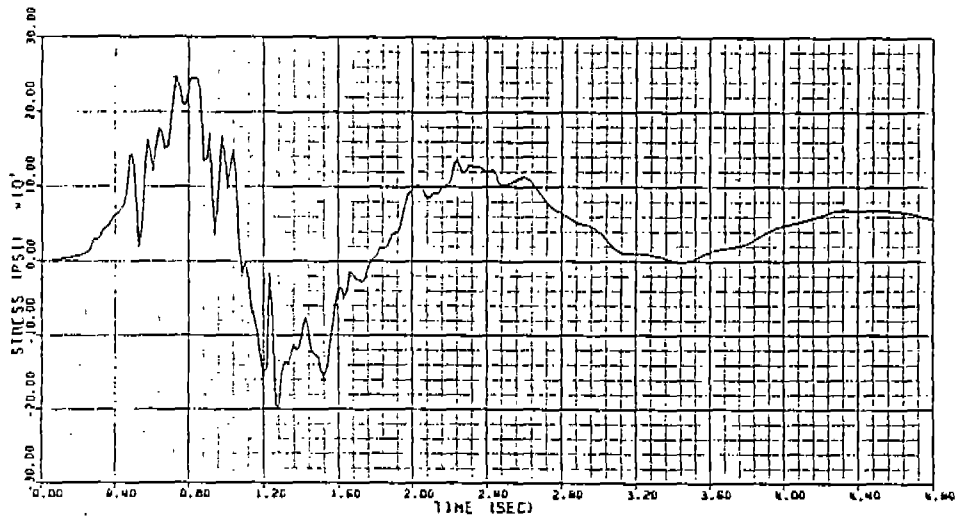
STRESS TIME-HISTORY OF ELEMENT   921   (B-01-C35-P&S)

Figure 3.13 Stress Time History for Load case 5

-69-
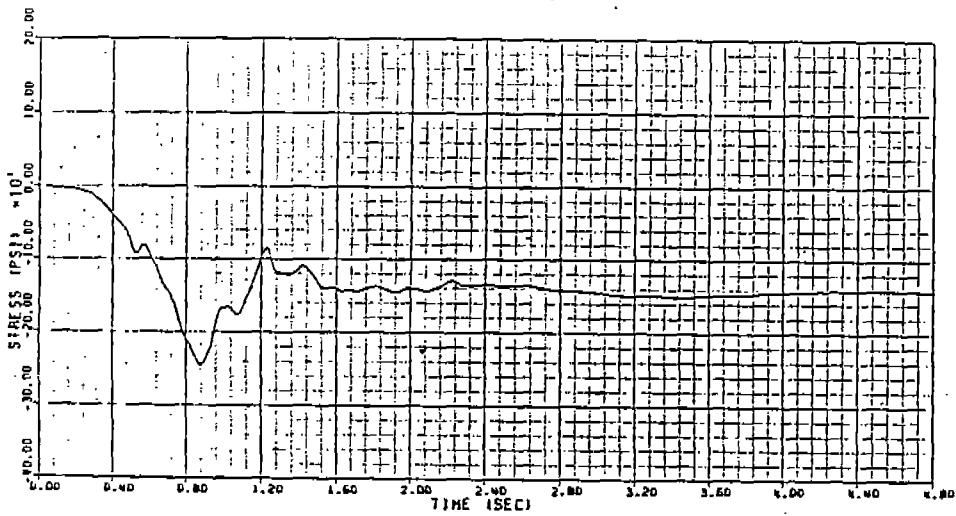
STRESS TIME-HISTORY OF ELEMENT   919   (B-01-C44-P&S)
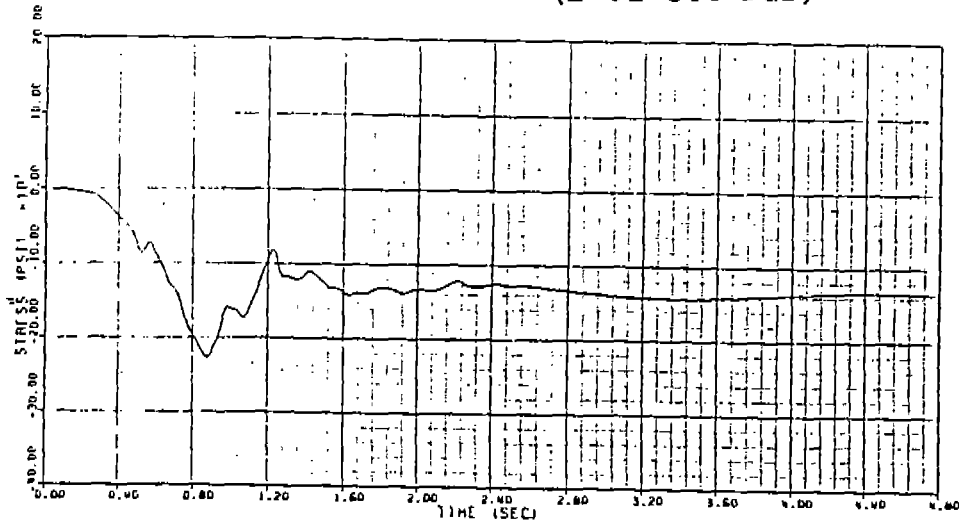
STRESS TIME-HISTORY OF ELEMENT   917
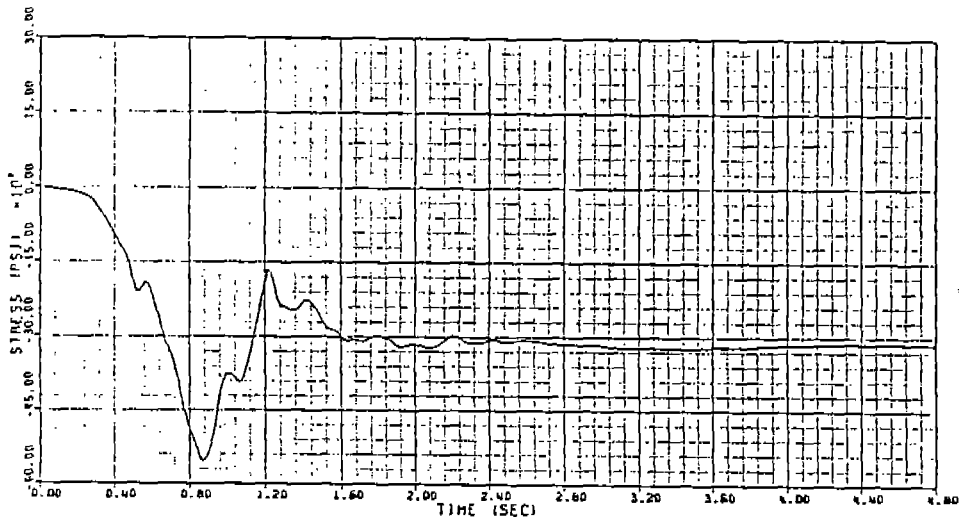
STRESS TIME-HISTORY OF ELEMENT   914   (B-01-39-P&S)
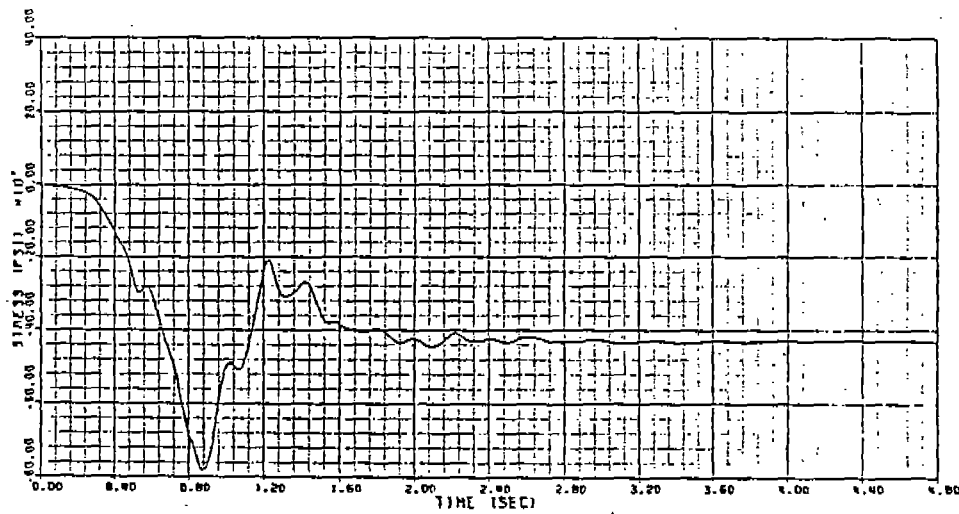
Figure 3.13 Stress Time History for Load case 5 (cont'd)

STRESS TIME-HISTORY OF ELEMENT   913   (B-01-55-P&S)
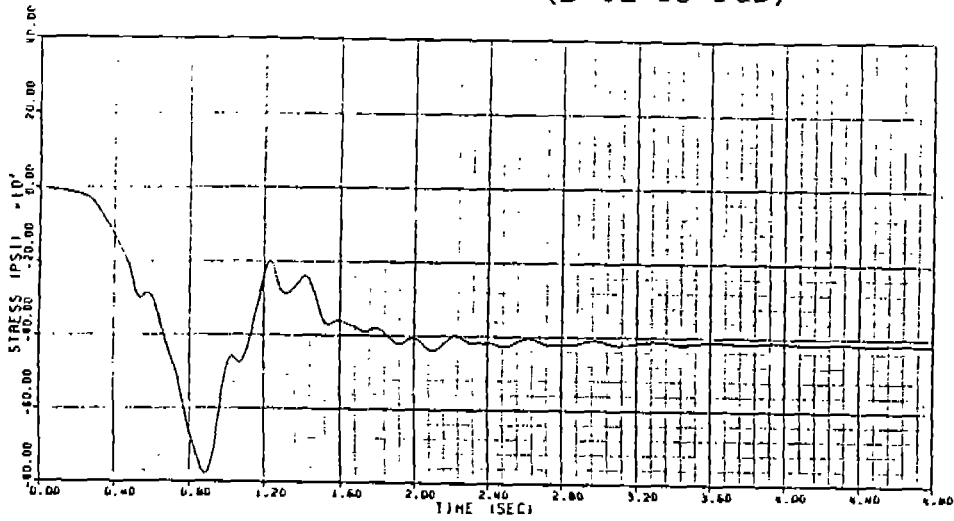
STRESS TIME-HISTORY OF ELEMENT   909   (B-01-86-P&S)
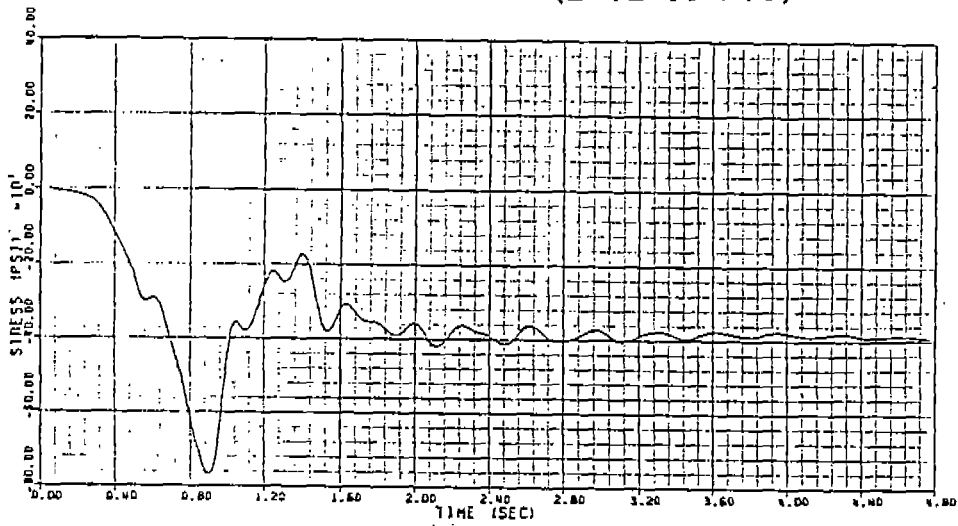
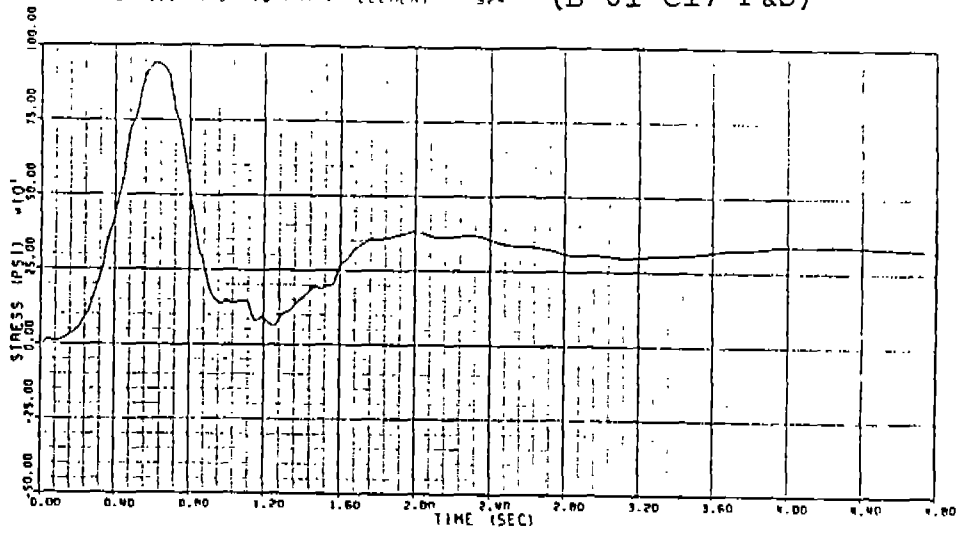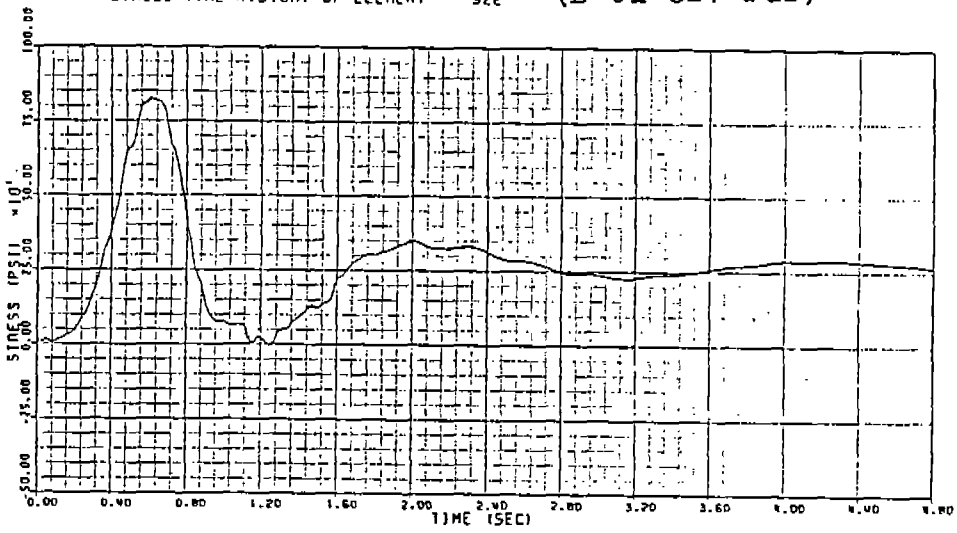STRESS TIME-HISTORY OF ELEMENT   906   (B-01-128-P&S)
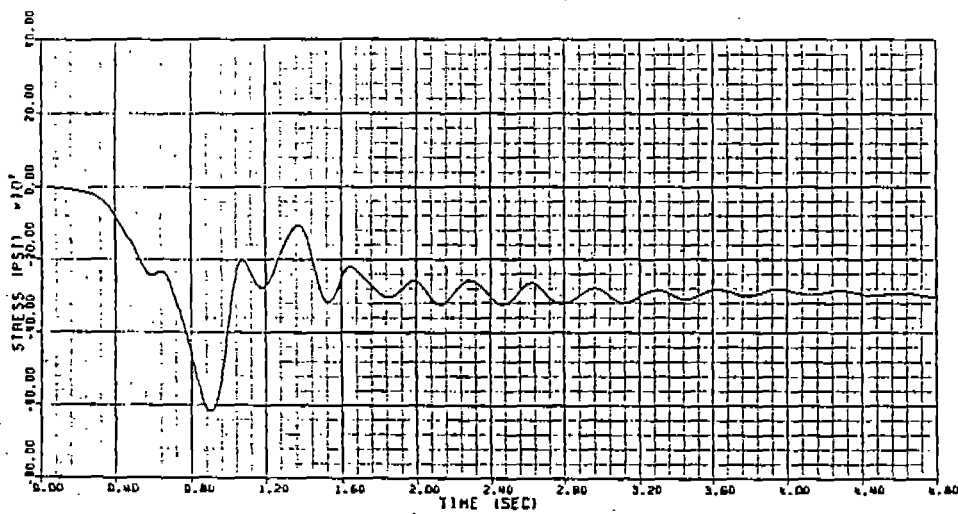
Figure 3.13 Stress Time History for Load case 5 (cont'd)

STRESS TIME-HISTORY OF ELEMENT 924 (B-01-C17-P&S)
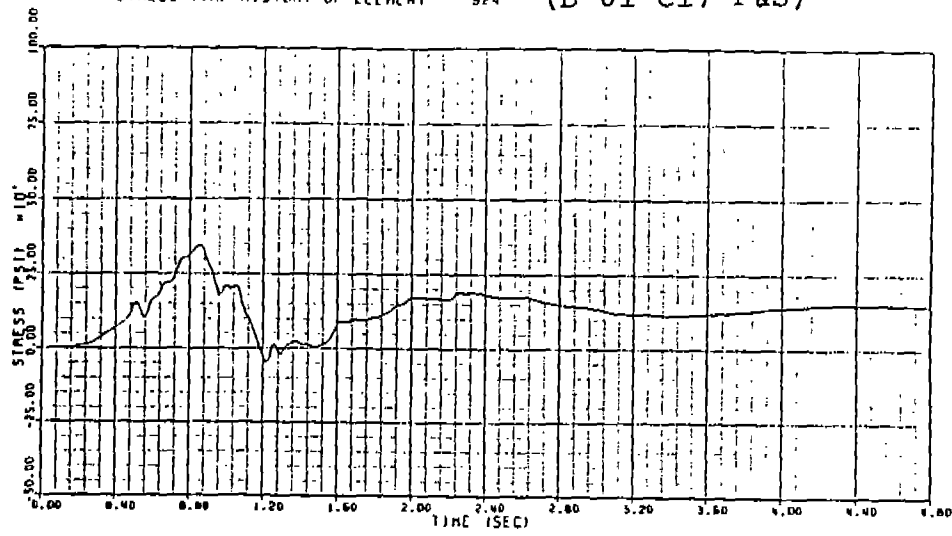
STRESS TIME-HISTORY OF ELEMENT 922 (B-01-C27-P&S)
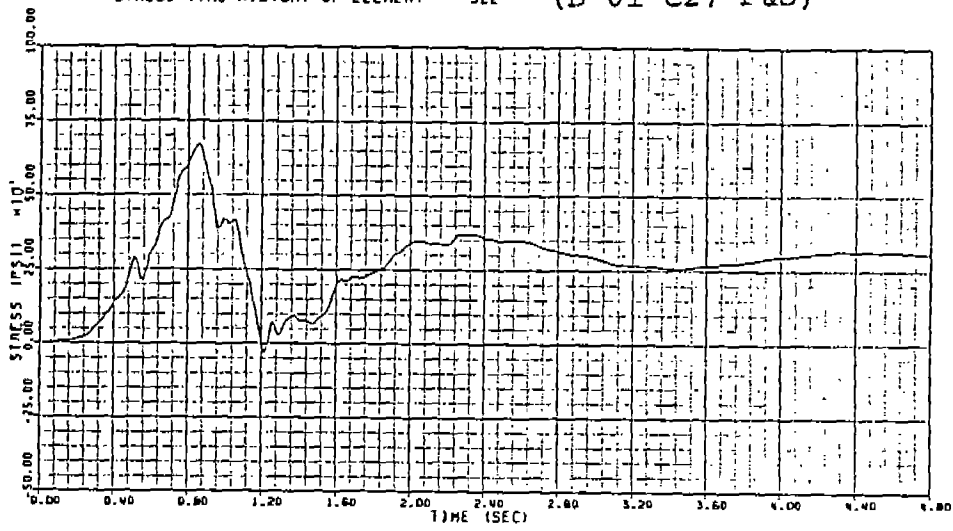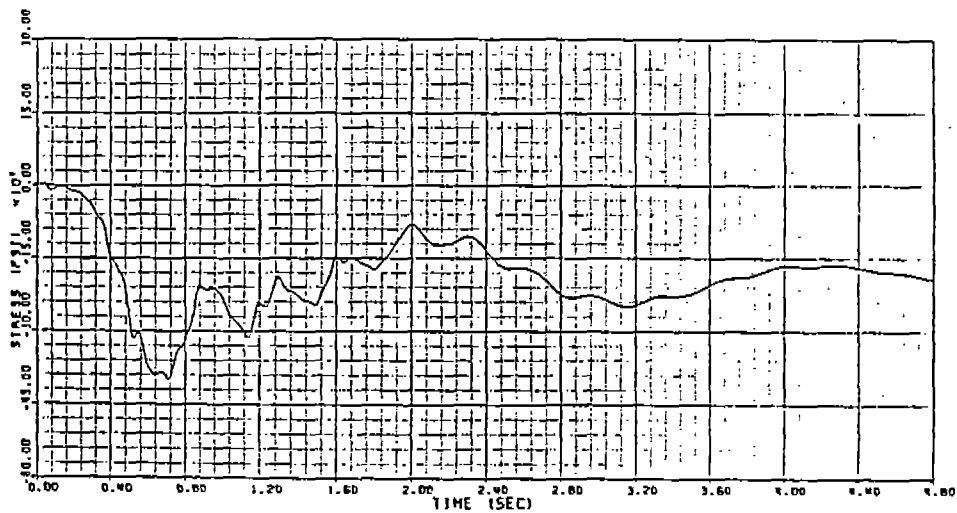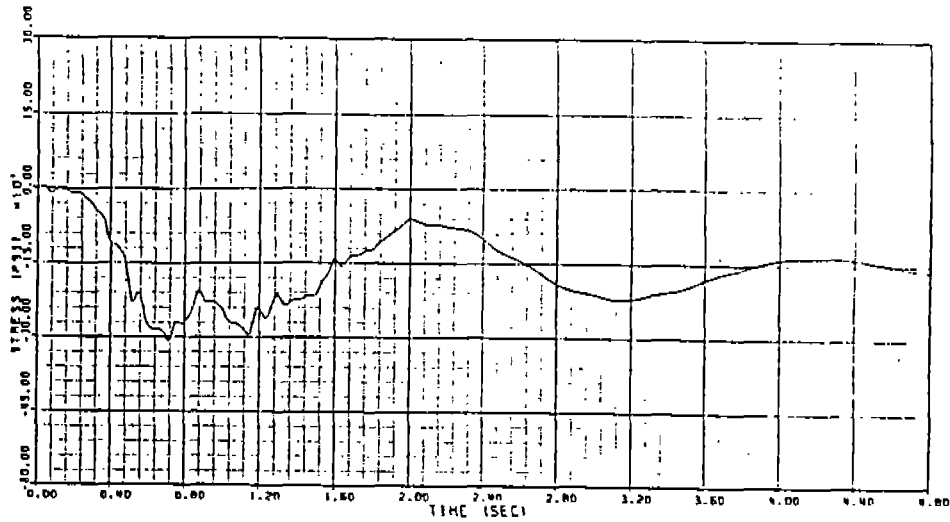
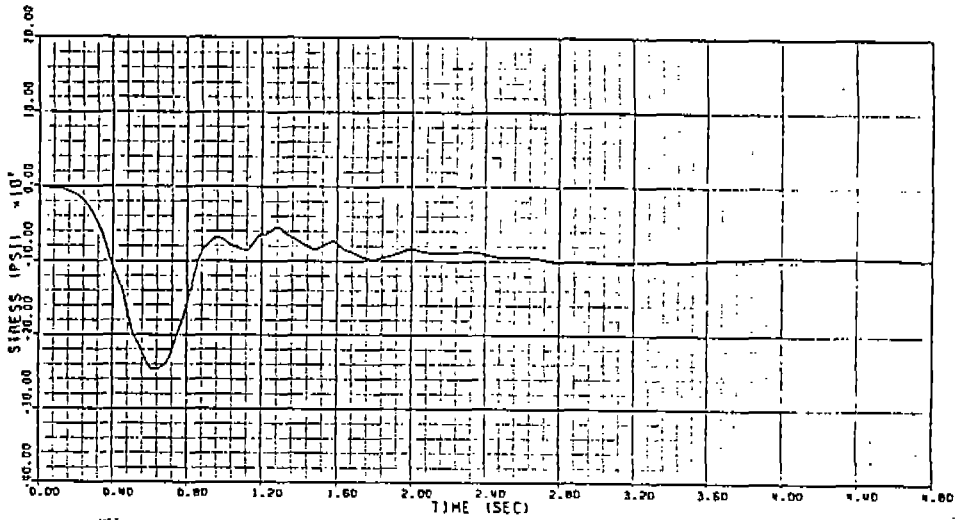STRESS TIME-HISTORY OF ELEMENT 921 (B-01-C35-P&S)

Figure 3.14 Stress Time History for Load case 6

-72-
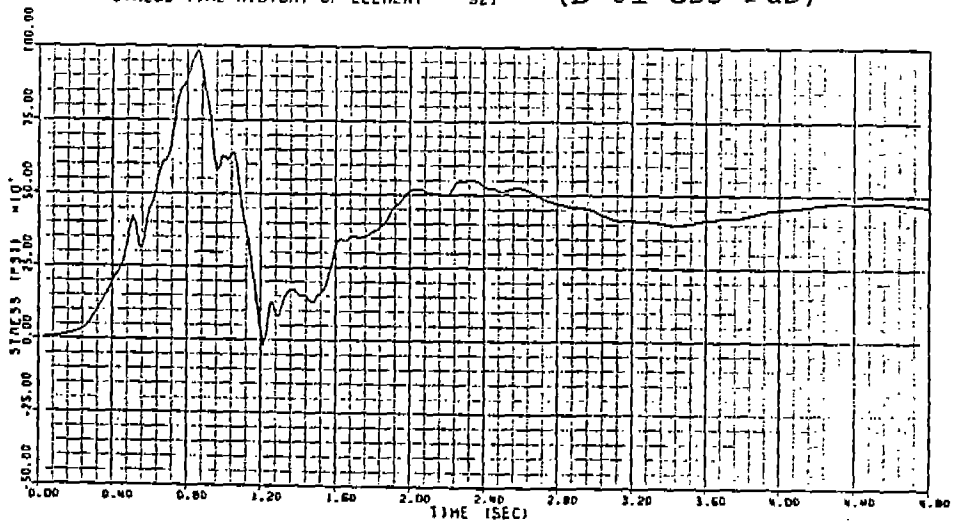
STRESS TIME-HISTORY OF ELEMENT   919   (B-01-C44-P&S)
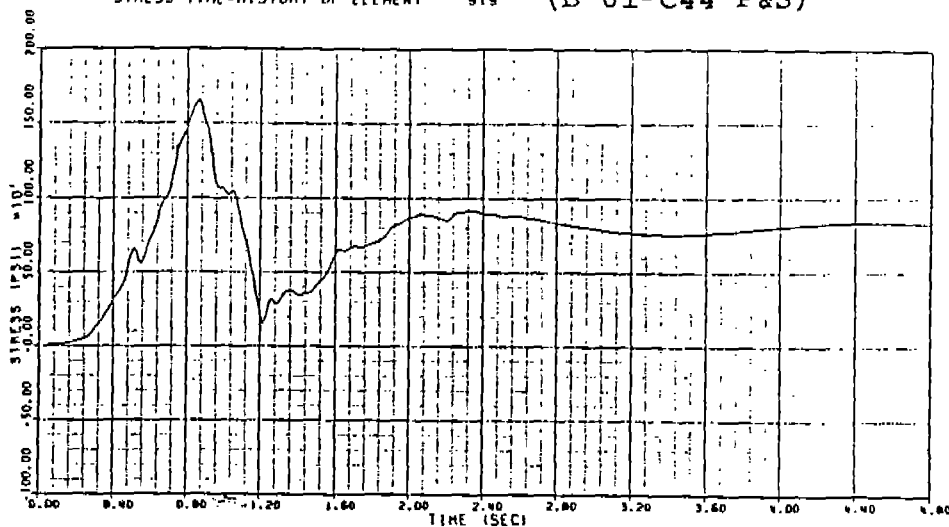
STRESS TIME-HISTORY OF ELEMENT   917

STRESS TIME-HISTORY OF ELEMENT   914   (B-01-39-P&S)

Figure 3.14   Stress Time History for Load case 6   (cont'd)

STRESS TIME-HISTORY OF ELEMENT   913   (B-01-55-P&S)

STRESS TIME-HISTORY OF ELEMENT   909   (B-01-86-P&S)

STRESS TIME-HISTORY OF ELEMENT   906   (B-01-128-P&S)

Figure 3.14 Stress Time History for Load case 6 (cont'd)

Figure 3.15 Stress Time History for Load case 7

STRESS TIME-HISTORY OF ELEMENT 919 (B-01-C44-P&S)

STRESS TIME-HISTORY OF ELEMENT 917
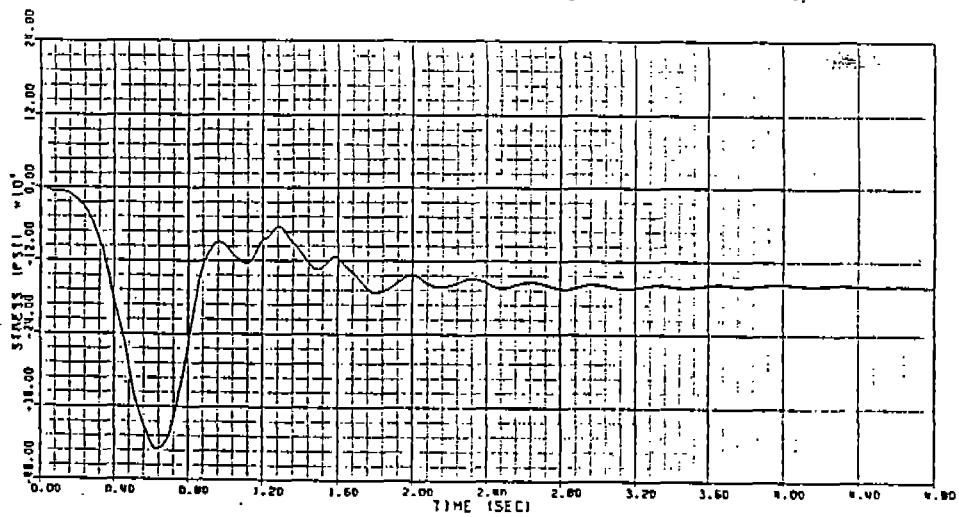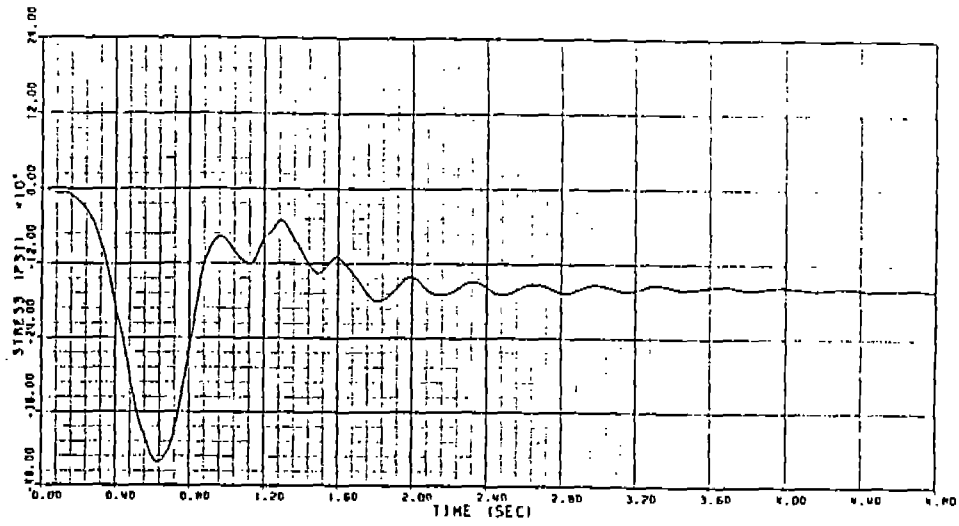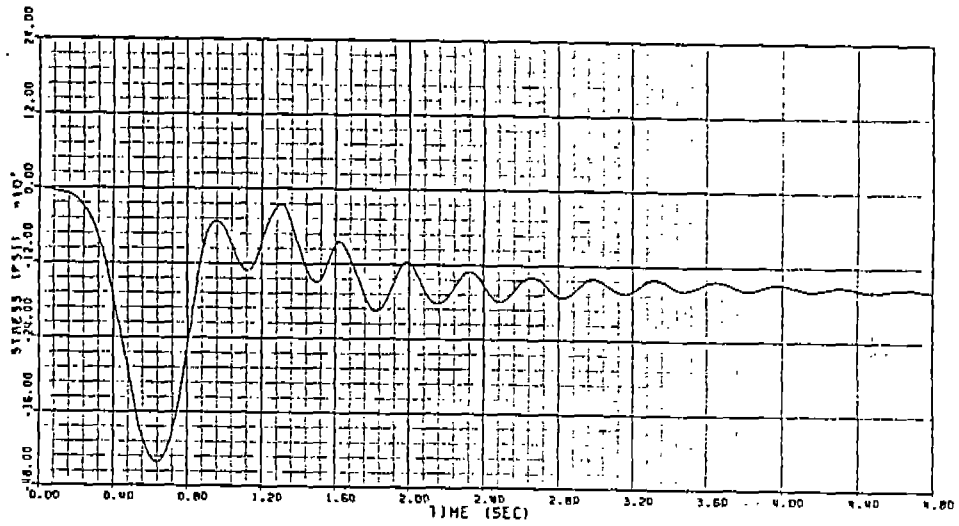
STRESS TIME-HISTORY OF ELEMENT 914 (B-01-39-P&S)

Figure 3.15 Stress Time History for Load case 7 (cont'd)

STRESS TIME-HISTORY OF ELEMENT   913   (B-01-55-P&S)

STRESS TIME-HISTORY OF ELEMENT   909   (B-01-86-P&S)
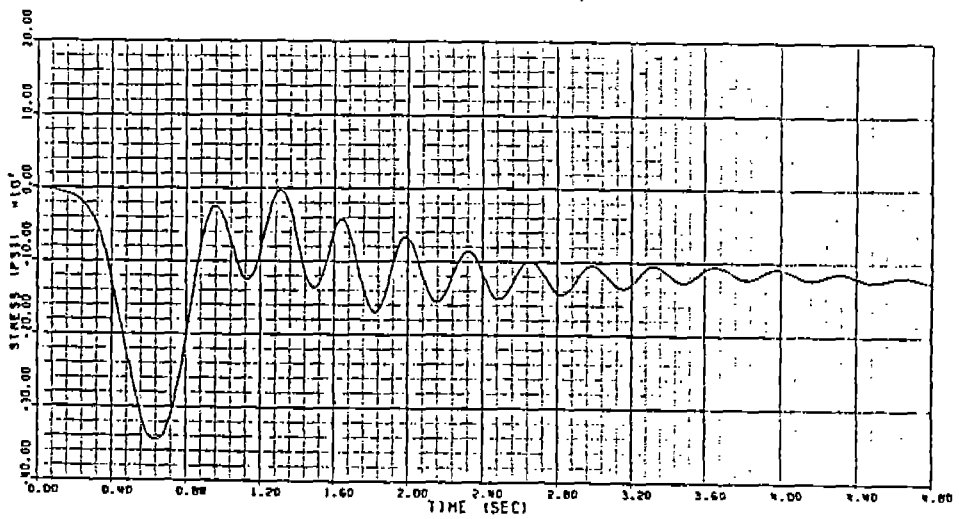
STRESS TIME-HISTORY OF ELEMENT   906   (B-01-128-P&S)

Figure 3.15 Stress Time History for Load case 7 (cont'd)

Figure 3.16 Stress Time History for Load case 8

STRESS TIME-HISTORY OF ELEMENT   919   (B-01-C44-P&S)

STRESS TIME-HISTORY OF ELEMENT   917

STRESS TIME-HISTORY OF ELEMENT   914   (B-01-39-P&S)

Figure 3.16 Stress Time History for Load case 8 (cont'd)

STRESS TIME-HISTORY OF ELEMENT   913   (B-01-55-P&S)

STRESS TIME-HISTORY OF ELEMENT   909   (B-01-86-P&S)

STRESS TIME-HISTORY OF ELEMENT   906   (B-01-128-P&S)
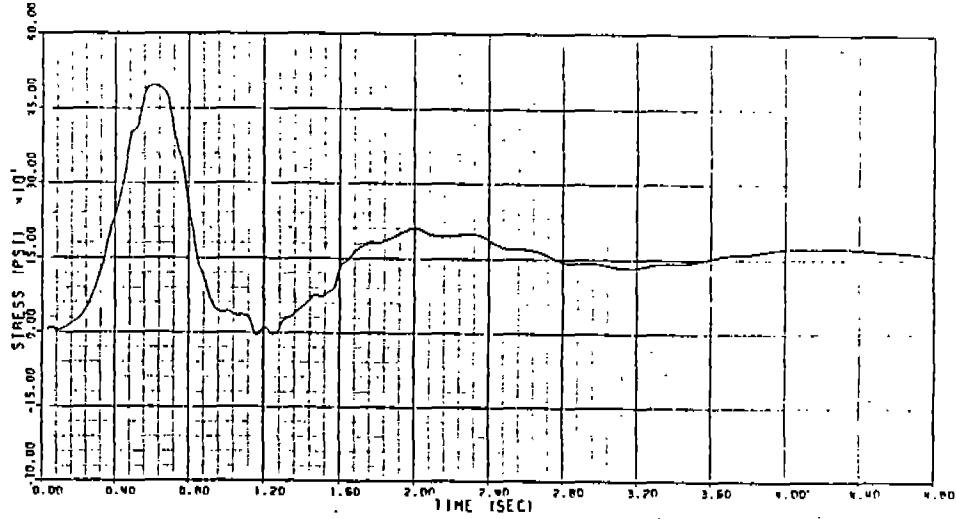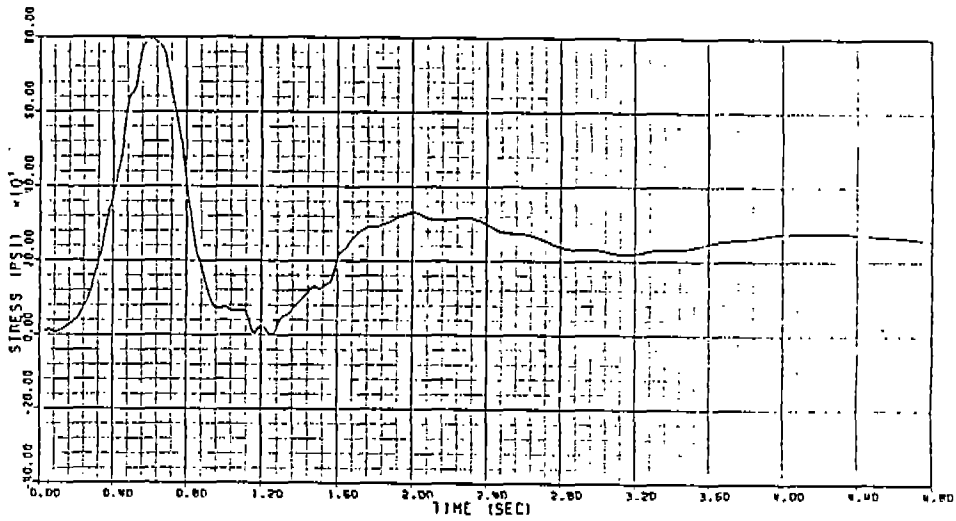
Figure 3.16 Stress Time History for Load case 8 (cont'd)

STRESS TIME-HISTORY OF ELEMENT   924   (B-01-C17-P&S)

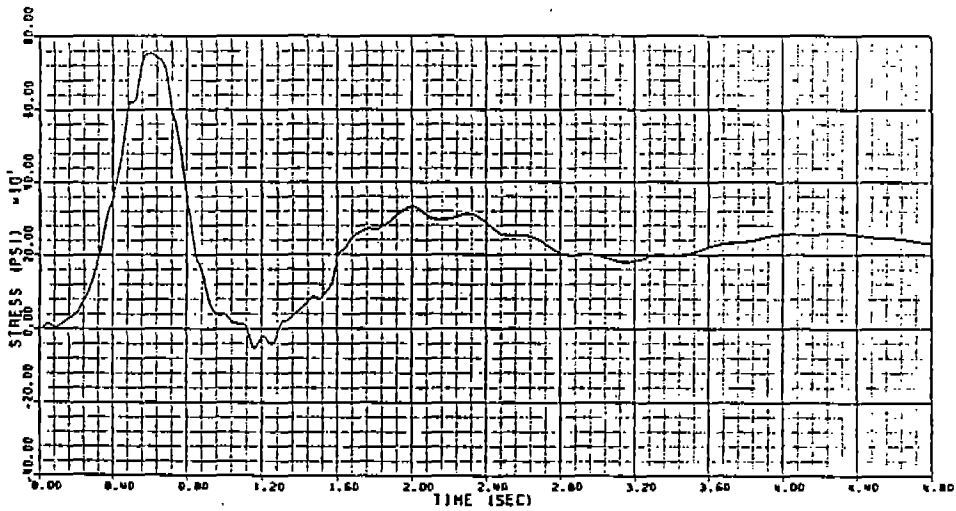STRESS TIME-HISTORY OF ELEMENT   922   (B-01-C27-P&S)

STRESS TIME-HISTORY OF ELEMENT   921   (B-01-C35-P&S)

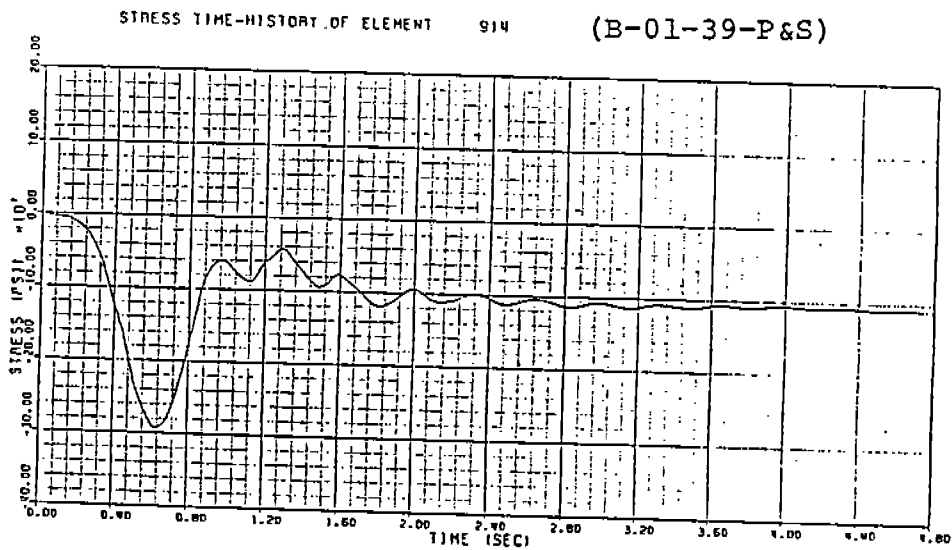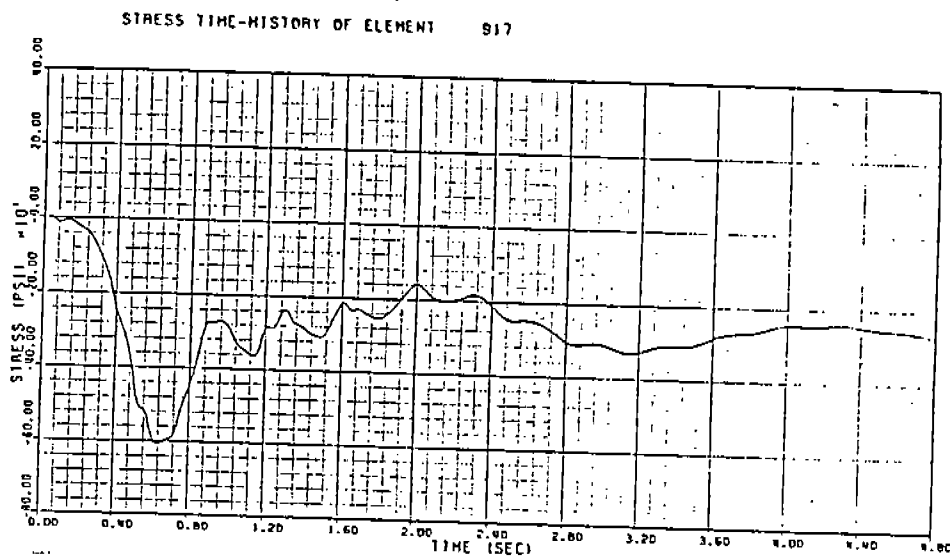Figure 3.17 Stress Time History for Load case 9
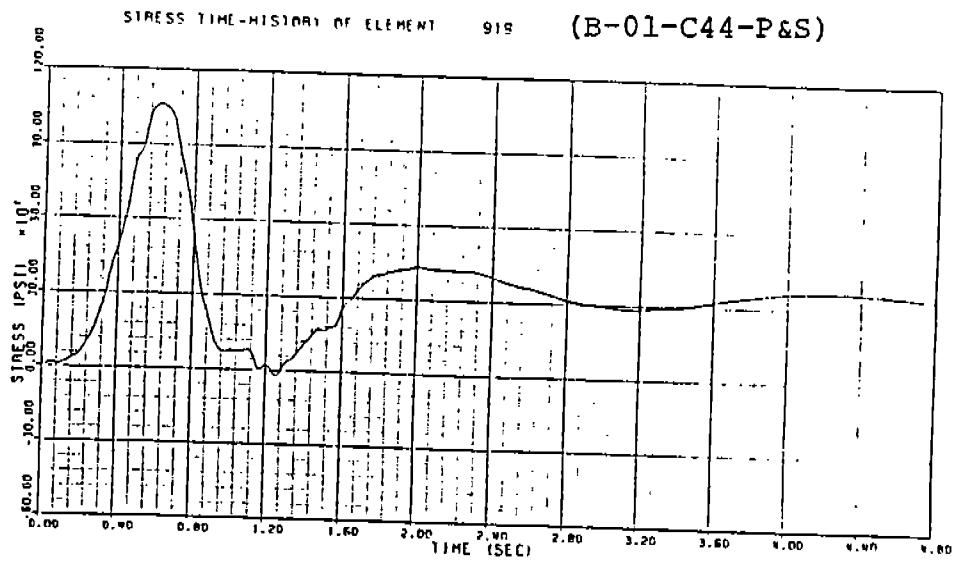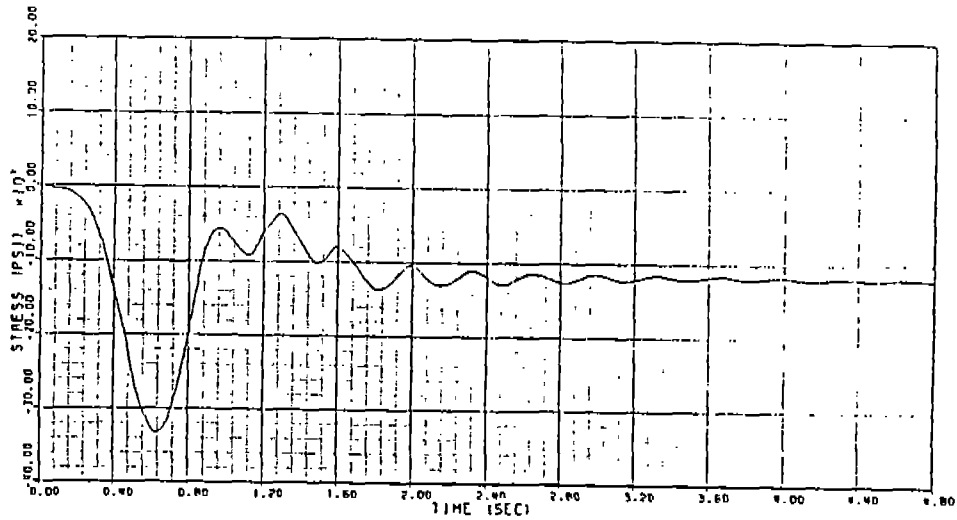
-81-

Figure 3.17 Stress Time History for Load case 9 (cont'd)

STRESS TIME-HISTORY OF ELEMENT   913   (B-01-55-P&S)

STRESS TIME-HISTORY OF ELEMENT   909   (B-01-86-P&S)

STRESS TIME-HISTORY OF ELEMENT   906   (B-01-128-P&S)

Figure 3.17 Stress Time History for Load case 9 (cont'd)

-83-

DISPLACEMENT TIME-HISTORY OF NODE 1382   (vertical disp.)

DISPLACEMENT TIME-HISTORY OF NODE 1349   (vertical disp.)

DISPLACEMENT TIME-HISTORY OF NODE 1349   (longitudinal disp.)

Figure 3.18 Displacement Time History for Load case 5

-84-

DISPLACEMENT TIME-HISTORY OF NODE 1236   (vertical disp.)

DISPLACEMENT TIME-HISTORY OF NODE 926   (vertical disp.)

DISPLACEMENT TIME-HISTORY OF NODE 926   (longitudinal disp.)

Figure 3.18 Displacement Time History for Load case 5 (cont'd)

-85-
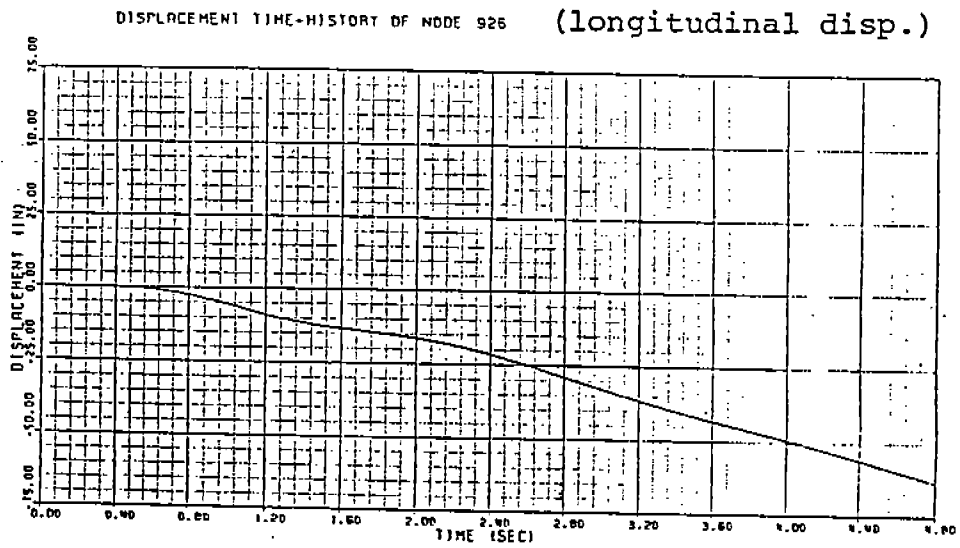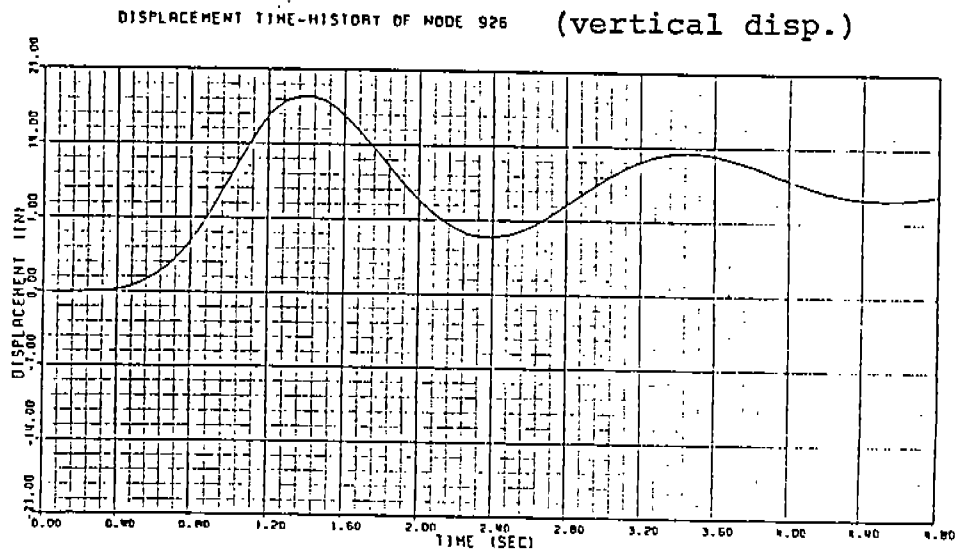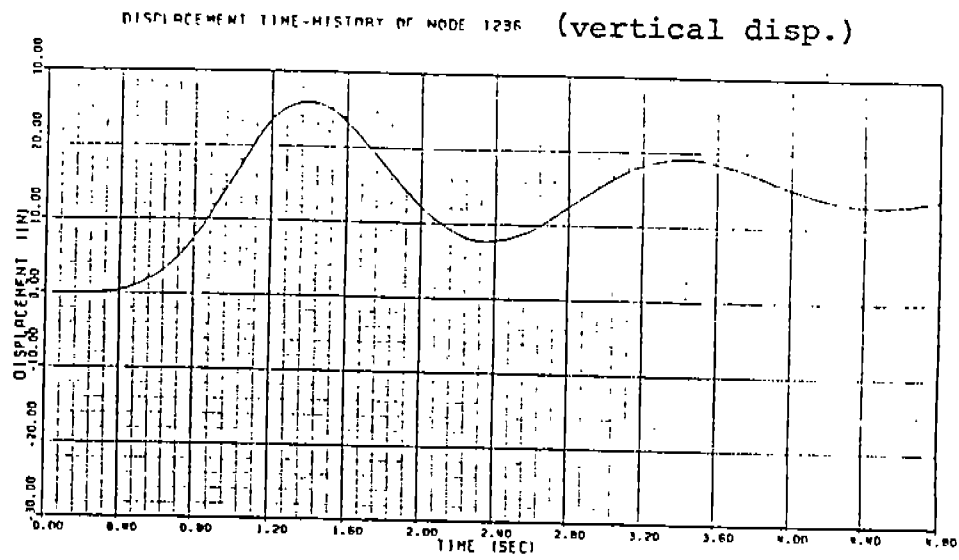
DISPLACEMENT TIME-HISTORY OF NODE 589 (vertical disp.)

DISPLACEMENT TIME-HISTORY OF NODE 339 (vertical disp.)

DISPLACEMENT TIME-HISTORY OF NODE 18 (vertical disp.)

Figure 3.18 Displacement Time History for Load case 5 (cont'd)

-86-

DISPLACEMENT TIME-HISTORY OF NODE 1382   (vertical disp.)

DISPLACEMENT TIME-HISTORY OF NODE 1349   (vertical disp.)
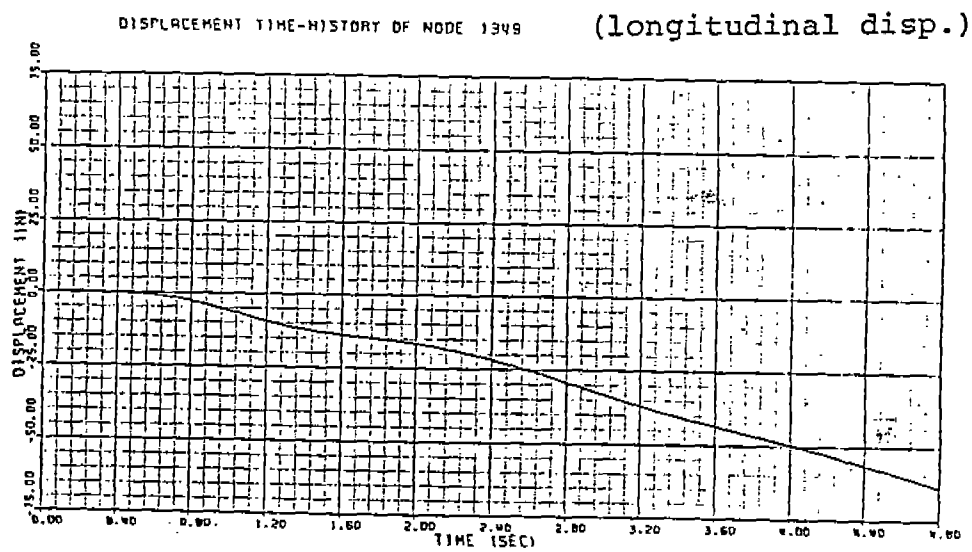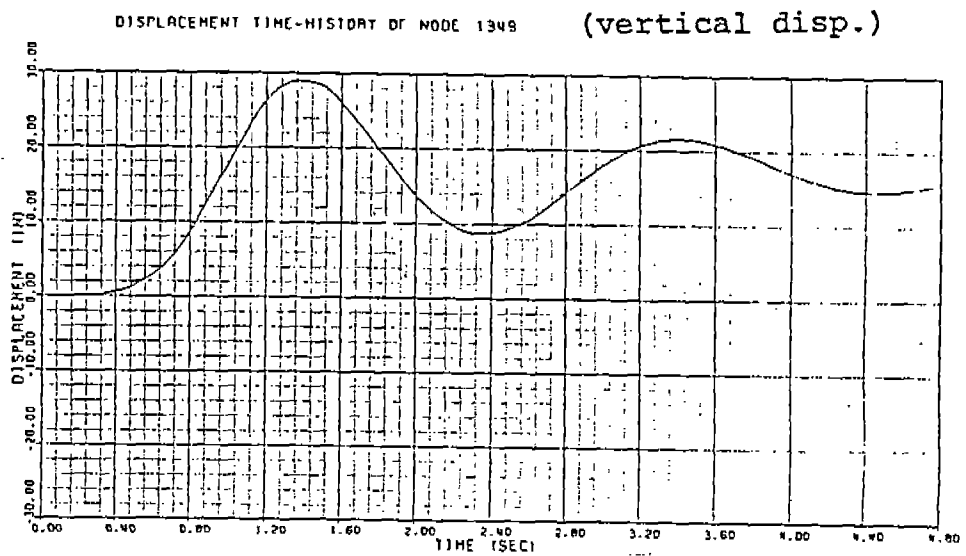
DISPLACEMENT TIME-HISTORY OF NODE 1349   (longitudinal disp.)

Figure 3.19 Displacement Time History for Load case 8

-87-

DISPLACEMENT TIME-HISTORY OF NODE 1236   (vertical disp.)

DISPLACEMENT TIME-HISTORY OF NODE 926   (vertical disp.)
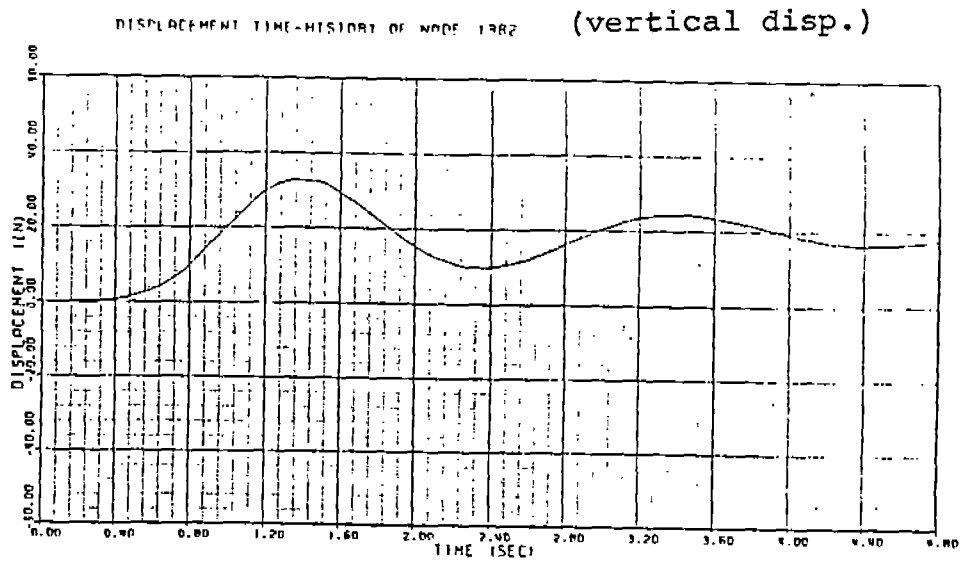
DISPLACEMENT TIME-HISTORY OF NODE 926   (longitudinal disp.)

Figure 3.19 Displacement Time History for Load case 8 (cont'd)

DISPLACEMENT TIME-HISTORY OF NODE 589   (vertical disp.)

DISPLACEMENT TIME-HISTORY OF NODE 339   (vertical disp.)

DISPLACEMENT TIME-HISTORY OF NODE 18   (longitudinal disp.)

Figure 3.19 Displacement Time History for Load case 8 (cont'd)

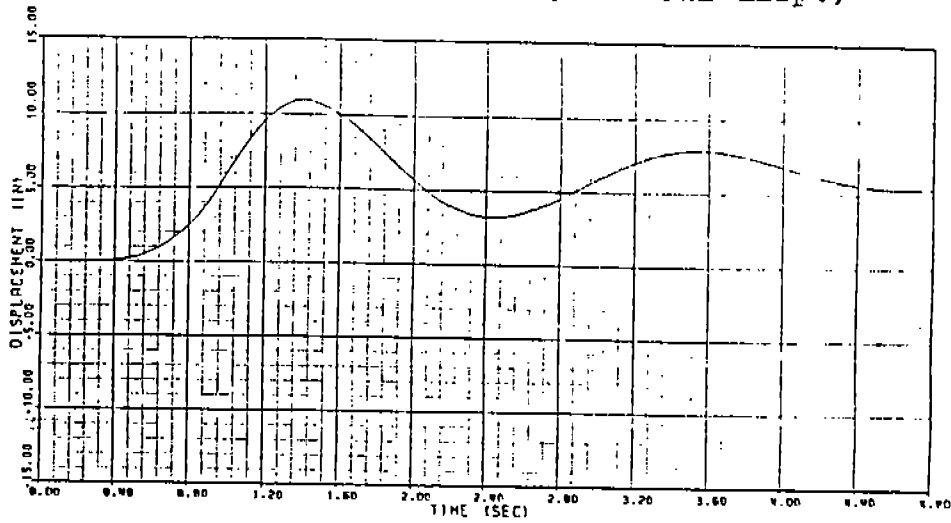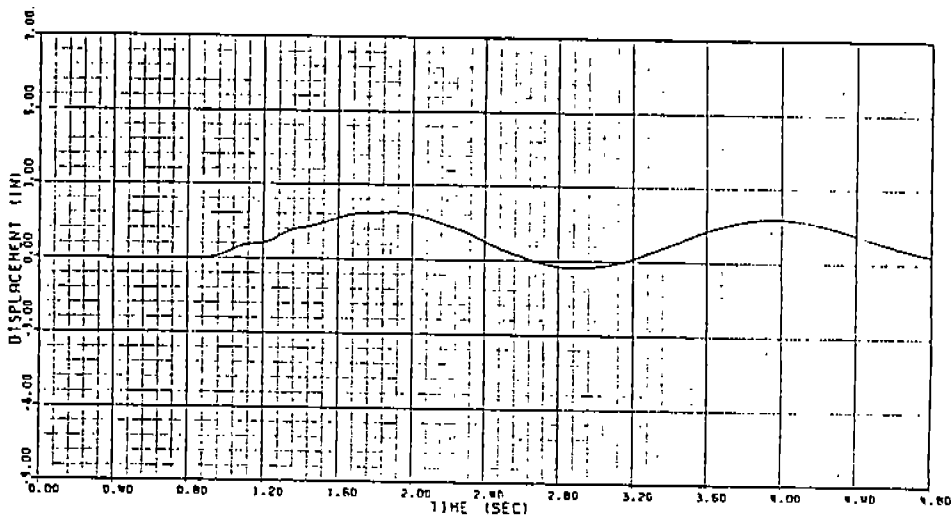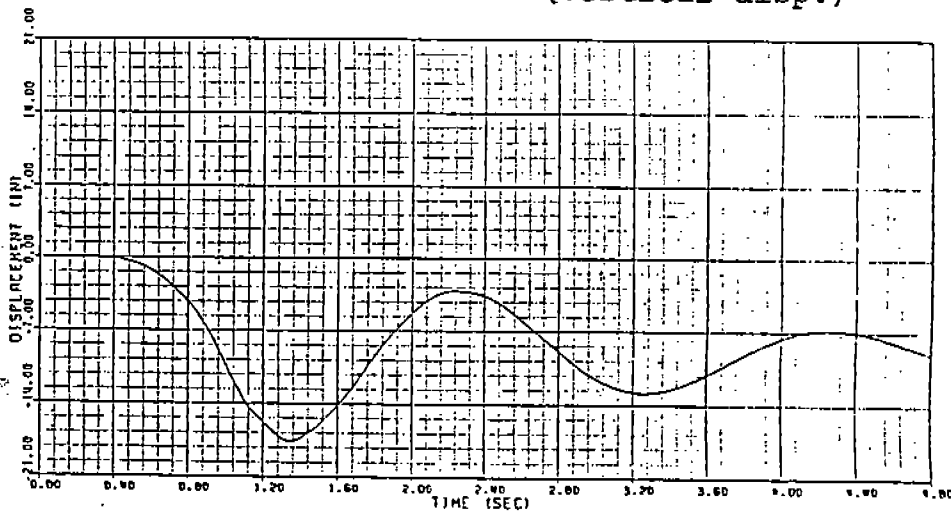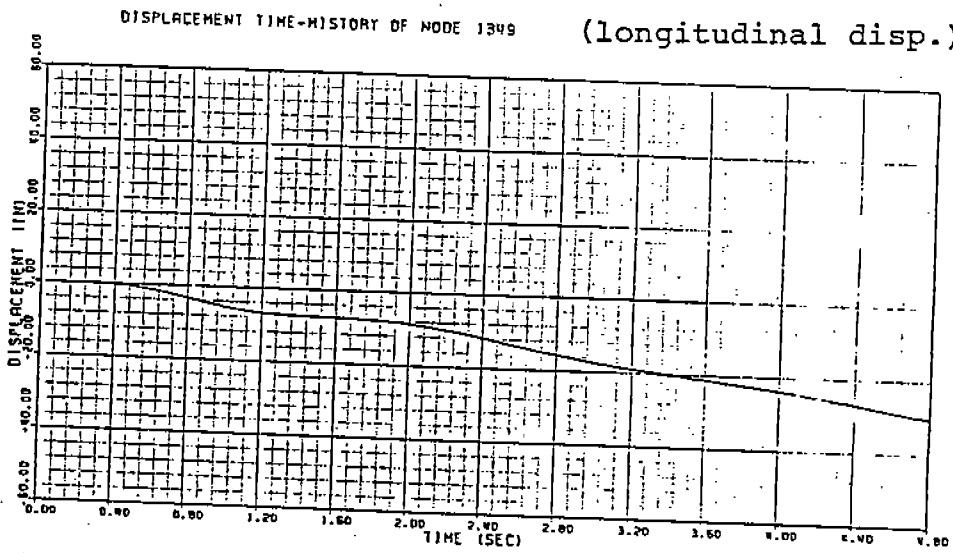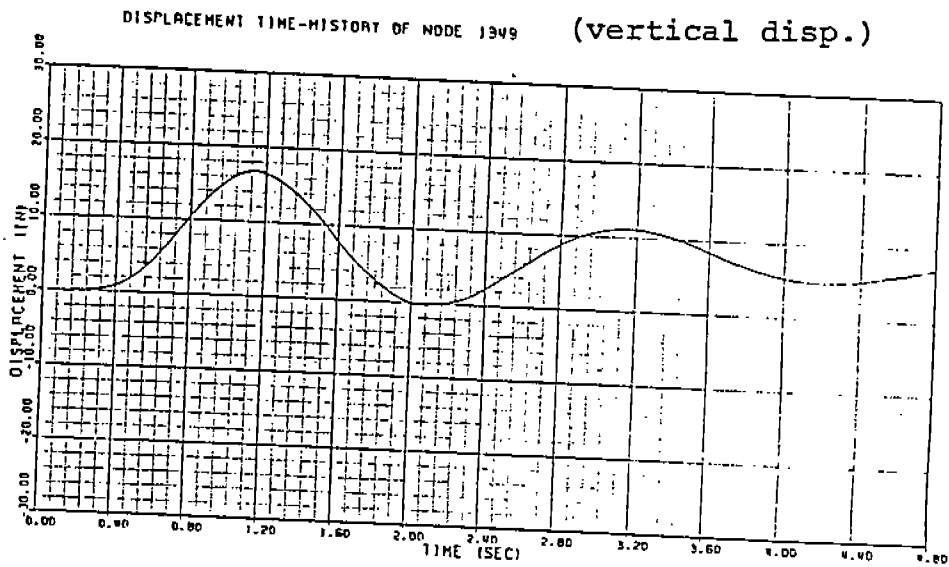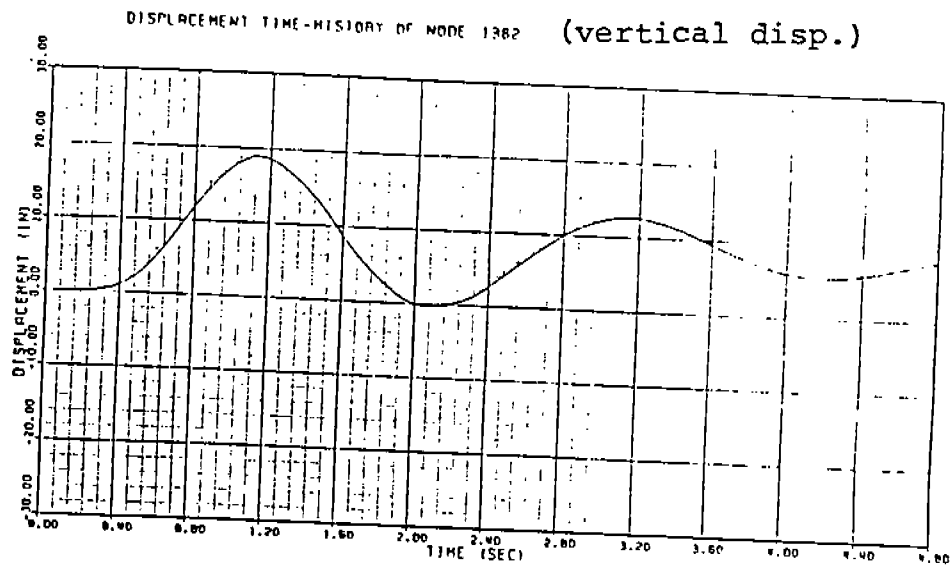-89-
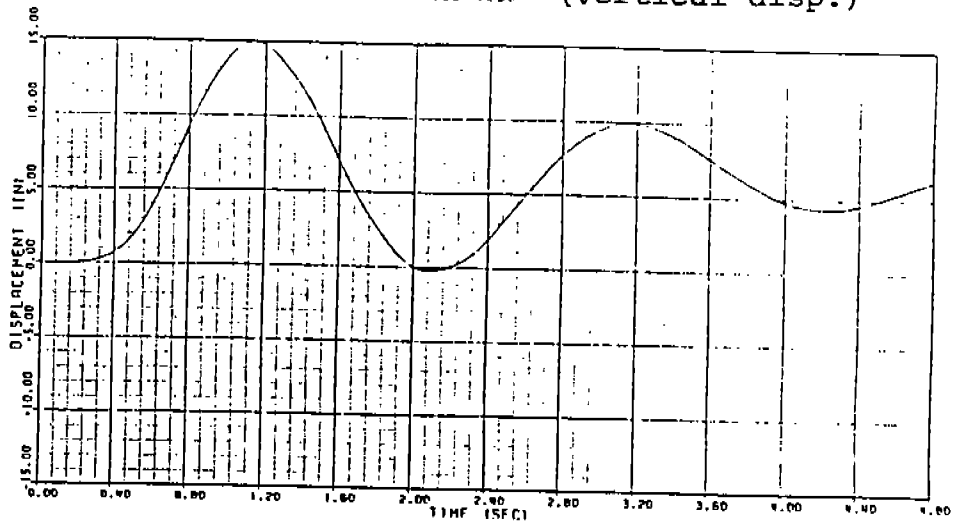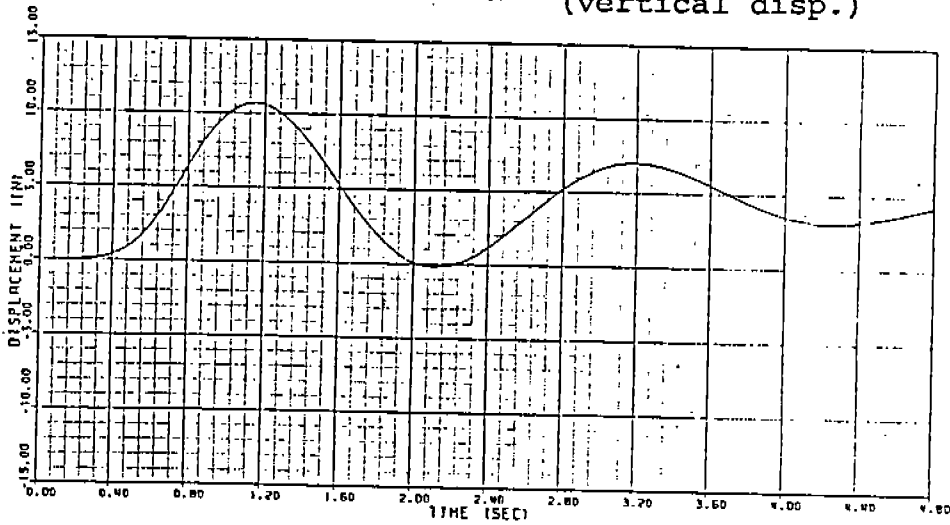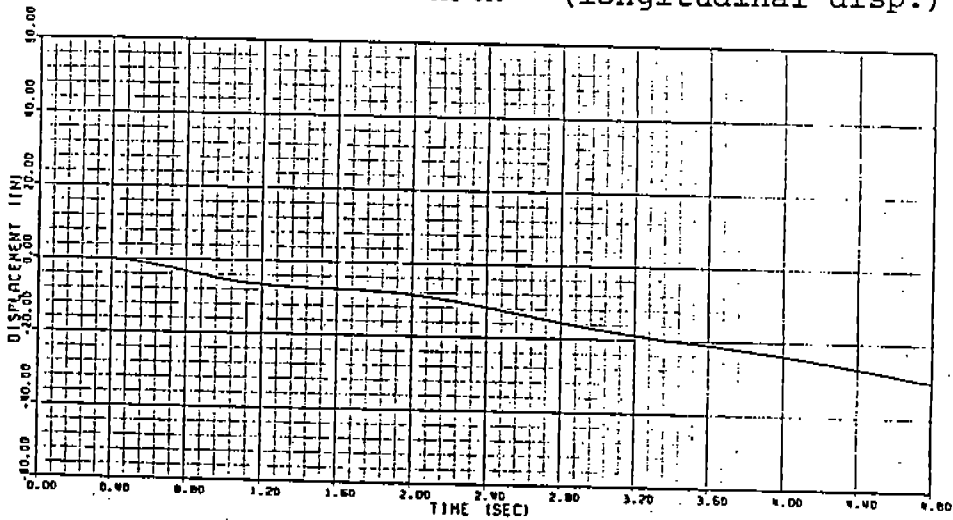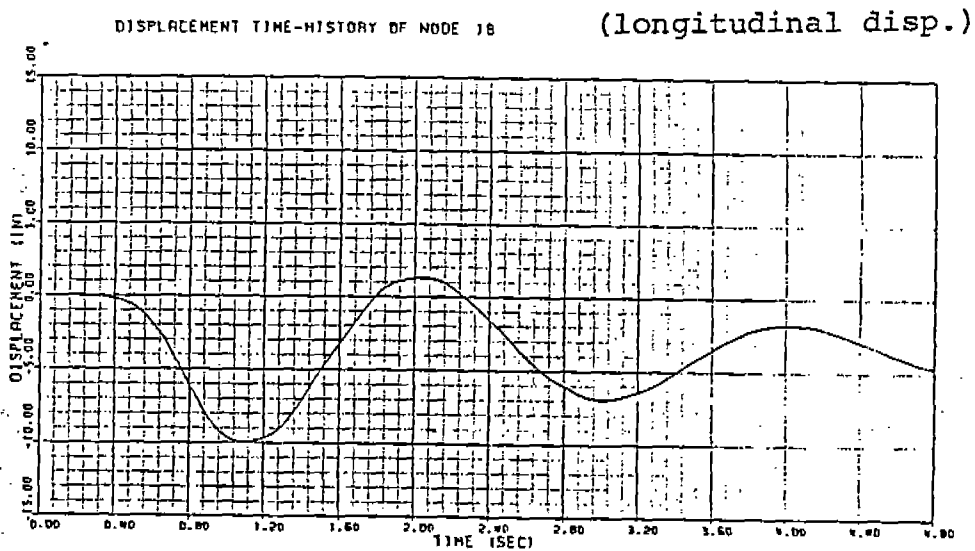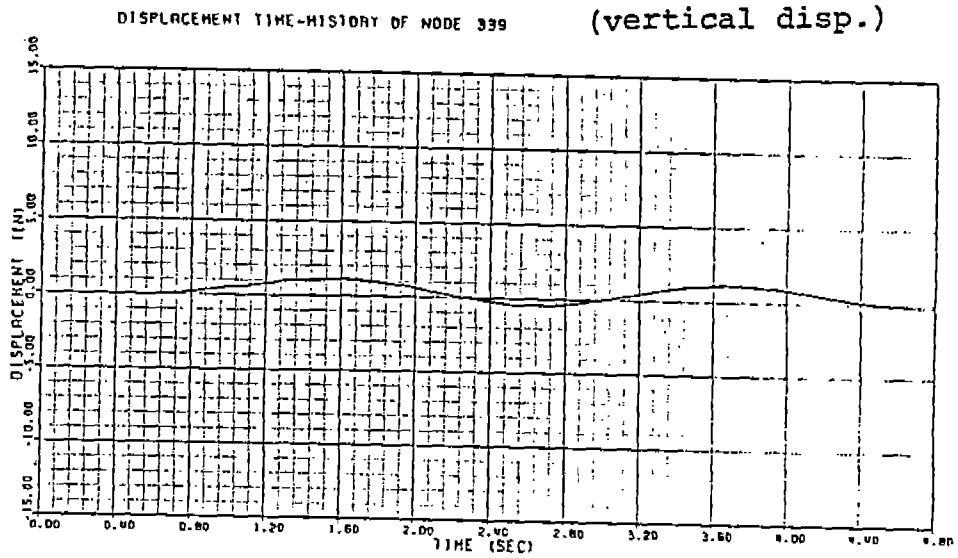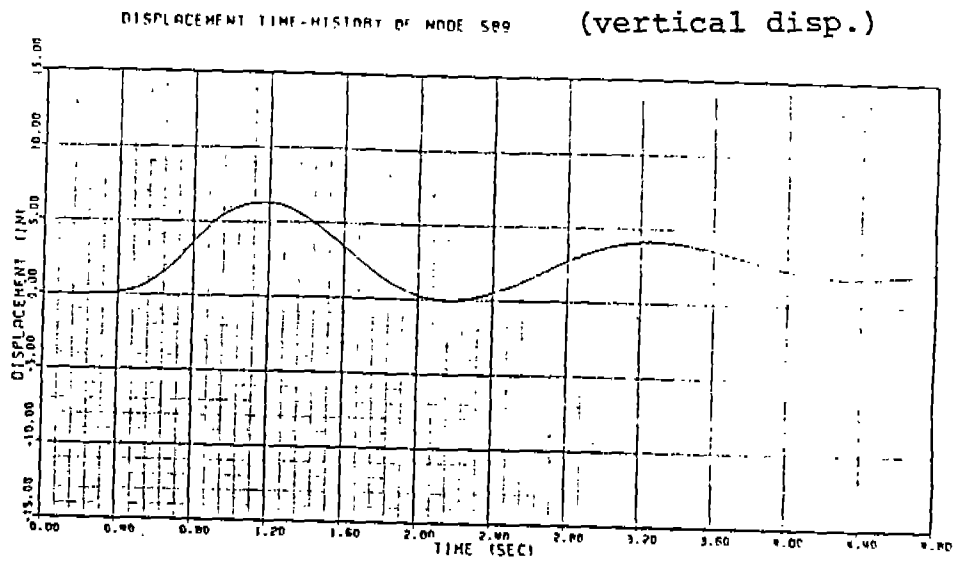
Table 3.3 Peak Stress (psi) on level-01 Deck for Load case 1
(Triangular shape, Load location A)

Ship Fr. No.	Strain Gage Location	Element No.	Time Instant (sec)	Peak Stress (psi)
258		897	0.760	6.1
248		898	0.760	8.2
238		899	0.750	12.3
228		900	0.780	-8.3
217		901	0.760	-32.1
204		902	0.760	-45.9
192		903	0.740	5.0
150		904	0.700	-127.8
132		905	0.740	-202.1
128	B-01-128-P&S	906	0.700	-423.8
106		907	0.700	-467.6
96		908	0.690	-532.3
86	B-01- 86-P&S	909	0.690	-560.3
82		910	0.690	-554.8
74		911	0.690	-492.8
63		912	0.680	-511.9
55	B-01- 55-P&S	913	0.680	-597.8
39	B-01- 39-P&S	914	0.680	-610.2
CF67		915	0.680	-532.9
CF60		916	0.680	-506.0
CF53		917	0.680	-439.6
CF48		918	0.680	-333.7
CF44	B-01-C44-P&S	919	0.690	-182.7
CF39		920	0.690	-225.3
CF35	B-01-C35-P&S	921	0.690	-195.7
CF27	B-01-C27-P&S	922	1.070	-22.7
CF25		923	1.070	-23.3
CF17	B-01-C17-P&S	924	0.670	117.7
CF16		925	0.670	103.9
CF14		926	0.670	64.9
CF 8		927	0.670	44.1

Table 3.4   Peak Stress (psi) on level-01 Deck for Load case 2
            (Concave trigonometric curve, Load location A)

Ship Fr. No.	Strain Gage Location	Element No.	Time Instant (sec)	Peak Stress (psi)
258		897	0.740	6.2
248		898	0.730	8.6
238		899	0.730	12.9
228		900	0.760	-8.3
217		901	0.750	-33.0
204		902	0.740	-47.5
192		903	0.730	5.2
150		904	0.720	-134.8
132		905	0.740	-217.8
128	B-01-128-P&S	906	0.710	-442.2
106		907	0.700	-483.3
96		908	0.700	-547.6
86	B-01- 86-P&S	909	0.700	-573.7
82		910	0.690	-566.0
74		911	0.690	-500.6
63		912	0.690	-517.9
55	B-01- 55-P&S	913	0.680	-602.2
39	B-01- 39-P&S	914	0.680	-610.9
CF67		915	0.680	-531.7
CF60		916	0.680	-503.0
CF53		917	0.680	-435.0
CF48		918	0.680	-329.4
CF44	B-01-C44-P&S	919	0.680	-178.5
CF39		920	0.690	-221.0
CF35	B-01-C35-P&S	921	0.690	-192.9
CF27	B-01-C27-P&S	922	0.660	20.9
CF25		923	0.660	23.5
CF17	B-01-C17-P&S	924	0.670	119.6
CF16		925	0.670	104.9
CF14		926	0.670	64.8
CF 8		927	0.680	43.7

Table 3.5   Peak Stress (psi) on level-01 Deck for Load case 3
(Convex trigonometric curve, Load location A)

Ship Fr. No.	Strain Gage Location	Element No.	Time Instant (sec)	Peak Stress (psi)
258		897	0.610	6.5
248		898	0.600	8.8
238		899	0.600	13.3
228		900	0.610	-9.0
217		901	0.610	-35.2
204		902	0.600	-50.5
192		903	0.600	5.5
150		904	0.600	-137.6
132		905	0.600	-219.3
128	B-01-128-P&S	906	0.600	-440.6
106		907	0.600	-478.1
96		908	0.610	-539.3
86	B-01- 86-P&S	909	0.620	-563.9
82		910	0.630	-556.8
74		911	0.630	-493.2
63		912	0.640	-512.1
55	B-01- 55-P&S	913	0.640	-597.4
39	B-01- 39-P&S	914	0.650	-610.0
CF67		915	0.670	-533.8
CF60		916	0.680	-508.4
CF53		917	0.680	-443.4
CF48		918	0.690	-337.4
CF44	B-01-C44-P&S	919	0.690	-186.4
CF39		920	0.690	-228.6
CF35	B-01-C35-P&S	921	0.690	-197.5
CF27	B-01-C27-P&S	922	1.060	-25.2
CF25		923	1.160	-25.5
CF17	B-01-C17-P&S	924	0.610	116.7
CF16		925	0.660	103.3
CF14		926	0.670	65.1
CF 8		927	0.670	44.5

Table 3.6   Peak Stress (psi) on level-01 Deck for Load case 4
            (ABS theoretical bow force, Load location A)

Ship Fr. No.	Strain Gage Location	Element No.	Time Instant (sec)	Peak Stress (psi)
258		897	1.260	9.0
248		898	1.260	10.3
238		899	1.260	16.0
228		900	1.250	−19.3
217		901	1.250	−57.0
204		902	1.250	−73.8
192		903	1.260	6.0
150		904	0.720	−131.4
132		905	1.130	237.7
128	B-01-128-P&S	906	0.720	−429.7
106		907	0.720	−471.5
96		908	0.720	−535.0
86	B-01- 86-P&S	909	0.720	−561.6
82		910	0.730	−555.6
74		911	0.730	−493.1
63		912	0.730	−512.7
55	B-01- 55-P&S	913	0.730	−598.3
39	B-01- 39-P&S	914	0.730	−610.5
CF67		915	0.740	−533.5
CF60		916	0.740	−506.9
CF53		917	0.740	−440.4
CF48		918	0.750	−334.3
CF44	B-01-C44-P&S	919	1.030	232.1
CF39		920	1.030	275.7
CF35	B-01-C35-P&S	921	1.030	249.3
CF27	B-01-C27-P&S	922	1.010	−252.9
CF25		923	1.010	−281.8
CF17	B-01-C17-P&S	924	1.010	−315.2
CF16		925	1.010	−228.3
CF14		926	1.010	−71.0
CF 8		927	1.020	−47.1

Table 3.7   Peak Stress (psi) on level-01 Deck for Load case 5
(Ram 39, Load loaction A)

Ship Fr. No.	Strain Gage Location	Element No.	Time Instant (sec)	Peak Stress (psi)
258		897	0.928	87.2
248		898	0.912	120.9
238		899	0.912	182.0
228		900	1.216	-123.3
217		901	0.928	-465.0
204		902	0.928	-671.9
192		903	0.912	74.6
150		904	0.896	-1921.0
132		905	0.912	-3076.0
128	B-01-128-P&S	906	0.896	-6173.0
106		907	0.896	-6628.0
96		908	0.896	-7410.0
86	B-01- 86-P&S	909	0.896	-7689.0
82		910	0.896	-7523.0
74		911	0.896	-6567.0
63		912	0.880	-6744.0
55	B-01- 55-P&S	913	0.880	-7793.0
39	B-01- 39-P&S	914	0.880	-7846.0
CF67		915	0.880	-6814.0
CF60		916	0.880	-6426.0
CF53		917	0.880	-5539.0
CF48		918	0.880	-4195.0
CF44	B-01-C44-P&S	919	0.880	-2275.0
CF39		920	0.880	-2825.0
CF35	B-01-C35-P&S	921	0.880	-2463.0
CF27		922	0.736	249.4
CF25	B-01-C27-P&S	923	0.736	282.0
CF17	B-01-C17-P&S	924	0.864	1503.0
CF16		925	0.864	1323.0
CF14		926	0.864	826.0
CF 8		927	0.864	561.3

Table 3.8   Peak Stress (psi) on level-01 Deck for Load case 6
             (Ram 39, Load location B)

Ship Fr. No.	Strain Gage Location	Element No.	Time Instant (sec)	Peak Stress (psi)
258		897	0.912	63.5
248		898	0.912	86.6
238		899	0.912	130.9
228		900	0.928	-91.0
217		901	0.912	-349.9
204		902	0.912	-502.8
192		903	0.912	55.2
150		904	0.896	-1388.0
132		905	0.896	-2332.0
128	B-01-128-P&S	906	0.896	-4317.0
106		907	0.896	-4476.0
96		908	0.896	-4871.0
86	B-01- 86-P&S	909	0.896	-4936.0
82		910	0.896	-4637.0
74		911	0.896	-3820.0
63		912	0.880	-3575.0
55	B-01- 55-P&S	913	0.880	-3508.0
39	B-01- 39-P&S	914	0.896	-2513.0
CF67		915	0.896	-1585.0
CF60		916	0.912	-463.4
CF53		917	0.864	1047.0
CF48		918	0.864	1489.0
CF44	B-01-C44-P&S	919	0.864	1661.0
CF39		920	0.864	1426.0
CF35	B-01-C35-P&S	921	0.864	986.0
CF27	B-01-C27-P&S	922	0.864	672.5
CF25		923	0.864	504.0
CF17	B-01-C17-P&S	924	0.864	344.5
CF16		925	0.864	181.4
CF14		926	0.880	65.5
CF 8		927	0.944	37.0

Table 3.9 Peak Stress (psi) on level-01 Deck for Load case 7
(Ram 39, Moving load)

Ship Fr. No.	Strain Gage Location	Element No.	Time Instant (sec)	Peak Stress (psi)
258		897	0.930	78.3
248		898	0.920	107.0
238		899	0.920	161.4
228		900	1.210	-109.6
217		901	0.940	-423.8
204		902	0.930	-608.9
192		903	0.920	66.7
150		904	0.900	-1721.0
132		905	0.900	-2800.0
128	B-01-128-P&S	906	0.900	-5500.0
106		907	0.900	-5820.0
96		908	0.890	-6437.0
86	B-01- 86-P&S	909	0.890	-6617.0
82		910	0.890	-6365.0
74		911	0.880	-5452.0
63		912	0.870	-5440.0
55	B-01- 55-P&S	913	0.860	-5993.0
39	B-01- 39-P&S	914	0.850	-5577.0
CF67		915	0.850	-4592.0
CF60		916	0.840	-3757.0
CF53		917	0.840	-2441.0
CF48		918	0.840	-1140.0
CF44	B-01-C44-P&S	919	0.870	1082.0
CF39		920	0.870	1166.0
CF35	B-01-C35-P&S	921	0.870	752.8
CF27	B-01-c27-P&S	922	0.870	1442.0
CF25		923	0.870	1354.0
CF17	B-01-C17-P&S	924	0.830	1091.0
CF16		925	0.830	652.1
CF14		926	0.830	257.5
CF 8		927	0.840	137.5

Table 3.10 Peak Stress (psi) on level-01 Deck for Load case 8
(Ram 14, Load location D)

Ship Fr. No.	Strain Gage Location	Element No.	Time Instant (sec)	Peak Stress (psi)
258		897	0.672	47.5
248		898	0.656	65.4
238		899	0.656	99.1
228		900	0.672	-67.8
217		901	0.672	-262.6
204		902	0.656	-378.3
192		903	0.656	41.8
150		904	0.640	-1066.0
132		905	0.640	-1696.0
128	B-01-128-P&S	906	0.640	-3451.0
106		907	0.640	-3752.0
96		908	0.640	-4232.0
86	B-01- 86-P&S	909	0.640	-4422.0
82		910	0.640	-4332.0
74		911	0.640	-3791.0
63		912	0.640	-3882.0
55	B-01- 55-P&S	913	0.624	-4420.0
39	B-01- 39-P&S	914	0.624	-4306.0
CF67		915	0.624	-3657.0
CF60		916	0.624	-3238.0
CF53		917	0.624	-2477.0
CF48		918	0.624	-1582.0
CF44	B-01-C44-P&S	919	0.704	-307.1
CF39		920	0.704	-389.0
CF35	B-01-C35-P&S	921	0.704	-401.0
CF27	B-01-C27-P&S	922	0.608	826.1
CF25		923	0.608	839.6
CF17	B-01-C17-P&S	924	0.608	941.1
CF16		925	0.624	634.1
CF14		926	0.624	288.7
CF 8		927	0.624	169.4

Table 3.11 Peak Stress (psi) on level-01 Deck for Load case 9
          (Ram 14, Load location C)

Ship Fr. No.	Strain Gage Location	Element No.	Time Instant (sec)	Peak Stress (psi)
258		897	0.656	42.0
248		898	0.656	57.4
238		899	0.656	87.2
228		900	0.672	-61.6
217		901	0.656	-235.1
204		902	0.656	-338.1
192		903	0.656	37.2
150		904	0.640	-944.8
132		905	0.640	-1534.0
128	B-01-128-P&S	906	0.640	-3022.0
106		907	0.640	-3238.0
96		908	0.640	-3615.0
86	B-01- 86-P&S	909	0.640	-3746.0
82		910	0.640	-3615.0
74		911	0.640	-3102.0
63		912	0.640	-3085.0
55	B-01- 55-P&S	913	0.640	-3329.0
39	B-01- 39-P&S	914	0.624	-2926.0
CF67		915	0.624	-2282.0
CF60		916	0.640	-1600.0
CF53	B-01-C44-P&S	917	0.640	-608.7
CF48		918	1.152	-177.5
CF44	B-01-C35-P&S	919	0.608	1062.0
CF39		920	0.608	1091.0
CF35	B-01-C27-P&S	921	0.608	754.3
CF27		922	0.608	795.2
CF25		923	0.608	695.7
CF17	B-01-C17-P&S	924	0.624	497.5
CF16		925	0.624	268.3
CF14		926	0.624	94.7
CF 8		927	0.640	44.0

Table 3.12   Summary of Results for Load Cases

	LC 1	LC 2	LC 3	LC 4	LC 5	LC 6	LC 7	LC 8	LC 9
Shape of Ice Load	Triangular	Concave curve	Convex curve	ABS	Ram 39	Ram 39	Ram 39	Ram 14	Ram 14
Peak Bow Force (MN)	2.0	2.0	2.0	2.0	25.	25.	25.	16.	16.
Duration T (sec)	1.0	1.0	1.0	1.0	1.1	1.1	1.1	0.85	0.85
Time to reach Peak force (sec)	0.667	0.667	0.667	0.728	0.65	0.65	0.65	0.50	0.50
Bow Force Location (Frame No.)	A CF21-25	A CF21-25	A CF21-25	A CF21-25	A CF21-25	B CF41-45	A TO C CF21-25 TO CF33-37	D CF25-29	C CF33-37
Calculated Peak Stress (psi)	610.2	610.9	610.0	610.5	7846.	4936.	6617.	4422.	3746.
Location of Peak Stress	B-01-39 -P&S	B-01-39 -P&S	B-01-39 -P&S	B-01-39 -P&S	B-01-39 -P&S	B-01-86 -P&S	B-01-86 -P&S	B-01-86 -P&S	B-01-86 -P&S
Time Instant of Peak Stress (sec)	0.680	0.680	0.650	0.730	0.880	0.896	0.890	0.640	0.640
Measured Peak Stress (psi)	-	-	-	-	6078.	6078.	6078.	2554.	2554.

the forward end of the ship. Typical stress time histories for element 914 from load cases 2 and 3 show that during the 1 second period of application of the impact loads, the response follows closely the shape of the forcing functions. After the initial 1 second, the vibration response damps out quite rapidly as the impact ends. The peak stress value for element 914 was found to be 611 psi at a time instant of 0.68 second in load case 2 and 610 psi at a time instant of 0.65 second in load case 3.

These results indicated that the peak stress values obtained for the three load cases were about the same in magnitude, although the time instant at which the peak stress occured did vary slightly.

In the present analysis, a fourth load case was carried out using ABS theoretical bow force time history curve (Figure 3.4). The stress response curves are presented in Figure 3.12. The response for strain gage B-01-128-P&S again shows two-node bending vibration after the impact load ends. For other locations between ship frame 128 and cant frame CF44, the response follows the pattern of the applied bow force time history and reaches the peak stress at about 0.73 second, which was the time to the peak of the bow force time history curve. It is noted that the response exhibits a sharp reversal of stresses immediately followed the 1 sec duration of the impact force. This pheonmenon is attributed to the unloading rate of the impact force. Referring to the ABS theoretical bow force curve, it is observed that the slope of the unloading branch is quite steep compared to the loading branch. The maximum peak stress obtained in this case is 610 psi at location B-01-39-P&S.

It is interested to note that the peak stresses obtained in load case 4 are about the same as those in load cases 1 to 3. In all four cases, the impact forces were applied at the same location A and the bow force histories had the same peak value of 2 MN and the same duration of 1 second. The difference between load case 4 and load cases 1 to 3 was that the time to peak force for load cases 1 to 3 was 0.667 second and for load case 4 was 0.728 second. The loading branches were about the same. In fact, it was noted that the loading branch for load case 4 fell between the loading branches of load cases 1 to 3, although load case 4 had a longer time to reach the peak force. In contrast, the unloading branch of load case 4 fell outside the bound of load case 3 and was much steeper. As a result, a sharp reversal of stresses occurred in load case 4. Based on the calculated results, it was found that the stress time histories obtained for these cases were quite similar following the pattern of the loading histories.

This initial phase of study shows that the dynamic response of the hull girder is predominantly corresponded to the two-node bending mode and the response followed closely to the shape of the forcing functions. This also served as a bench mark check in using the finite element model in the subsequent study.

The next three cases (load cases 5 to 7) utilized the actual bow force time history of Ram 39. Emphasis was given to the locations where the vertical bow forces were applied.

Figure 3.13 shows the stress time history results for load case 5 in which the bow force was applied to location A between cant frames 21 and 25. As ex-

pected from the initial study, the dominant vibration was found to be the two-node bending mode having a vibration frequency of about 3.1 Hz. The maximum peak stress value was determined to be 7846 psi occured at a time instant of 0.88 second. This was located at element 914 corresponding to ship frame 39.

Similarly, by examining the element stress time history for load case 6 in which the bow force was applied to location B between cant frames 41 and 45,the same phenomenon as in load case 5.was obtained. However, the location at which the maximum peak stress occured shifts towards the aft of the ship to element 909 (B-01-86-P&S) instead of 914 (B-01-39-P&S). The maximum peak stress was 4936 psi, as compared to 7846 psi in load case 5, and occured at a time instant of 0.896 second. For this case, the peak stress obtained for element 914 was 2513 psi at a time instant of 0.896 second. These results indicated that by changing the location of the applied bow forces from location A to location B, the maximum peak stresses dropped from 7846 psi to 4936 psi,occuring at different sections of the hull (see Tables 3.7 and 3.8).

For simplicity, the above two load cases assumed that the location of the bow forces was stationary during the entire duration of load application. To simulate more closely the case in reality, it became necessary to use moving loads with the actual measured time history of Ram 39. The impact velocity of 4.4 m/sec given in the ARCTEC report was assumed to be constant during the impact and the vessel moved with that velocity for a duration of 1.2 seconds. The data preparation for this case was much involved since the forcing function changed with time along the center line stem bar. In this particular case, the number of time functions had to be limited to 30 becasue of the limitation of SAP-V computer program. The results of this load case 7 are presented in Table 3.9 and in Figure 3.14. The maximum peak stress was found to be 6617 psi at a time instant of 0.89 second. This occurred at element 909 corresponding to strain gage location B-01-86-P&S.

By comparing the results of these seven load cases, it is noted that the variation of the peak stress values is not significant for different shapes of the forcing functions, if the loads are applied to the same location. The peak stress values obtained are about the same and the location at which the maximum peak stress occurred is also the same. For example, the maximum peak stresses found in load cases 1 to 3 were about 610 psi at location B-01-39-P&S for the applied vertical bow force of 2 MN. Because of the linear elastic analysis, this peak stress would be 7625 psi if the Ram 39 vertical force of 25 MN is applied to the same location A. In comparison, the maximum peak stress obtained in load case 5 when using Ram 39 bow force was 7846 psi, a ratio of 1.03. This variation could be attributed to the difference in shapes of the forcing functions.

Although the variation of peak stresses was insignificant when impacts were applied to the same location, it became considerably more significant when impacts were applied to different locations. For the two extreme locations, designated as location A and location B, for Ram 39 presented in load cases 5 and 6, the upper and lower bounds values of the peak stresses were obtained. For load case 7 where the Ram 39 loading was allowed to move at constant velocity between location A and B, the peak stresses were found to be within the two bounds. The maximum peak stress for load case 7 was located at B-01-86-P&S hav-

ing a value of 6617 psi at the time instant of 0.89 second. From the measured data of Ram 39, the maximum peak stress was found to be 6078 psi. In this case, the ratio of the maximum peak stress between the finite element analysis to the measured data is 1.09.

The next two load cases use Ram 14 bow force history applied to locations D and C, respectively. Based on the measured data of Ram 14, the load location for the measured time of 13.0 and 14.0 seconds was nearly stationary in way of cant frame 27. This corresponded to load case 8 where the load was applied to location D. The calculated maximum peak stresses were found to be 4422 psi and 3746 psi, respectively, for load cases 8 and 9, both occuring at the same strain gage location of B-01-86-P&S and at the same time instant of 0.64 second. Again, this analysis indicated that load case 8 showed higher peak stress than load case 9 in which the load location C was more towards the aft of the vessel. The measured maximum peak stress obtained from the Ram 14 was 2554 psi, which was lower than both load cases 8 and 9. The ratios of the maximum peak stress compared to load cases 8 and 9 were 1.73 and 1.47, respectively. Using Ram 14 loading, the comparision was not as good as that using Ram 39 loading. This study showed that in addition to the peak magnitude and time history of the impact load, the exact location at which impact takes place and the impact velocity are important in order to obtain a correct dynamic response.

4. CONCLUSIONS

1. The test data acquired during the POLAR SEA deployment in 1985 is a substantial contribution to the database available for developing a practical analytical model of ship/ice impact. The test data analysis shows that the analytical model used is capable to predict the impact loads due to ramming icebreaking. The model describes well the total force history and gives reasonable estimate of the force magnitudes. For more accurate force prediction the model should be further refined. However, two factors make it impossible to adjust the mathematical model using the presented test data.

    A. Insufficient Ice Data
        Since the impact load parameters (forces, pressure, time histories, etc.) depend on many variables (such as masses, shapes, velocities, etc.) it is essential to measure all of the variables or maintain the unmeasurable variables constant during the tests. It is very difficult, if not impossible, to fulfill this condition when ramming ice ridges. The presented data does not contain sufficient information on the variables related to ice, such as the shapes and masses of the ice ridges, its homogeneity, dynamic crushing strength of ice, etc. Since some of the ice parameters in equations (1)-(7) could vary randomly during the tests and their values and changes are unknown, one can hardly expect accurate results for each particular events, even if the equations are perfect. Therefore, the inaccuracy of the calculated ice forces, which takes place for some peak forces such as 3-(1), 3-(2), 17-(3), 25-(3), 26-(1) in Table 5, should rather be related to the insufficient ice data.

    B. Insufficient velocity data
        The velocity data contains only the horizontal velocity records which often are interrupted. A majority of the rams have resulted in successful breaking through the ridges. Many of the rams, consisted of consecutive impacts followed by beachings. In such conditions the horizontal velocity history, even if accurate, does not characterize the penetration (crushing) velocity history. The latter can be obtained if an additional velocity or acceleration component is measured, such as vertical velocity of the bow, or pitching accelerations or others.

2. The analytical model described in Section 2 can predict the loads due to ship/ice impacts, both in general, and specifically for ramming icebreaking. Even at its present form given by equations (3)-(7) it gives reasonable estimates of ramming forces. Further

developments of the model are desirable and feasible, both analytically and experimentally.

3. The analytical efforts should be concentrated on widening the model's applicability. Ice impacts against ship sides and appendages should be specified in detail for various shapes of ship structures and ice features. Post-impact beaching forces should also be included in the model.

4. The experimental studies, which can be most valuable for the analytical model and less expensive, may include:

> - Ramming tests on very thick level ice, either grounded or floating. If such a field is found, its mass, shape, strength and homogeneity can be specified accurately enough to assume it virtually constant during the trial. As a result, only several rams would give sufficient, reliable and interpretable information on ice loads both during the impact and beaching phases. Those tests can establish experimental dependence of the ramming loads on the ramming speed - which is the principal variable in any model.
>
> - Ramming tests at various size bergy-bits of glacial ice. The main variables in such tests can be the ice mass (and consequently the reduced ship/ice mass). Since ice properties of freely floating glacial ice can be assumed virtually constant, while ice shapes vary randomly, the number of rams should be sufficient for statistical confidence.
>
> - In-situ ball-dropping or pendulum tests. In these tests all variables can be accurately recorded and controlled. As a result, the tests can provide information on the effects of many variables, as well as the values of the dynamic crushing strength of ice.

5. Based on the dynamic analysis of the finite element model, the dominant vibration was the two-node bending mode of the hull girder, having a natural frequency of 3.1 Hz. The frequency agrees very well between the calculated and measured results.

6. The dynamic response showed that the shape of the stress time history curve followed closely to the shape of the applied bow force curve. In this study, the maximum peak stresses obtained in load cases 1 to 4 were about the same for the same peak value of the unit impact load and impact location, although the shape of the applied bow force was different. Therefore, the maximum peak stress value was not signficant to the shape of the bow force, This may be due to the fact that the resonance did not occur in this case.

7. It was found that the exact location at which the impact bow force occurred was an important factor in the peak stress values. The maximum peak stress obtained was higher when the bow force was applied more towards the forward end. It is noted that efforts are made towards the prediction of the magnitude and shape of the ice force both by analytical means and by measurements. It is equally important to include the effort in determining the exact location and disbribution of the ice force where the impact occurs in order to more accurately predict the structural response. The velocity of impact and the movement of the ice force along the center line keel also contributes to the acccurary in obtaining the dynamic response of the analytical model.

8. The maximum peak stresses obtained from the finite element analysis and the measured value did not agree quite well in the case when using Ram 14 loading, whereas in the case of Ram 39 moving load, the maximum peak stresses agree very closely. The difference in results attributed partly to the inaccuracy in defining the location of the ice ramming load and its movement in the measurements and partly to the inherent differences in the two methods in obtaining the stresses. In the finite element analysis, the response represents the coupled interaction of the entire hull structure of the three dimensional finite element model. On the other hand, the beam idealization of the hull girder used in the measurements is of two dimensional and the effect of shear deformation is neglected. In this regard, the assumption of beam behaviour in relating the measured stress to the bending moment may contribute to inaccuracy in obtaining the magnitude of bow force.

5. REFERENCES

1. Brown, T.G., Kocaman, A., Punj, V., Bercha, F.G. Iceberg-Structure Interaction Global and Local Loads. Proc. OMAE-86, April 1986, Tokio, Japan, Vol. 4, pp 374-378.

2. Glen, I.F., Comfort, G. Ice Impact Pressure and Load: Investigation by Laboratory Experiments and Ship Trials. Proc. POAC-83, Helsinki, Finland, April 1985, Vol. 1, pp 516-533.

3. Kheisin, D.E., Likhomanov, V.A., Kurdyumov, V.A. Determination of Specific Crushing Energy and Contact Pressures due to Solid/Ice Impact. Trans. Arctic & Antartica Research Institute, Leningrad, 1975, Vol. 326, pp 210-218, (in Russian). English draft translation by CRREL, TL539, 1976.

4. Kurdyumov, V.A., Kheism, D.E. A Hydrodynamic Model of Solid/Ice Impact. Applied Mechanics, Kiev, 1976, Vol. XII, #10, pp 103-109.

5. Kurdyumov, V.A., Kheisin, D.E. Determination of Ice Loads Acting upon Icebreaker Hull Due to an Impact. Trans. Lengingrad Shipbuilding Institute, issue 90, 1974, pp 95-100 (in Russian).

6. Nevel, D.E. Iceberg Impact Forces. Proc IAHR Ice Symposium-86, Iowa City, Iowa, August 1986, Vol. 3.

7. Tunik, A.L. Dynamic Ice Loads on a Ship. Proc IAHR Ice Symposium 1984, Hamburg, F.R. Germany, August 25-31, 1984, Vol. 3, pp 227-313.

8. Tunik, A.L. Hull Girder Bending Forces due to Ramming Icebreaking. Proc POAC-85, Narsarssuag, Greenland, September 1985, Vol. 2, pp 873-881.

9. Bathe, K.J. and Wilson, E.L. "Stability and Accuracy Analysis of Direct Integration Methods", International Journal of Earthquake Engineering and Structural Dynamics, Vol. 1, No. 2, 1973.

APPENDIX A

Finite Element Model
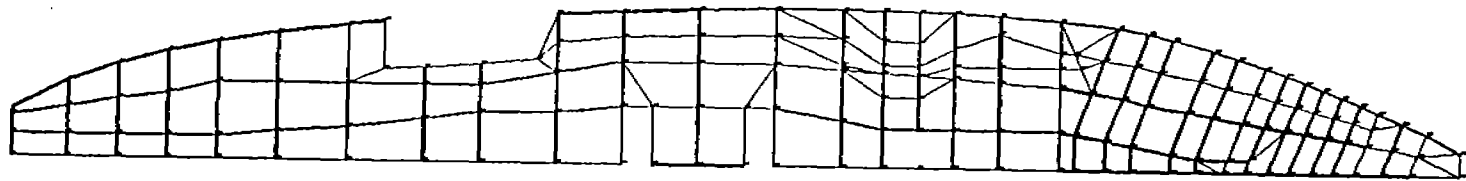
Figure A-1   01-Level Deck
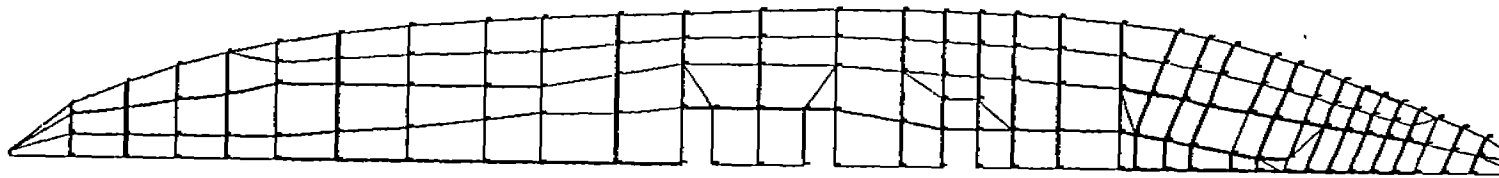
Figure A-2   Main Deck

Figure A-5   04-Level Deck

Figure A-3   02-Level Deck
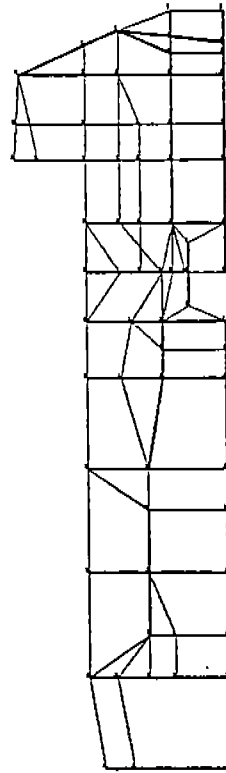
Figure A-4   03-Level Deck

A-2
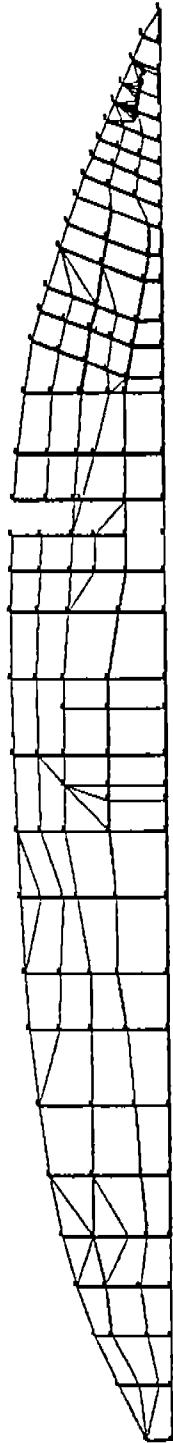
Figure A-6   Second Deck
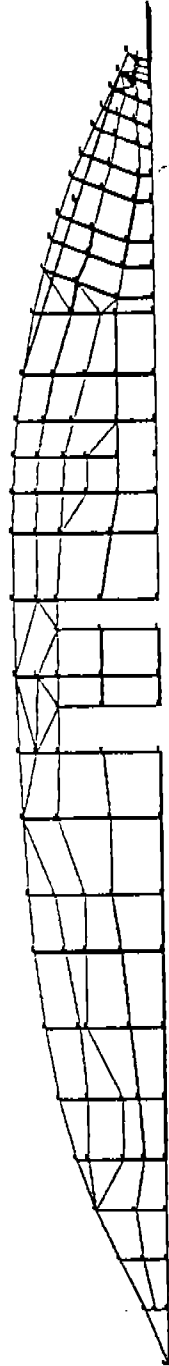
Figure A-7   Third Deck
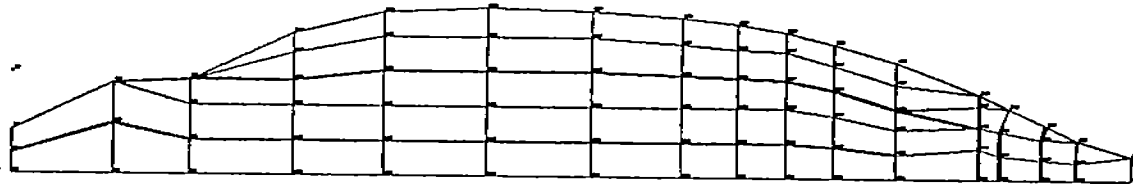
Figure A-8   Inner Bottom
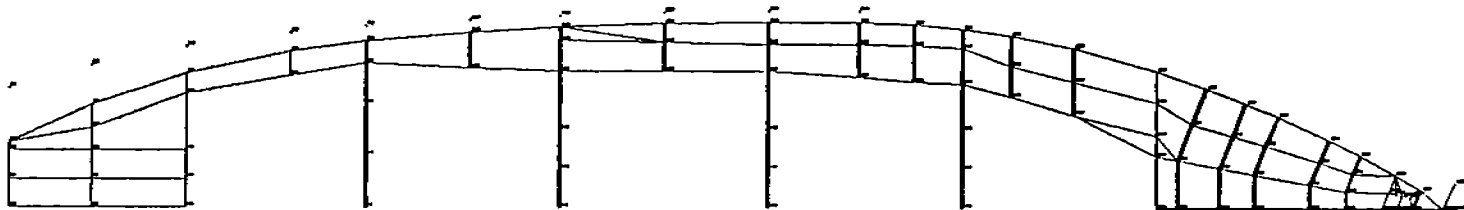
Figure A-9   1st Platform
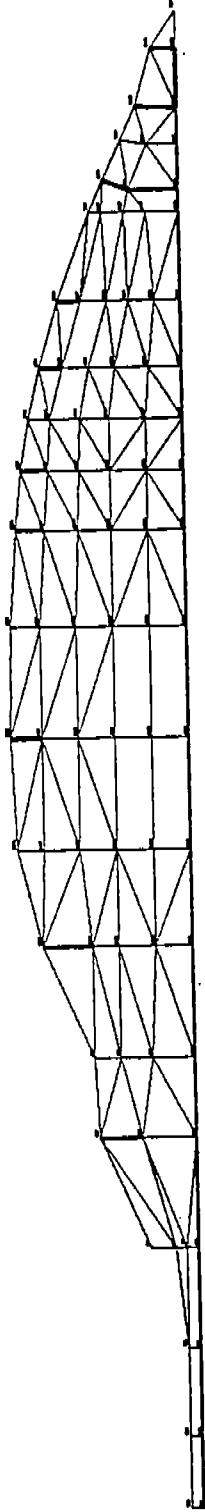
Figure A-10 Bottom
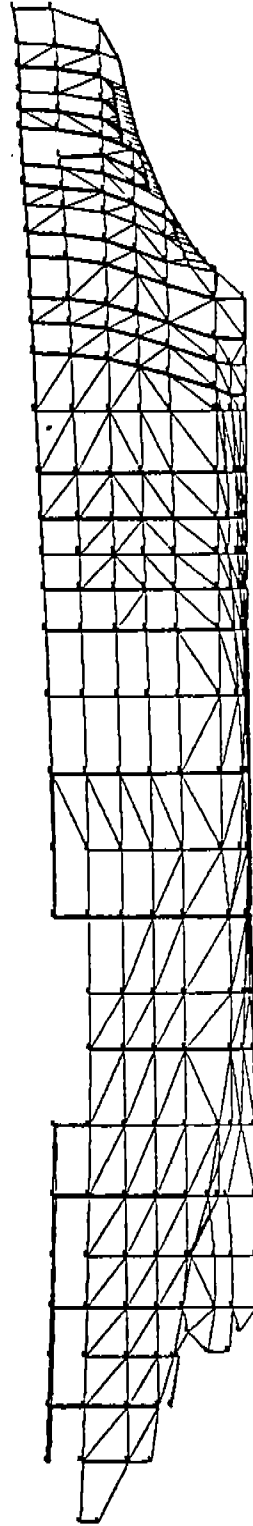
Figure A-11 Shell Plating
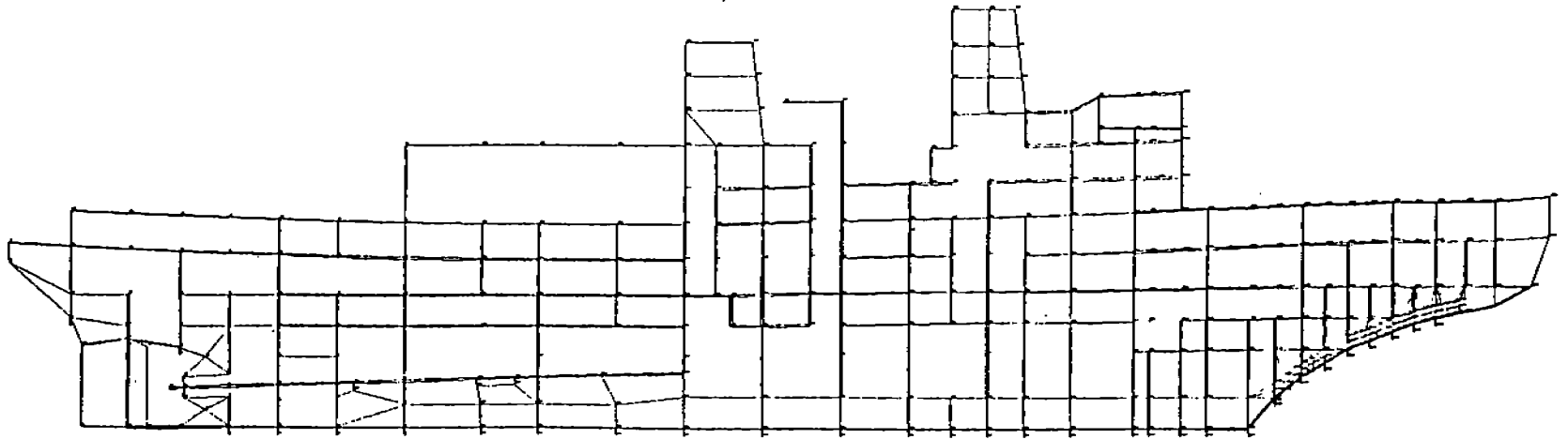
Figure A-12   Center line Vertical Keel
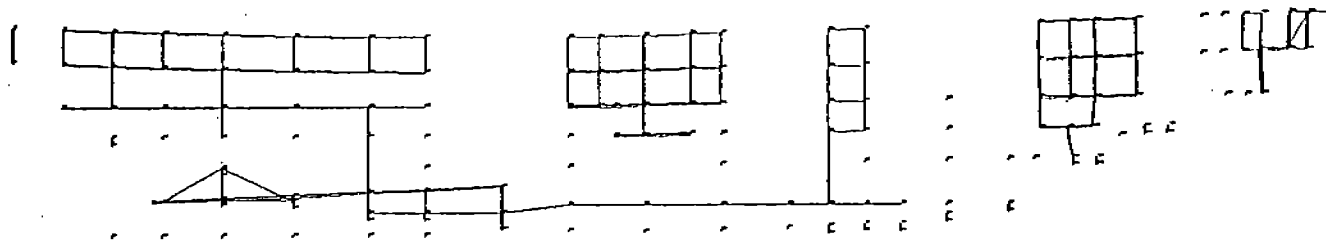
Figure A-13 Shafting, 15 ft.- 21 ft. off C.L.
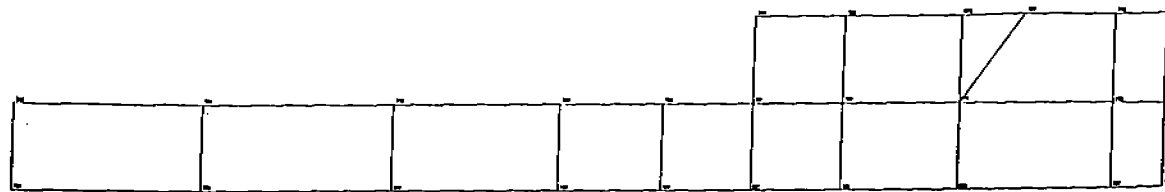
Figure A-14 Long. Bhd, 26 ft. 6 in. off C.L.
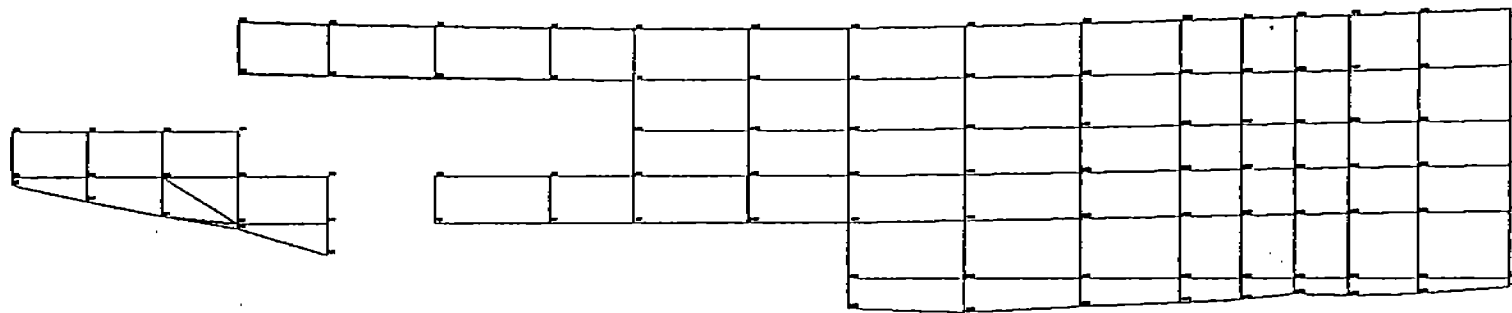
Figure A-15 Long. Bhd, 4 ft.- 14 ft. off C.L.
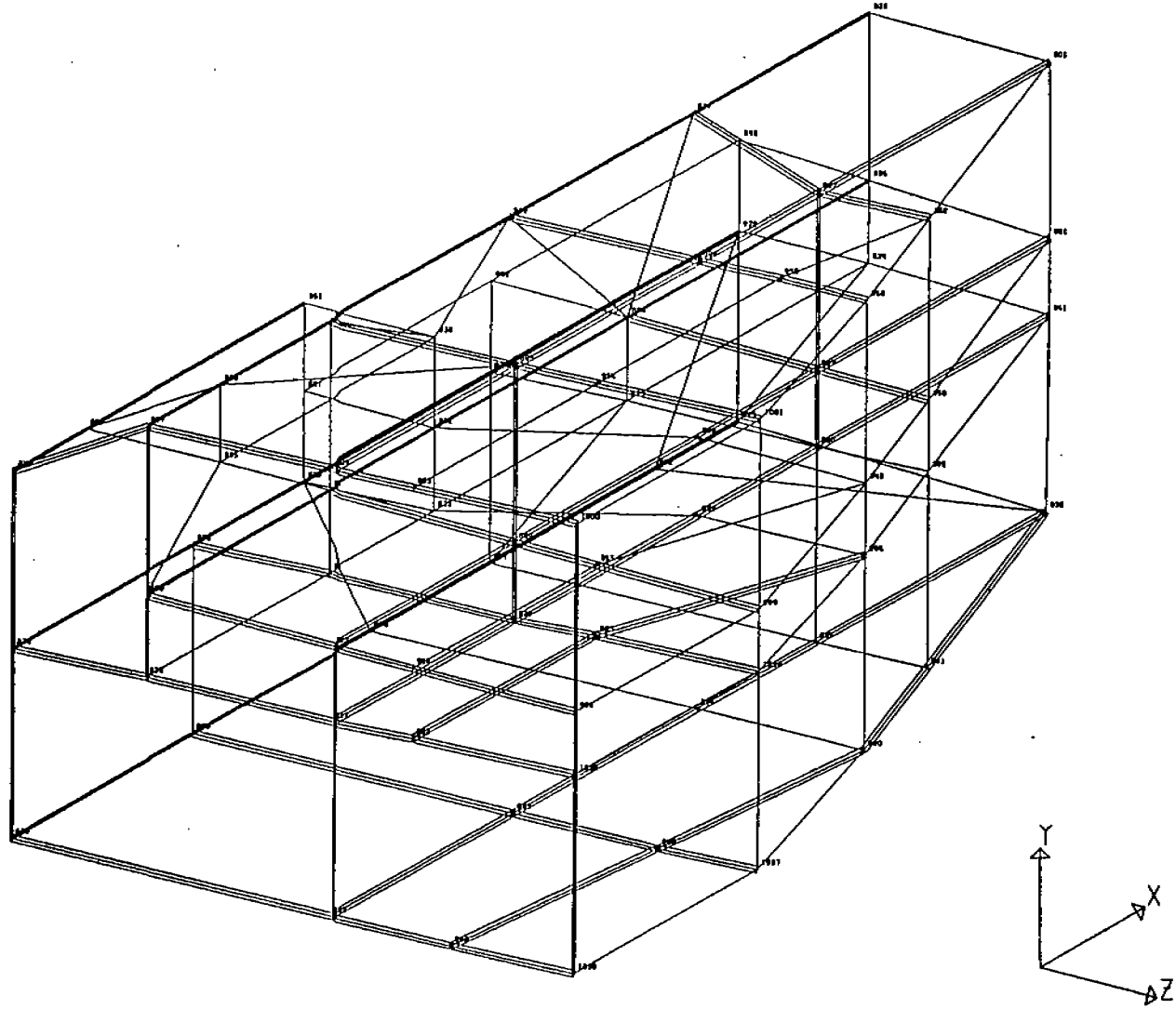
Figure A-16   Pilot House
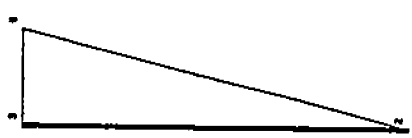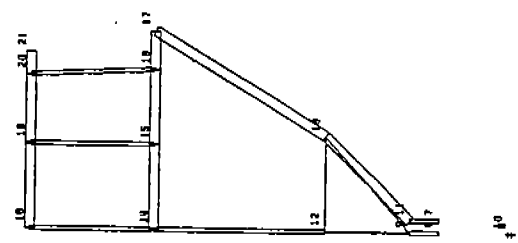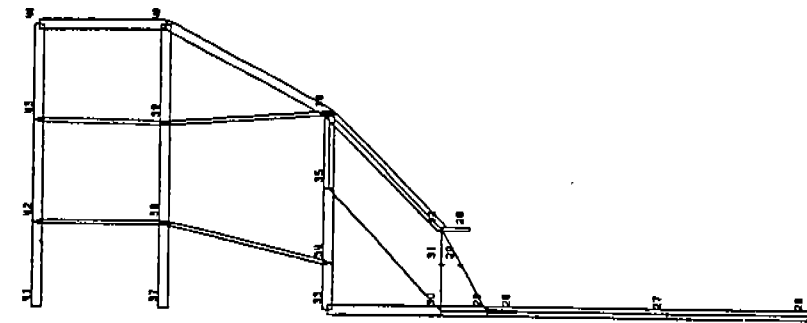
Model Fr. 1 (Ship Fr. 275)   Model Fr. 2 (Ship Fr. 263)   Model Fr. 3 (Ship Fr. 253)

Figure A-17   Transverse Sections
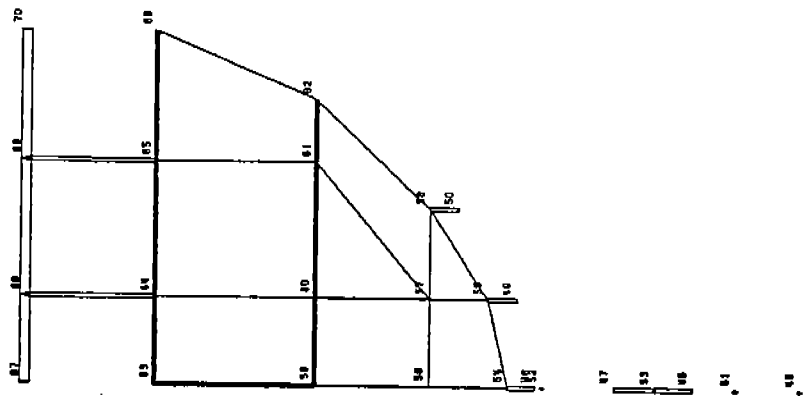
Model Fr. 4 (Ship Fr. 243)
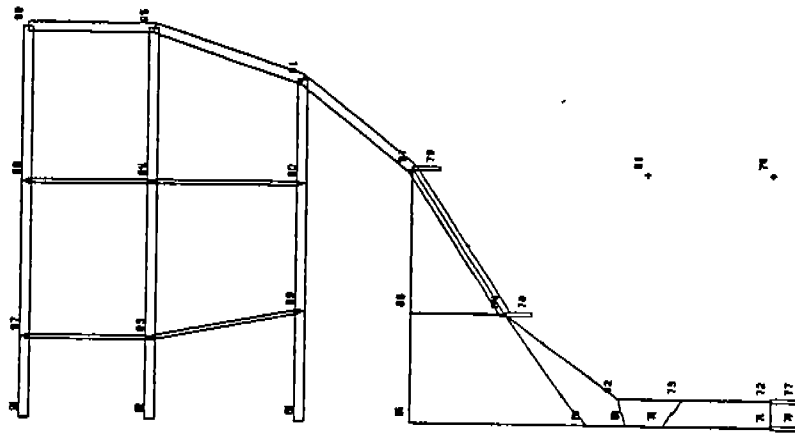
Model Fr. 5 (Ship Fr. 233)

Figure A-17 (Continued)

A-10

Model Fr. 7 (Ship Fr. 211)

Model Fr. 6 (Ship Fr. 223)

Figure A-17 (Continued)
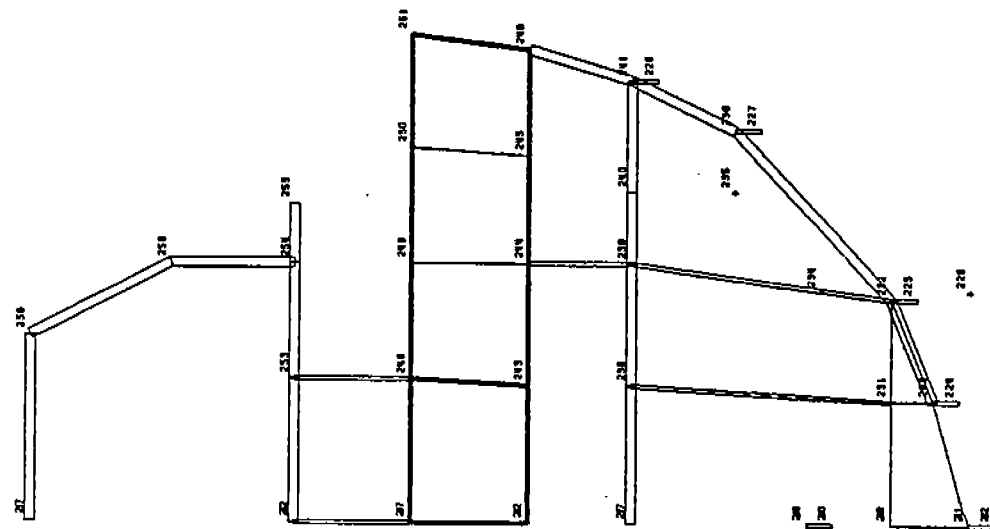
Model Fr. 9 (Ship Fr. 182)
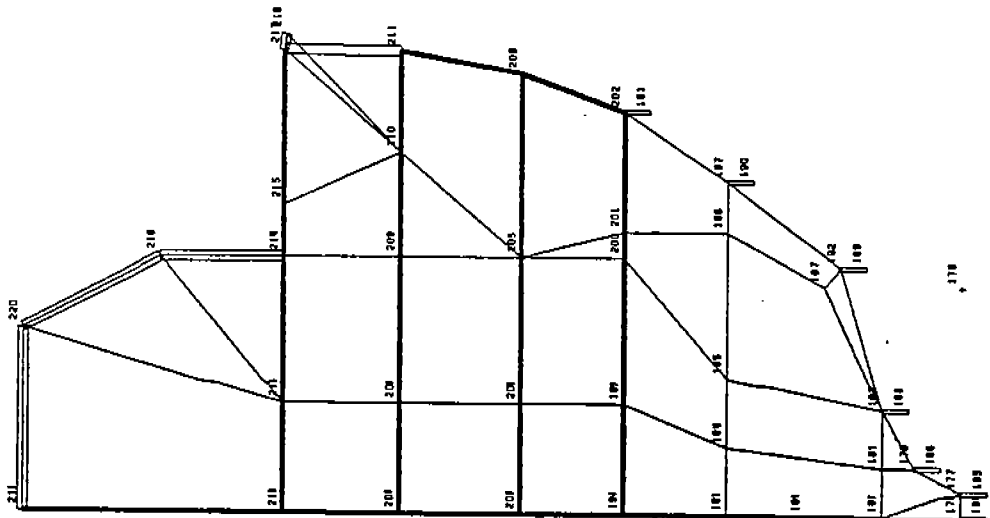
Model Fr. 8 (Ship Fr. 197)

Figure A-17 (Continude)

Model Fr. 11 (Ship Fr. 156)

Model Fr. 10 (Ship Fr. 171)

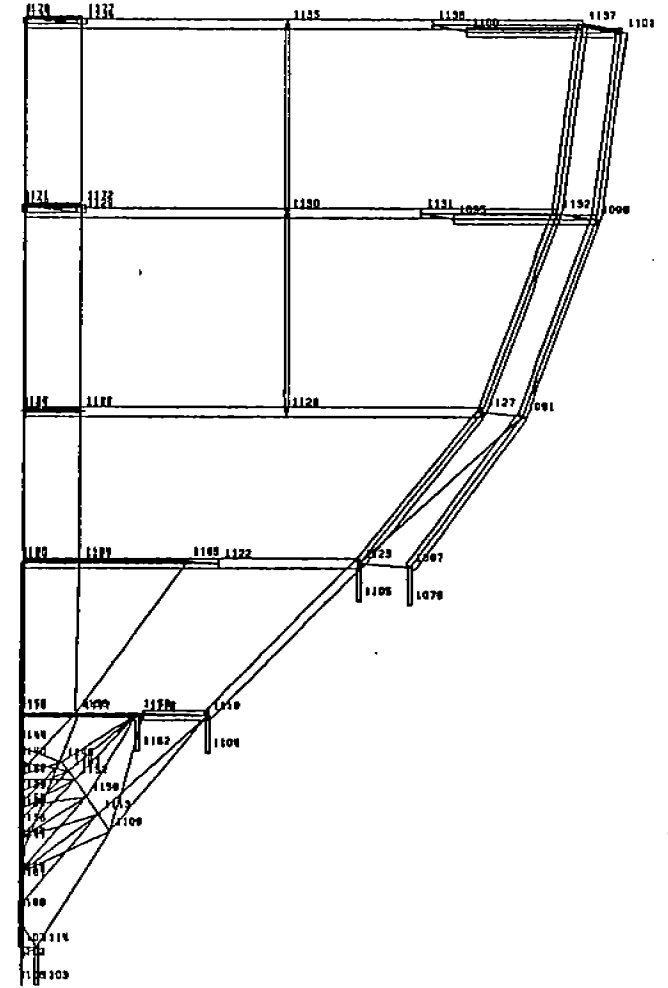Figure A-17 (Continued)

A-13
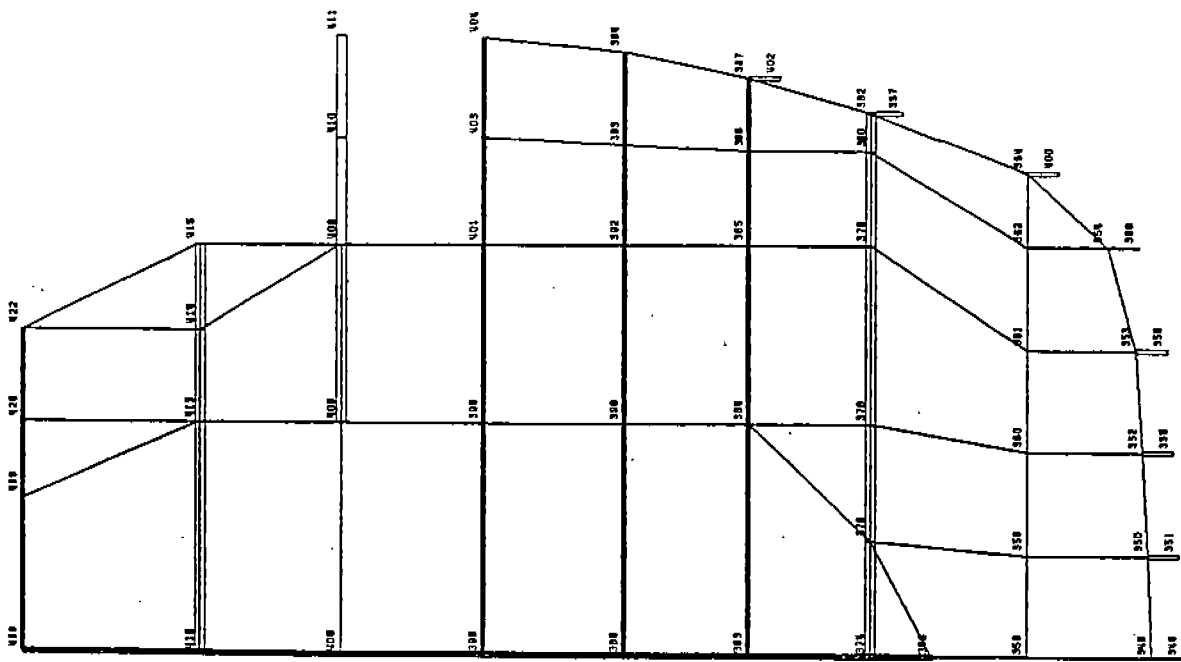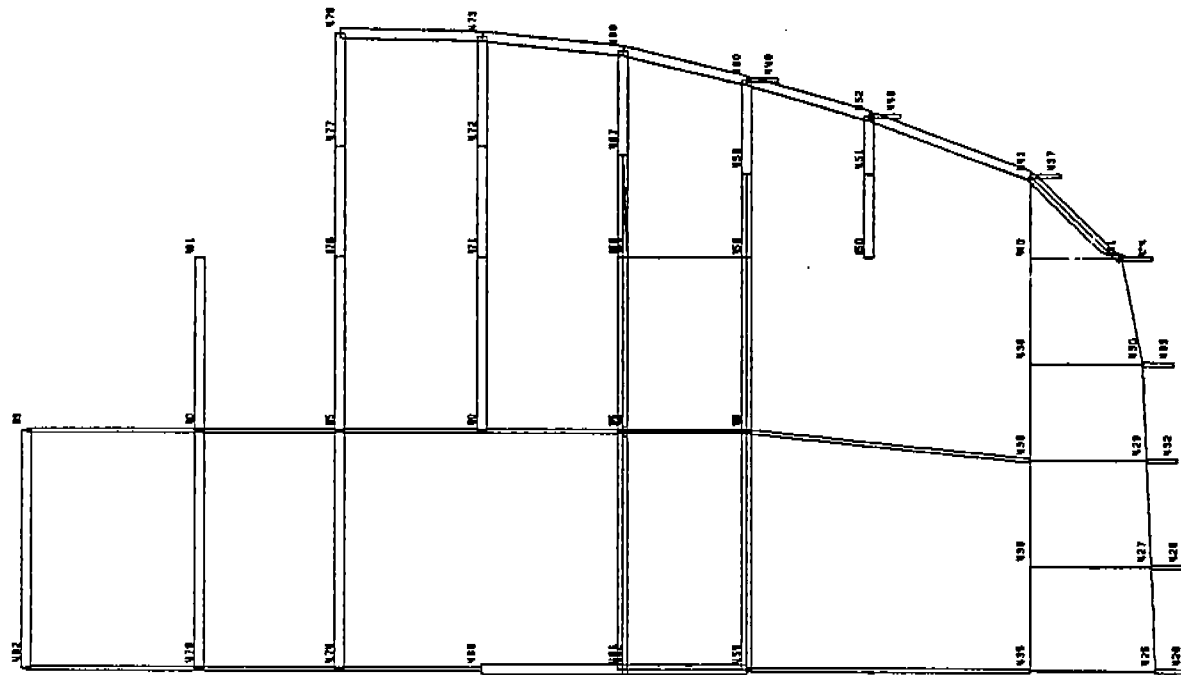
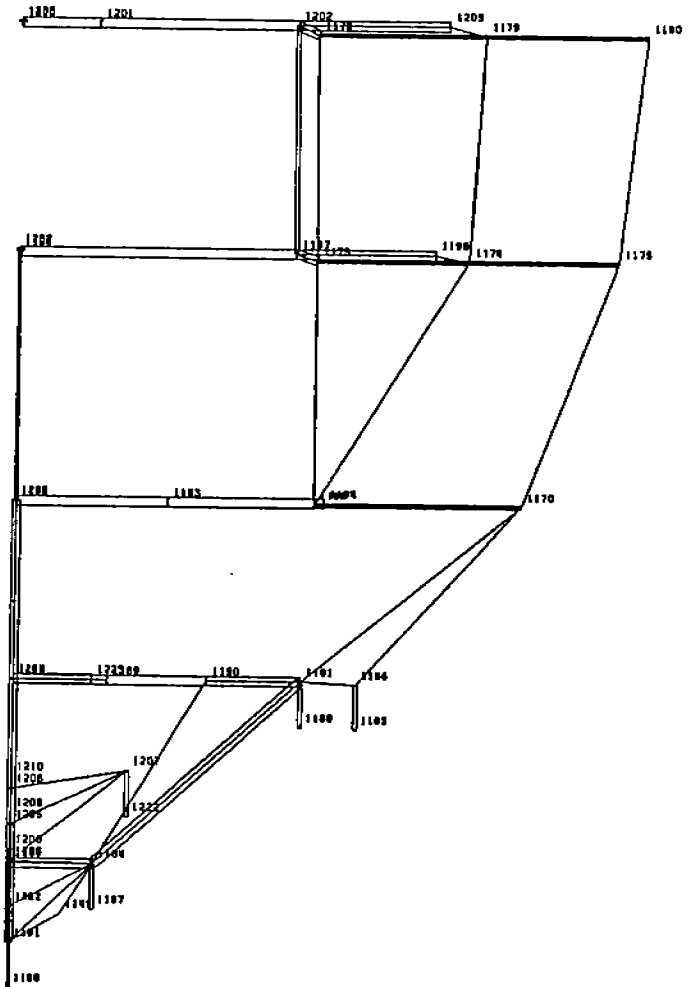Model Fr. 13 (Ship Fr. 128)

Model Fr. 12 (Ship Fr. 143)

Figure A-17 (Continued)

Model Fr. 15 (Ship Fr. 100)

Model Fr. 14 (Ship Fr. 113)

Figure A-17 (Continued)

A-15

Model Fr. 17 (Ship Fr. 85)
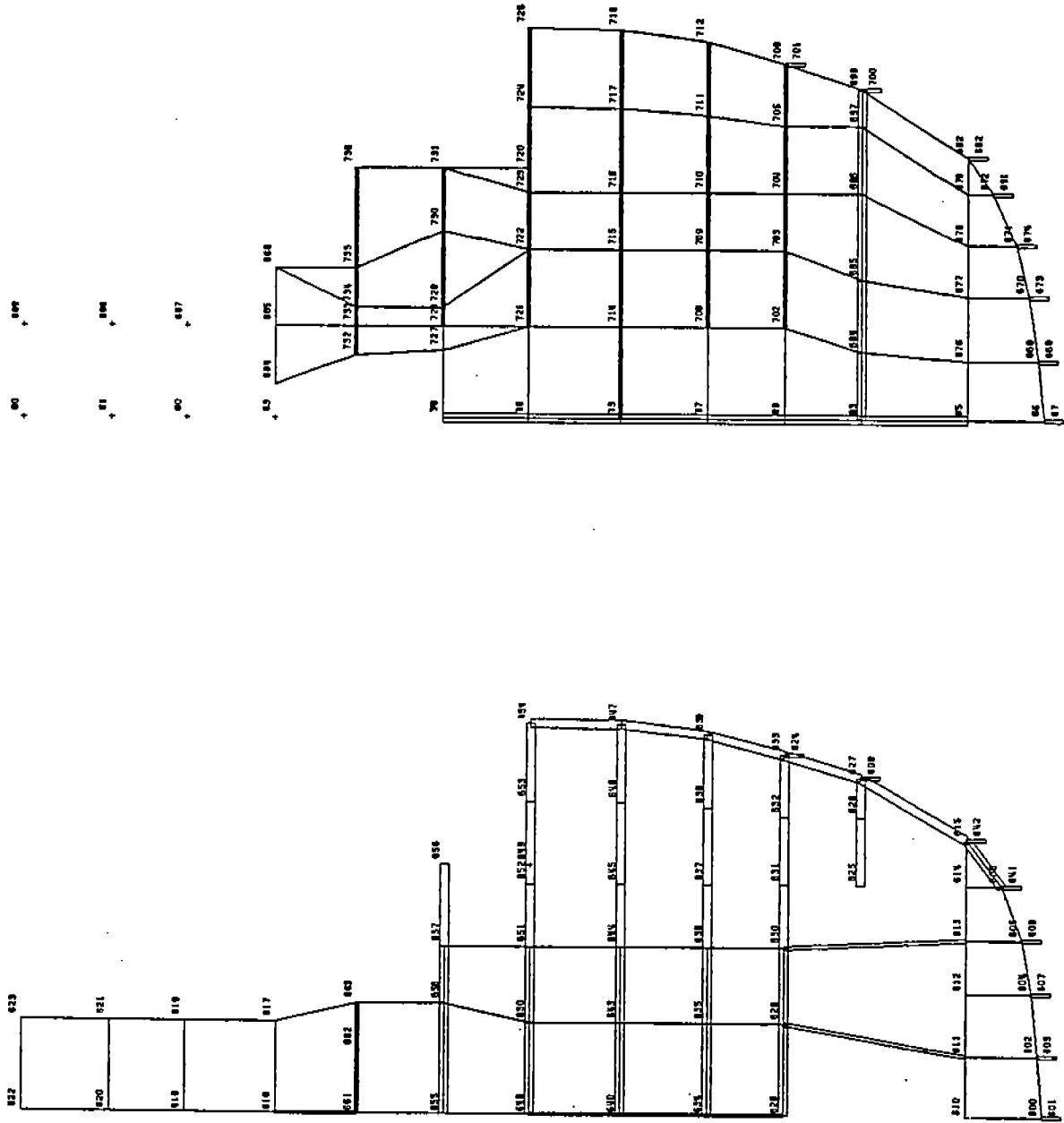
Model Fr. 16 (Ship Fr. 92)

Figure A-17 (Continued)
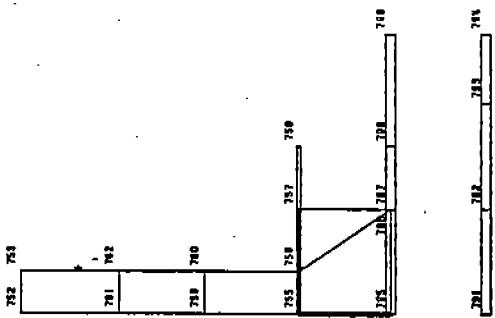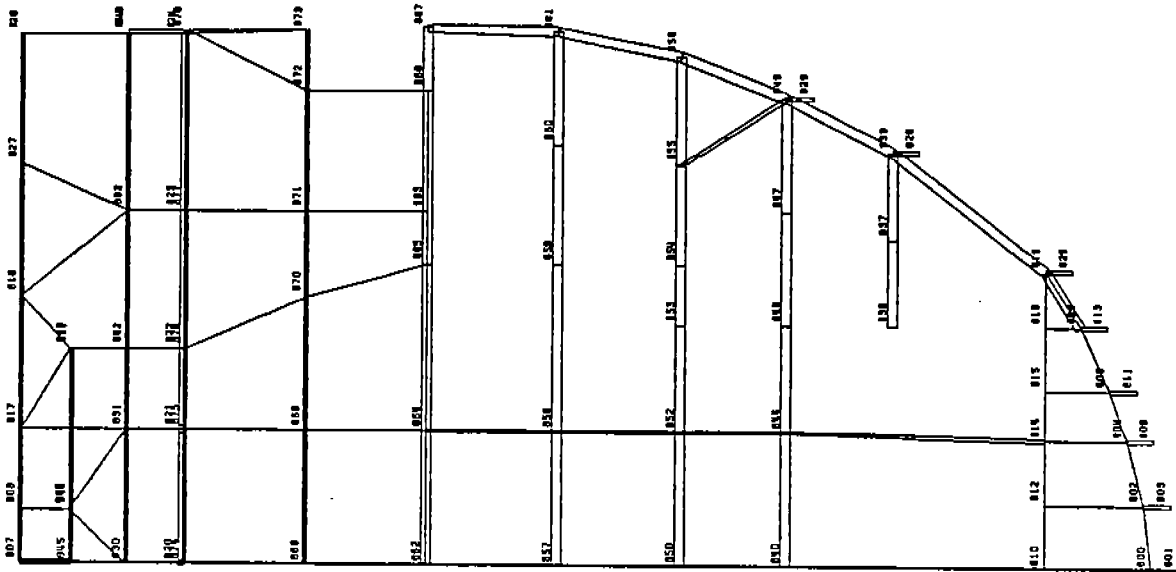
Model Fr. 19 (Ship Fr. 69)

Model Fr. 18 (Ship Fr. 78)

Figure A-17 (Continued)

A-17
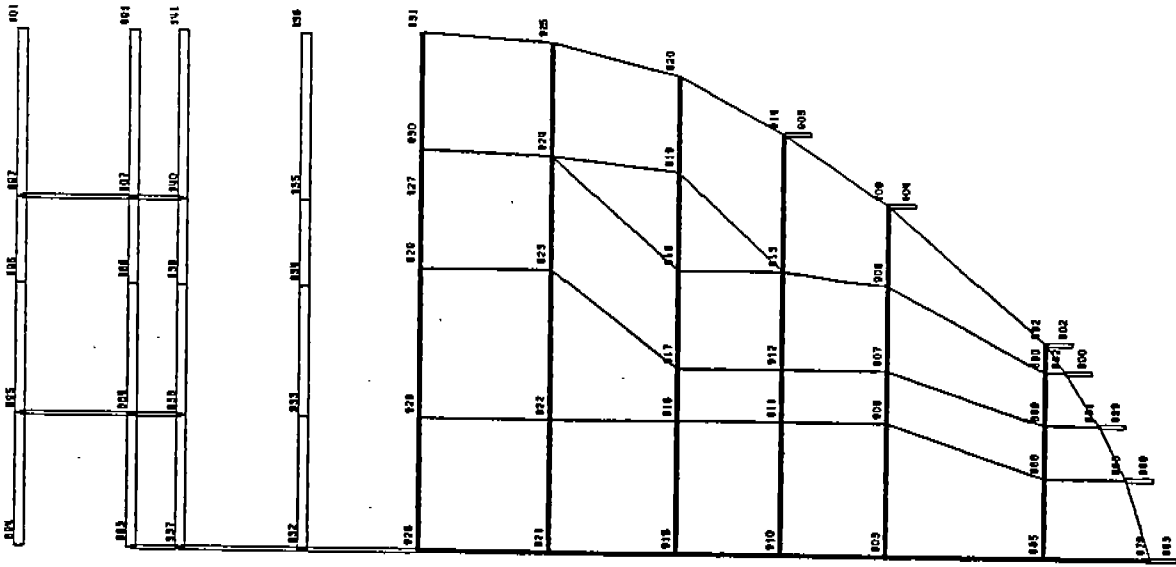
Model Fr. 20 (Ship Fr. 57)   Model Fr. 21 (Ship Fr. CF75)
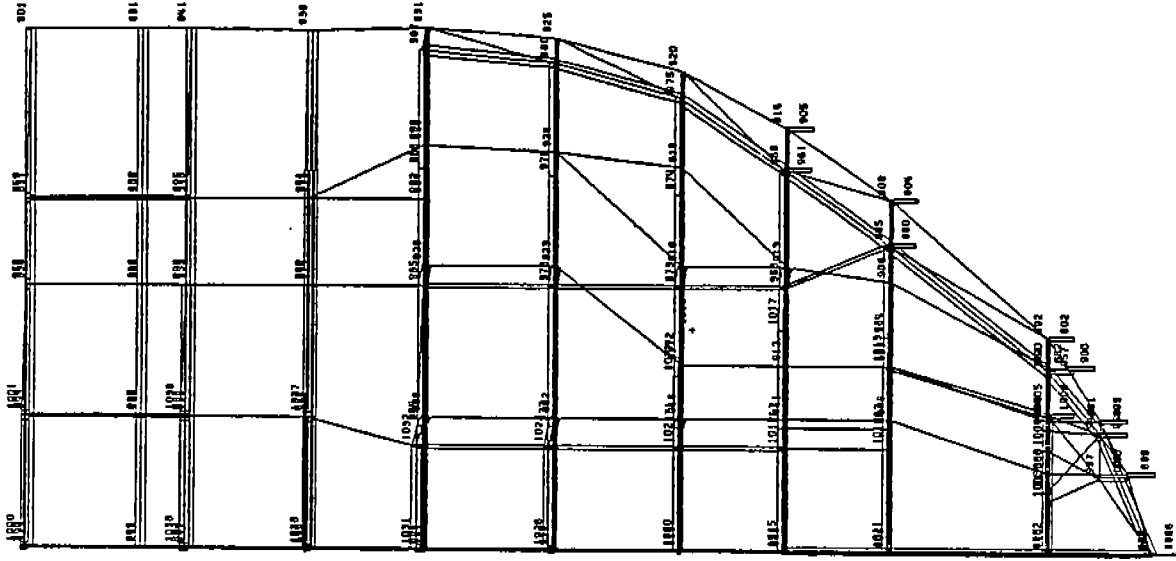
Figure A-17 (Continued)

A-18
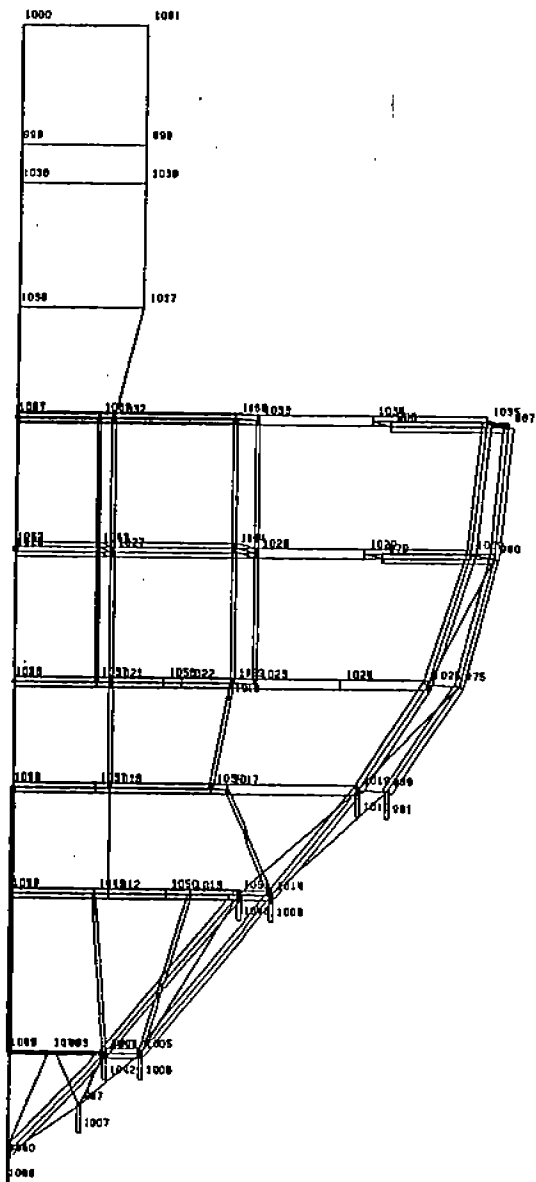
Model Fr. 22 (Ship Fr. CF69)   Model Fr. 23 (Ship Fr. CF64)
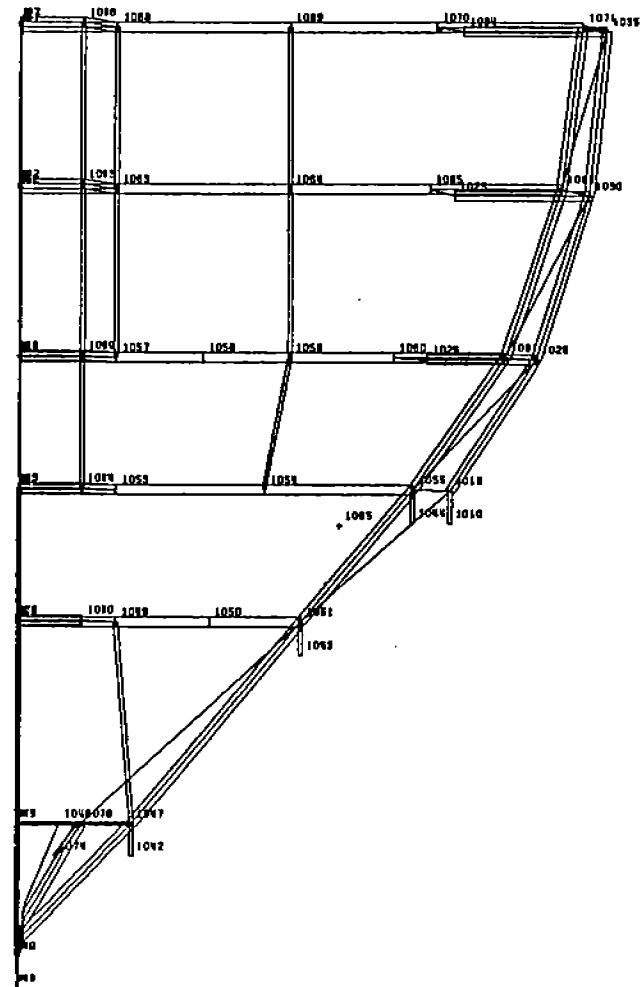
Figure A-17 (Continued)
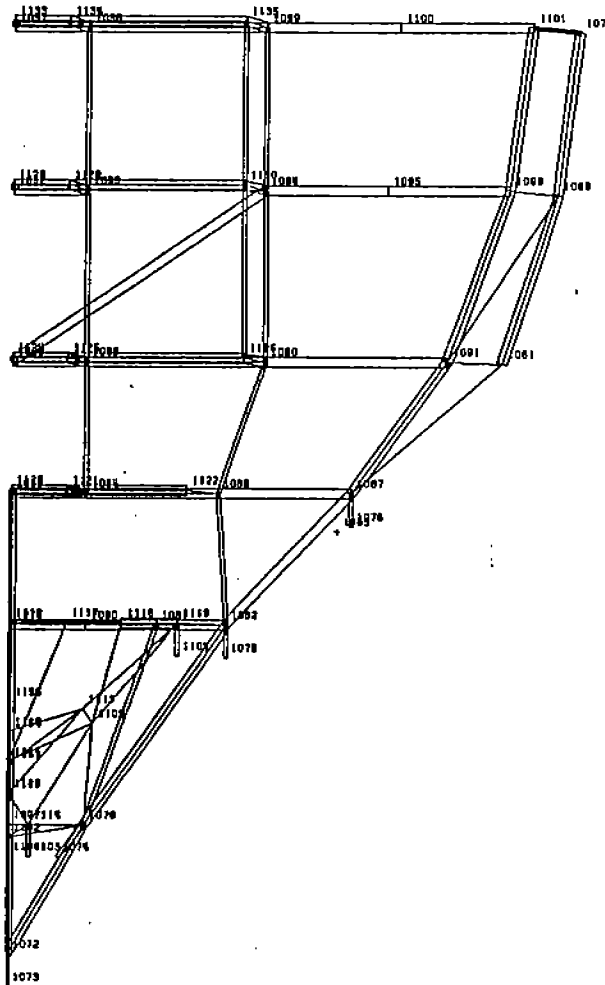
Model Fr. 24 (Ship Fr. CF56)   Model Fr. 25 (Ship Fr. CF51)
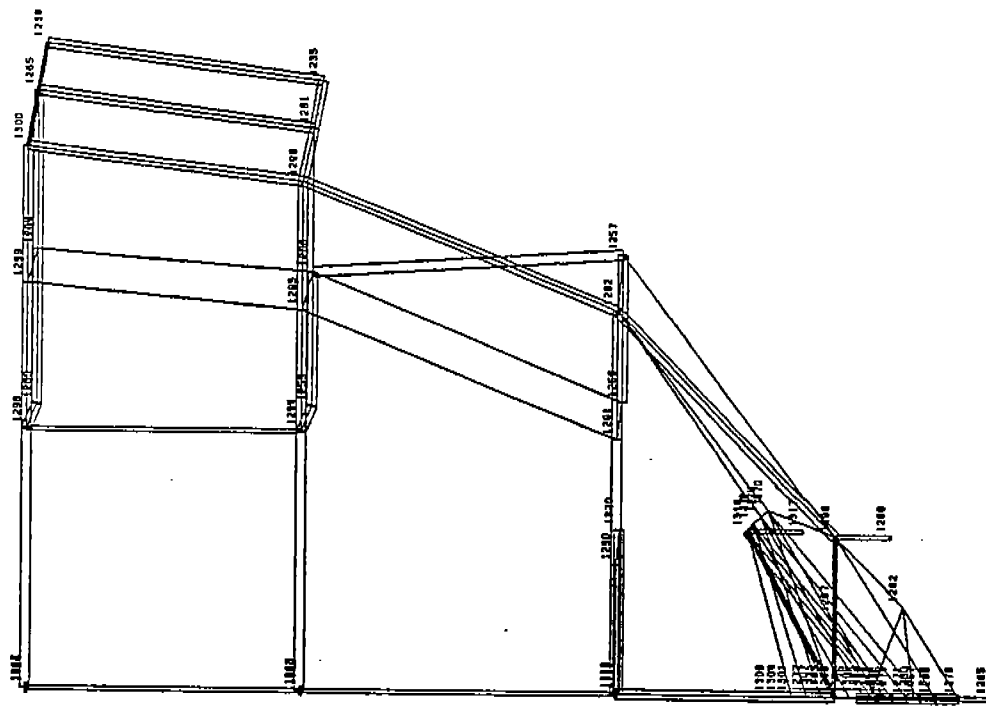
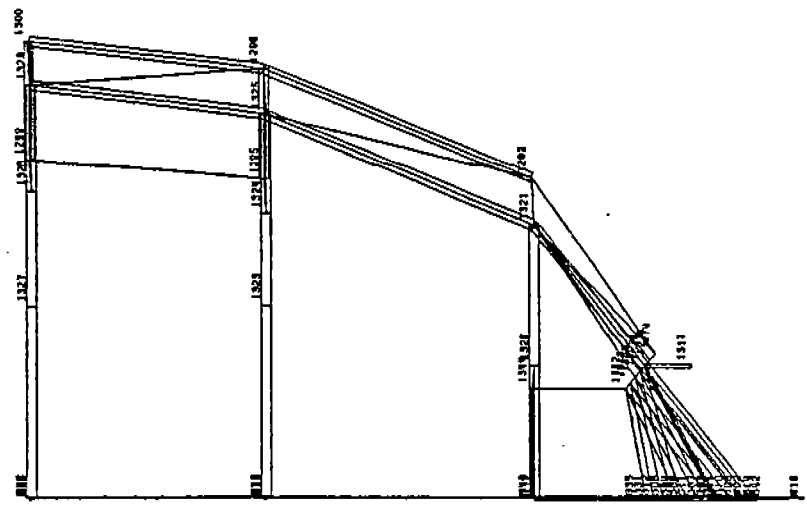Figure A-17 (Continued)
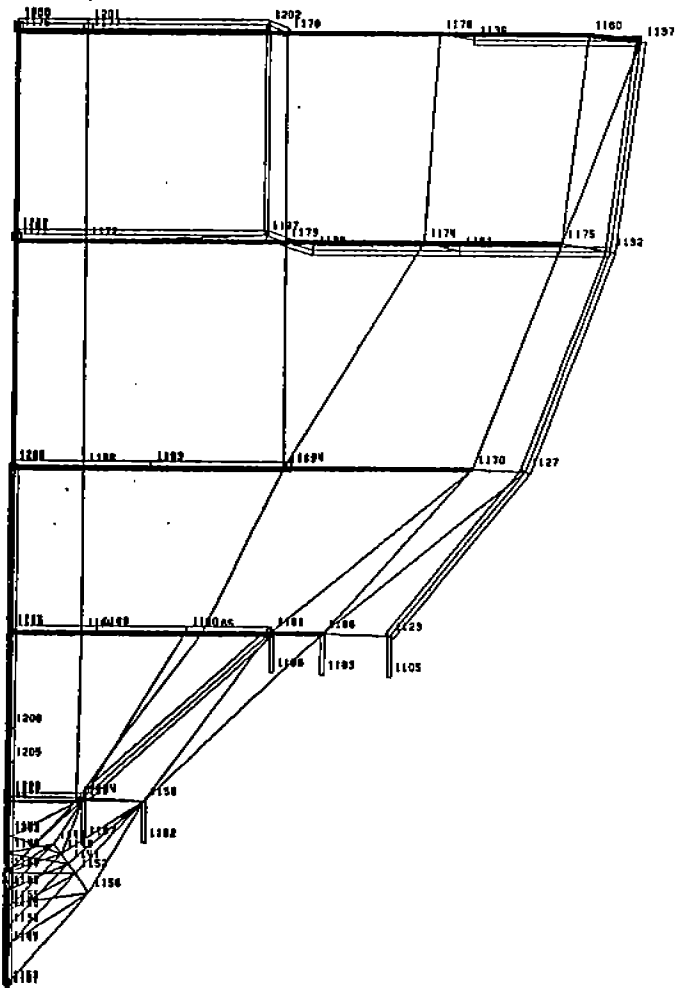
Model Fr. 26 (Ship Fr. CF45)   Model Fr. 27 (Ship Fr. CF41)

Figure A-17 (Continued)

Model Fr. 29 (Ship Fr. CF33)

Model Fr. 28 (Ship Fr. CF37)

Figure A-17 (Continued)

Model Fr. 31 (Ship Fr. CF25)

Model Fr. 30 (Ship Fr. CF29)
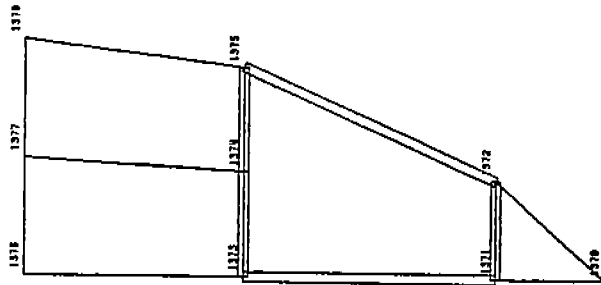
Figure A-17 (Continued)

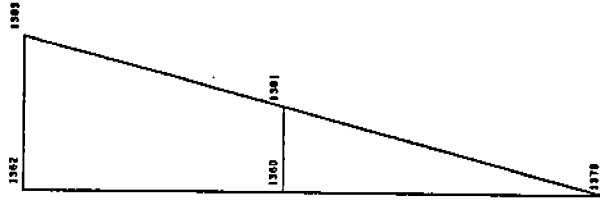Model Fr. 33 (Ship Fr. CF16)

Model Fr. 32 (Ship Fr. CF21)

Figure A-17 (Continued)

Model Fr. 34 (Ship Fr. CF11)   Model Fr. 35 (Ship Fr. CF6)

Figure A-17 (Continued)